NTNU
Norwegian University of
Science and Technology

Diesel Engine Response Improvements using Hybrid Turbocharging

Anders Gusevik Gravdal

Master of Science in Engineering and ICT
Submission date: June 2017
Supervisor: Eilif Pedersen, IMT

Norwegian University of Science and Technology
Department of Marine Technology

NTNU Trondheim
Norwegian University of Science and Technology
Department of Marine Technology

MASTER'S THESIS IN MARINE CYBERNETICS
SPRING 2017

ANDERS G GRAVDAL

Diesel Engine Response Improvements using Hybrid Turbocharging

Work Description: Turbochargers are commonly used with internal combustion engines due to improvements in power, efficiency and reduced emissions over naturally aspirated engines. These advantages allowed for the widespread adoption of turbo diesel engines for multiple purposes including marine propulsion. However, a turbocharged engine is limited by its ability to generate high boost pressure at low engine speeds, which in turn affects the transient response.

Several methods have been proposed and implemented to improve response of turbocharged engines. In several marine operations like anchor handling, crane operation and dynamic positioning an improved transient response could increase operational capability and safety.

In this thesis methods to improve the transient response will be explored, and the electrically assisted turbocharger will be modeled and simulated together with a full thermodynamic engine model. A design proposal for the system will also be made with the intent of installing the system in the engine lab at MTS in further work.

Scope of Work:

1. Review of necessary literature within the field of diesel engine modeling and simulation.
2. Build or adapt a dynamic process engine model.
3. Build an electrically assisted turbocharger model.
4. Show improved transient response in simulations.
5. Make a design proposal for implementing the system in the engine lab.

The report shall be written in English and edited as a research report including literature survey, description of mathematical models, description of algorithms, simulations results, discussion and a conclusion including a proposal for further work. The thesis should be submitted within June 11.

Eilif Pedersen, IMT
Main supervisor

Preface

This thesis is submitted to conclude a five-year master's programme in Engineering and ICT with a marine cybernetics specialization at the Norwegian University of Science and Technology. With a background in ICT and marine technology together with a fascination for engines, the topic of hybrid turbocharging presented itself as a golden opportunity to further explore this field of engineering.

The work presented was carried out from January to June of 2017 under the supervision of Associate Professor Eilif Pedersen.

The reader is assumed to have basic knowledge of engine modeling and simulation.

Acknowledgment

I would like to thank my supervisor, Eilif Pedersen, for his academic advice, during the work on this thesis. Not only did he provide valuable inputs but also showed a genuine interest in the topic which was inspiring and motivating.

Thanks also to Ingebrigt Valberg at SINTEF who was available for questions and showed interest in and provided answers to problems I presented to him. I would also like to thank Kevin Koosup Yum at SINTEF who took his time to help me with the engine model which he had worked on previously as part of his Master's thesis.

Finally, I am thankful for the support and encouragement received from friends and family.

Summary and Conclusions

Using a dynamic process diesel engine model, potential response improvements by use of an electrically assisted turbocharger were presented in simulations. The engine and motor model used to evaluate the concept were reviewed and explained in detail.

The engine model was validated against experimental data from a laboratory engine for various changes in speeds and loads. The model showed a response similar to the actual engine for transients at low engine speeds, and some discrepancies for transients at larger engine speeds.

A parametric study to determine response improvements from the electrically assisted motor showed that the time to reach 90 % of the step in engine speed from 1000-1400 rpm could be improved by 20-30 % with a maximum electrical motor assistance power from 3.5-8.8 kW. For a load increase step at a fixed engine speed of 1000 rpm response times were improved by 37-50 % with a maximum electrical motor assistance power in the range of 1.3-3.9kW

A design proposal consisting of a permanent magnet DC motor and control scheme to determine the onset and deactivation of assistance showed response improvements of 13 % in terms of time to reach 90 % of step in engine speed from 1000-1400 rpm.

Sammendrag

Ved hjelp av en dynamisk dieselmotormodell ble responsforbedring ved hjelp av en elektrisk assistert turbolader vist i simuleringer. Matematikken bak både dieselmotormodellen og den elektriske motormodellen ble gjennomgått.

Motormodellen ble validert mot eksperimentell data fra en faktisk motor på marinteknisk senter. Modellen og den faktiske motoren viste tilsvarende tidskonstanter for lave turtall, men større avvik for sprang i turtallet ved høyere motorturtall.

En parametrisk studie viste 20-30 % responsforbedring for en turtallsendring fra 1000 til 1400 omdreininger per minutt, ved hjelp av en elektrisk assistert turbolader. Turboladeren var assistert med en elektrisk motor med maksimal effekt på mellom 3.5-8.8 kW. Ved et konstant motorturtall på 1000 omdreininger per minutt og en påført lastendring ble responsen forbedret med 37-50 %, med en elektrisk assistert turbolader med en effekt på 1.3-1.9 kW.

En implementasjon av en elektrisk assistert turbolader bestående av en permanentmagnet likespenningsmotor, og en kontroll ordning som bestemte når motoren skulle assistere ble foreslått. Med denne implementasjonen ble tiden til å nå 90% av en turtallsendring fra 1000-1400 rpm redusert med 13 %.

Contents

Preface . . . i
Acknowledgment . . . iii
Summary and Conclusions . . . v
Sammendrag . . . vii

Nomenclature **xiii**

1 Introduction **1**
- 1.1 Background and Motivation . . . 1
- 1.2 Objectives . . . 2
- 1.3 Limitations . . . 3
- 1.4 Approach . . . 3
- 1.5 Structure of the Report . . . 3

2 Literature Review **5**
- 2.1 Engine Operating Conditions . . . 5
  - 2.1.1 Steady-state Conditions . . . 6
  - 2.1.2 Transient Events . . . 6
- 2.2 Benefits and Challenges of Engine Downsizing . . . 8
- 2.3 Forced Induction . . . 11
- 2.4 Turbocharging . . . 13
  - 2.4.1 Turbocharger Matching . . . 14
- 2.5 Engine Control . . . 22
- 2.6 Methods for Improving Transient Response . . . 25

2.6.1 Variable geometry turbines 26
2.6.2 Air injection systems 27
2.6.3 Combined Supercharging 28
2.6.4 Multiple Turbochargers 29
2.6.5 Hybrid Turbochargers 33
2.6.6 Comparison of systems 38

3 Hybrid Turbocharged Diesel Engine Model 39

3.1 Bond Graph as Modeling Framework 39
3.1.1 General Bond Graph Method 40
3.1.2 Pseudo Bond Graph Modified for Engine Process Modeling 41
3.2 Model Implementation 43
3.2.1 Cylinder 45
3.2.2 Intercooler 54
3.2.3 Turbocharger 54
3.2.4 Engine Controller 58
3.2.5 Electric motor model 60

4 Model Validation 63

4.1 Experimental Model Validation 63
4.1.1 Experimental setup 64
4.1.2 Analysis of Results 65

5 Simulation and Results 71

5.1 Selection of Simulation Cases 71
5.2 Parametric Study of Response Improvements 75
5.2.1 Performance Criteria 75
5.2.2 Motor Torque and Inertia 76
5.2.3 Ideal Motor 79
5.3 Design Proposal 86
5.3.1 DC Motors 87
5.3.2 Motor Implementation 91

6 Summary **99**

6.1 Summary and Conclusions 99

6.2 Discussion 101

6.3 Recommendations for Further Work 102

Bibliography **104**

A Appendix **108**

A.1 PID Control 108

A.2 Load acceptance test 109

Nomenclature

P	Pressure
T	Temperature
F	Fuel-air equivalence ratio / Force
V	Volume
$\dot{V}$	Rate of change of volume
E	Energy
$\dot{E}$	Energy flow
λ	Air-fuel equivalence ratio
ρ	Density
R	Gas constant / Radius
M	Molecular mass
S	Entropy / Stroke
U	Internal energy / Voltage
u	Specific internal energy
H	Enthalpy
h	Specific enthalpy

Q	Heating value
C_p	Heat capacity at constant pressure
C_v	Heat capacity at constant volume
γ	Ratio of specific heats
η	Efficiency
W	Work
$\dot{Q}$	Heat transfer rate
Tq	Torque
N	Rotational speed
ω	Rotational speed in radians per second
$\dot{m}$	Mass flow rate
Π	Pressure ratio
τ	Time constant / Delay
ϕ	Crank angle
i	Electrical current
EMF	Electromotive force
ψ	Flux linkage
L	Electrical inductance / Valve lift
A	Area
B	Bore
J	Mass moment of inertia

f_s	Stoichiometric fuel-air ratio
r	Electrical resistance
CI	Compression ignition
SI	Spark ignition
BMEP	Brake mean effective pressure
AFR	Air-fuel ratio
FAR	Fuel-air ratio
RPM	Revolutions per minute
(B)SFC	(Brake) specific fuel consumption
DC	Direct current
PMDC	Permanent magnet direct current
PMSM	Permanent magnet synchronous machine
IM	Induction machine
EATC	Electrically assisted turbocharger
EAC	Electrically assisted compressor
CHRA	Center housing and rotating assembly
NOx	Nitrogen oxide
ROHR	Rate of heat release
EGR	Exhaust gas recirculation
VGT	Variable geometry turbocharger

List of Figures

2.1 Steady-state torque profile for Scania DI09 072M 220kW 6
2.2 Torque development for speed and load increase transients 7
2.3 Comparison of torque development in a transient speed increase event and maximum steady-state torque 8
2.4 Brake specific fuel consumption for a baseline and downsized unit 9
2.5 Thermal efficiencies of various types of engines. Retrieved from Takaishi et al. [1] . 10
2.6 Comparison of maximum steady-state torque for baseline and downsized engines. Retrieved from Shahed and Bauer [2] 11
2.7 P-V diagram of ideal dual-combustion for a naturally aspirated and a supercharged engine 13
2.8 Schematic diagram of the turbocharger system with exhaust gas recirculation and charge air cooling 13
2.9 Diagram of turbocharger air path with corresponding subscripts 15
2.10 Compressor map for Scania DC1102 with indicated limits 17
2.11 Turbine maps 19
2.12 Turbine area and radius definition 20
2.13 Turbocharger matching procedure 22
2.14 Basic diesel engine control system 23
2.15 Controller output and fuel injection rate during a speed increase transient with active smoke limiter 25
2.16 Cause and effect diagram of a turbocharger with response improvements 26
2.17 0-60 mph response improvements by variable geometry turbine 27

2.18 Schematic diagram of an air injection system in conjunction with a turbocharger . 28
2.19 Schematic diagram of combined supercharging 29
2.20 Schematic diagram of a two-stage turbocharger configuration 31
2.21 Schematic diagram of a sequential turbocharger configuration 32
2.22 Comparison of torque development of a sequential turbocharged and conventional turbocharged engine 33
2.23 Schematic overview of the electrically assisted turbocharger configuration 34
2.24 Response improvements obtained by Millo et al. [3] with an electrically assisted turbocharger 35
2.25 Response improvements obtained by Katrašnik et al. [4] with an electrically assisted turbocharger 36
2.26 Schematic overview of the electrically driven compressor configuration 37
2.27 Response improvements obtained by use of an electrically assisted compressor . . 37

3.1 Causal stroke definition 40
3.2 Word bond graph for the engine model 44
3.3 Overview of cylinder model with sub-models 45
3.4 Pseudo bond graph of the engine cylinder 46
3.5 Stages of a typical CI engines combustion process as rate of released heat with respect to crank angle 48
3.6 Development of mass flow rate of fuel $\dot{m}_f$ during a speed increase transient 49
3.7 Effective area for intake and exhaust valve as a function of crank angle over one engine cycle 51
3.8 Bond graph implementation of the crank mechanism 52
3.9 Crank slider mechanism indicating the crank radius a and the connecting rod length l 53
3.10 Turbocharger model with sub-models 55
3.11 Block diagram representation of the engine control unit. 59
3.12 Permanent magnet DC-motor represented as an equivalent circuit and a bond graph 61
3.13 Series DC-motor represented as an equivalent circuit and a bond graph 62

3.14 Block diagram representation of the cascaded speed controller for the motors . . . 62

4.1 Engine speed, load, turbocharger speed, and manifold pressure for run 1 66
4.2 Engine speed, load, turbocharger speed, and manifold pressure for run 2 67
4.3 Engine speed, load, turbocharger speed, and manifold pressure for run 3 67
4.4 Effect of stricter smoke limiter on maximum steady-state torque, and operating conditions outside the scope of the model 69

5.1 Engine speed development for three different load acceptance tests 73
5.2 Engine variables for the 1000 and 2000 rpm load acceptance test 74
5.3 Load and speed increase transients selected for the parametric analysis 75
5.4 Definition of the performance index τ_{90} 76
5.5 Definition of the performance index τ_{rt} 76
5.6 Minimum motor torque required for the EATC to accelerate faster than a conventional TC as a function of motor inertia 77
5.7 Response time τ_{90} with varying turbocharger inertia 78
5.8 Engine speed, turbocharger speed and boost pressure responses for increasing turbocharger inertias 78
5.9 τ_{90} response times with ideal motor assistance for varying torques and durations . 80
5.10 Effects on engine variables with an ideal motor assistance of 0, 0.5, and 1Nm over 1.5 seconds 81
5.11 Operating points on compressor map plotted for three degrees of ideal motor assistance during a speed increase event 82
5.12 Comparison of turbocharger speed and power required for two ideal motors 83
5.13 Response time τ_{90} with increasing delays from start of transient to start of assistance 84
5.14 Response time τ_{rt} with ideal motor assistance for varying torques and durations . 85
5.15 Operating points on compressor map plotted for three degrees of ideal motor assistance during a load increase event 86
5.16 Torque speed curve of a PMDC motor, with suggested torque speed area and motor speed and torque development against time 88

5.17 Torque speed curve of a series DC motor, with suggested torque speed area and motor speed and torque development against time 89
5.18 PMDC and series DC motor acceleration from standstill to 30 000 rpm, and from 30 000 rpm to maximum speed 90
5.19 Possible configurations of the EATC 92
5.20 Pseudo code diagram for the EATC logic for the fixed rotor configuration 94
5.21 Pseudo code diagram for the EATC logic for the clutch configuration 95
5.22 Predefined clutch engagement profile 96
5.23 Engine variables for a speed increase event for the fixed rotor and clutch configurations 97
5.24 Engine variables for a speed increase event for the fixed rotor and clutch configurations without assistance 98

A.1 Block diagram of a PID controller in the loop. 108
A.2 Engine variables for the 1400 rpm load acceptance test 109

List of Tables

2.1 Comparison of methods to improve transient response 38

3.1 Basic bond graph elements 41
3.2 Thermodynamic properties and the semi-empirical relations with the efforts . . . 42
3.3 State variables for the modified pseudo bond graph 42
3.4 Constitutive laws for C- and R-fields 43
3.5 Friction coefficients for the clutch configuration 58

4.1 Model and laboratory engine specifications 64
4.2 Initial and final values of engine speed and loads for experimental validation of three transient runs 65
4.3 Steady-state differences of the simulation compared to experiment. 68

5.1 Load increase steps given in initial and final load in % of maximum load at given engine speed. 72
5.2 Motor parameters for the PMDC motor and the series DC motor 91
5.3 Moments of inertia used for the clutch and fixed rotor configurations 93
5.4 Response times for the proposed configurations for a 900-1400 rpm, 70-80 % load, speed increase transient 96
5.5 Response times for configuration 1 or 2 and configuration 3 for a 1300 - 1600 rpm speed increase transient without assistance 98

Chapter 1

Introduction

1.1 Background and Motivation

With increased fuel prices and increasingly stringent emission requirements, more efficient and environmentally friendly engines are demanded by the customers. A turbocharger increases the power potential per displacement of an internal combustion engine, allowing a smaller engine to replace a larger unit. This has shown to be an effective way of improving the engines efficiency and reduce emissions [5]. Typically the more downsized an engine is the more efficient it is. Since the diesel engine has several characteristics favoring high degrees of turbocharging over the gasoline engine, larger degrees of downsizing is achievable. As a result, turbocharged diesel engines are the primary choice for heavy-duty applications including vessels propulsion.

A central problem of turbocharged engines, especially heavily downsized units [2], is poor transient performance characterized by turbo-lag. While the engine itself may respond quickly to load and speed changes the delays associated with the inertias of turbocharger systems make the system as a whole respond accordingly.

In marine operations like anchor handling, crane operation and dynamic positioning where rapid speed and or load changes can occur, an improved transient response could increase the operational capability and safety. Furthermore, minimizing turbo-lag would mean that the engine would spend less time in unfavorable combustion conditions emission wise. Additionally by using less time to reach a more efficient operating condition, the fuel consumption could be reduced.

Further advances in electrical motor technologies has enabled the potential of hybrid turbocharging as a means to improve engine capabilities. By use of an external electric motor, the turbocharger can be accelerated up to speed faster than a conventional turbocharger. Although it is a relatively new concept, several studies have been performed over the past years. Most studies on the topic are simulation based on experimentally validated engine models. Among these, Millo et al. [3] investigated the use of an electric motor/generator connected to the turbocharger shaft of diesel engine. At high loads and speeds the hybrid turbocharger acted as a energy recovery system. The stored energy was then used by the motor to provide additional power to the turbocharger shaft under transients, increasing the engines capabilities. Another study was presented by Katrašnik et al. [4], which also showed improved transient capabilities by electrically assisting the turbocharger.

In this thesis the main focus is on the motoring mode of the hybrid turbocharger, i.e. supply the turbocharger shaft with additional power during transients to minimize turbo-lag, whereas the energy regeneration potential of the hybrid turbocharger is not considered. Although response improvements have been shown, the specific potential of implementing a hybrid turbocharger on an engine in the lab at the department of marine technology remains unknown.

1.2 Objectives

The main objective is to analyze response improvements in simulation by hybrid turbocharging a diesel engine. More specifically the objective can be split up into the following objectives: (1) assess how individual parameters of the hybrid turbocharger affect the transient response, (2) present a design proposal for how the system can be implemented in the lab in further work.

1.3 Limitations

There are several important limitations in the presented work: (1) tuning and validating the model in steady-state with the real engine was not done, (2) some discrepancies are seen between model and experimental values, and finally (3) the parameters used in the electric motors for the design proposal were freely specified.

From the limitations (1)-(3) the results obtained in this thesis will at best provide an initial estimate of the design parameters of the hybrid turbocharger for any implementation in the lab, while another design iteration would be needed for the specifics of the implementation. The general trends presented regarding response improvements, and suggestions for motor specifications given in the parametric analysis could still form a basis for further work.

1.4 Approach

In short the approach can be summarized by: (1) validate that the response times of the model and real engine are similar, (2) show response improvements by simulating the model together with the hybrid turbocharger, and determine how individual parameters related to the hybrid turbocharger affect response by means of a parametric analysis, (3) model and evaluate different types of implementations of the hybrid turbocharger.

1.5 Structure of the Report

The chapters in the remainder of this thesis is organized as follows:

Chapter 2 reviews literature relevant to the topic of hybrid turbocharging. The need for response improving systems are explained through the benefits and challenges of engine downsizing. The working principles behind the turbocharger is introduced together with how its dimensions and how the engine control system affects the transient performance. Finally, a review of what has been done to improve the response of turbocharged engines is presented.

Chapter 3 introduces the bond graph modeling framework and how it is used to model a hybrid turbocharged diesel engine. The mathematical engine model and its sub components are reviewed, together with the models used for the electrical motors.

In **Chapter 4**, the transient behavior of the model is compared to experimental data.

Chapter 5 present simulated response improvements by electrically assisting the turbocharger. Suggestions for specifications of the assistance motor is given together with a design proposal for implementing the system in the lab.

Chapter 6 finalizes the thesis with conclusions and discussions of the results together with recommendations for further work.

Chapter 2

Literature Review

This chapter attempts to summarize literature relevant to the topic of hybrid turbocharging. First, steady-state and transient operating conditions are introduced. Next, the need for hybrid turbocharging, or other response improving systems, is explained in light of benefits and challenges of engine down-sizing. The chapter continues with an explanation of the working principles of forced induction systems, with particular attention to the turbocharger and how the matching of a turbocharger is performed and its effect on engine response. Next, a brief introduction on the workings of the turbo diesel engine control system is given and how it affects the engine response before finally an overview of what has been done to improve response is given.

2.1 Engine Operating Conditions

Marine engines experience a wide range of engine conditions and load characteristics depending on the type of operation it is involved in. Cargo ships and other long-voyage freighters will typically maintain a constant speed and operate mostly in steady-state conditions, hence the transient performance of these operations are of little importance. On the other hand, vessels operating in anchor handling, crane operations or DP will experience frequent load and speed changes making the transient performance of engines in these operations increasingly important with respect to capability and safety.

2.1.1 Steady-state Conditions

A steady-state operating condition can be defined as an engine running at constant speed and load over a sufficient amount of time, to allow even the slowest dynamics of engine states, like temperature, to settle. Steady-state validation and testing can be done over the whole engine operating area in a systematic manner by iterating through range of values for each input parameter, load and engine speed, with respect to the other. A plot of maximum steady-state load over the engine speed range is a common way to express the performance of an engine, seen in Figure 2.1, where engine load is increased at a given engine speed to a point where further increase would result in a decrease in engine speed.

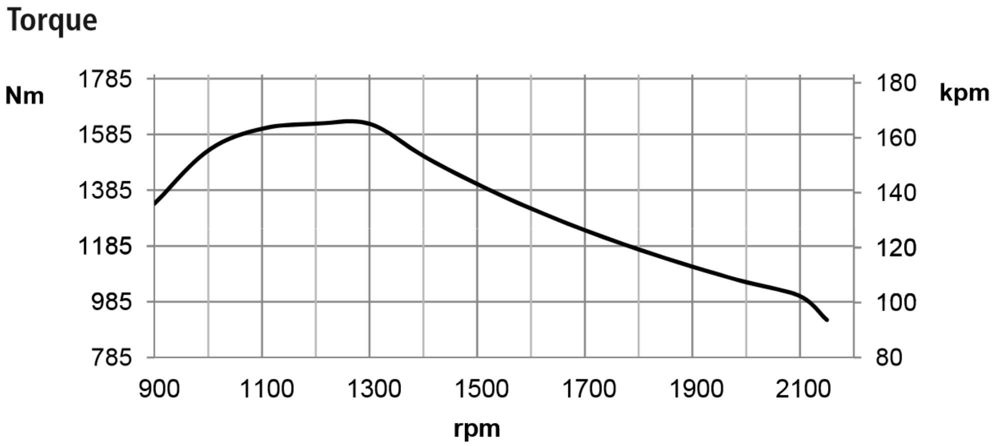

Figure 2.1: Steady-state torque profile for Scania DI09 072M 220kW

2.1.2 Transient Events

A transient event can be defined as the transition from one load and speed (steady-state operating condition) to another. This makes the task of systematically testing the transient performance complex and time consuming due to the large amount of conditions and combinations that can be tested. During a transient event both load and speed can vary as a function of time, and the development of the engine states will depend on the states from the previous engine cycle. Moreover, transient testing requires faster data acquisition and more control of the applied loading compared to the steady-state case [6].

Rakopoulos and Giakoumis [6] classifies transient tests in two categories:

- Speed increase
- Load increase

A comparison of the torque development for a load- and a speed increase transient is given in Figure 2.2. For the speed increase event a step in reference engine speed is given to the governor, while the load remains constant or increases moderately as a function of engine speed. A speed increase transient will cause the engine to accelerate due to the torque surplus throughout the transient which is evident in Figure 2.2.

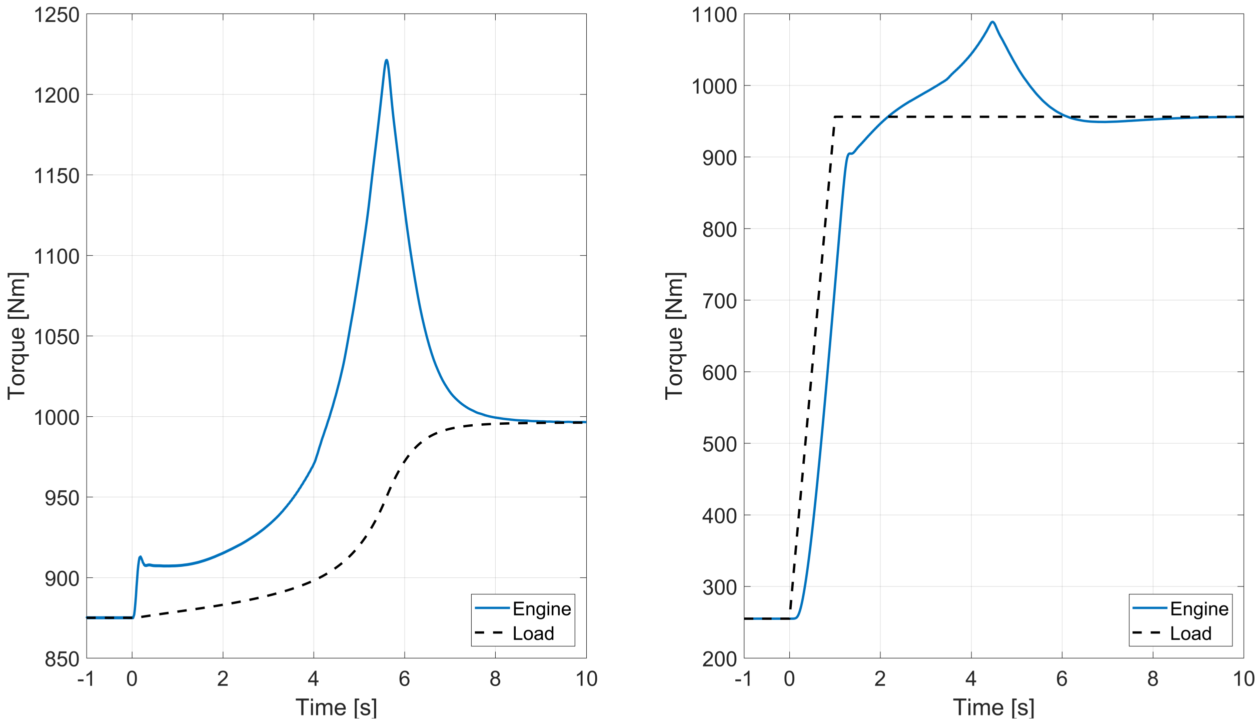

Figure 2.2: Comparison of torque development for speed increase (left) and load increase (right) transients

A load increase test involves having the governor set at a constant engine speed while an increase in loading is applied to the shaft. This transient event will initially cause the engine speed to drop due to the torque deficit between engine and load. The governor then senses the deviation from desired engine speed and increases the fueling until a torque surplus is generated to overcome the new load. The response of the system greatly depends on both the magnitude and and shape of the load increase.

To illustrate the differences between steady-state and transient performance a comparison of steady-state full load conditions and the actual transient development of torque against engine speed can be seen in Figure 2.3. This transient is the same as the speed increase transient shown in Figure 2.2. A large torque deficit between the steady-state full load and transient can be noted, and will be further discussed later in the chapter.

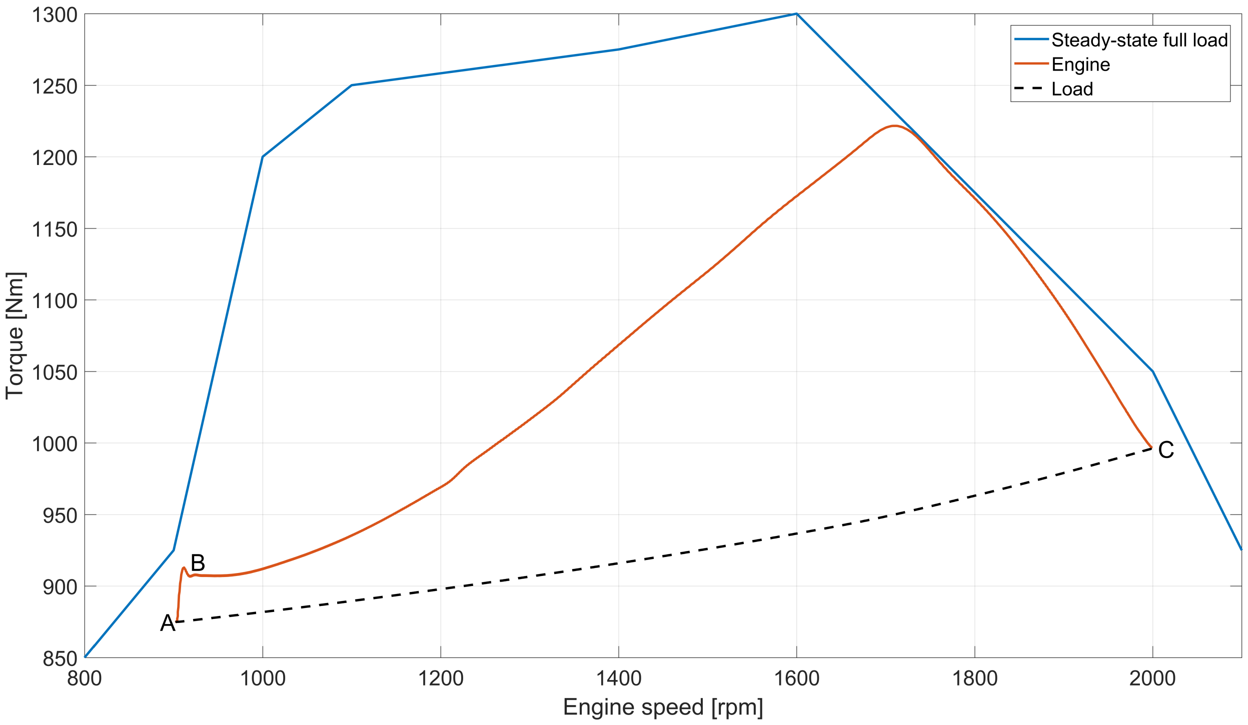

Figure 2.3: Comparison of torque development in a transient speed increase event and maximum steady-state torque

2.2 Benefits and Challenges of Engine Downsizing

Engine manufacturers have for the past decades been faced with increasingly stringent requirements regarding reduced emissions and improved fuel efficiency. Engine downsizing has shown to be an effective way of meeting these requirements. Downsizing involves using a smaller displacement engine with higher specific load, enabled by forced induction. The result is a more efficient engine, but the downside is a deterioration of engine response and low engine speed performance.

The improvements in fuel consumption and emissions can, in short, be attributed to reduced frictional losses, and less heat transfer across cylinder walls, as well as reduced pumping losses [7]. Reduced frictional losses and heat transfer is a result of the smaller engine having less piston-cylinder friction with fewer cylinders and or, smaller bore stroke dimensions. In addition, a small but significant positive pumping work will improve the efficiency if the increased intake pressure exceeds the exhaust pressure [8].

In the case of throttle operated engines at part loads, much of the improvements in specific fuel consumption are a result of reduced pumping losses as the smaller engine is less throttled [2]. In other words, the peak efficiency island is moved closer to steady-state driving conditions, i.e. a car cruising on the highway in high gear. These conditions are typically at low engine speeds and relatively low loads which are in the bottom left region of Figure 2.4. The figure shows normalized brake specific fuel consumption (BSFC) contours against normalized torque and speed operating points for a baseline unit on the left, and a turbocharged 40 % downsized engine on the right.

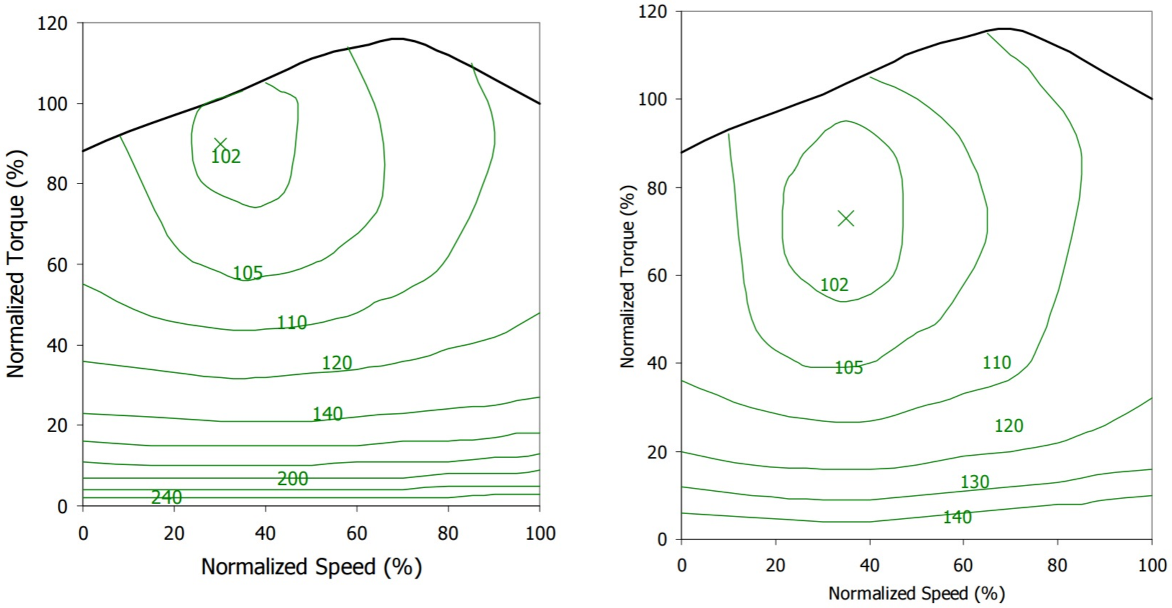

Figure 2.4: Contours of normalized brake specific fuel consumption for a baseline unit (left) and downsized (right). Retrieved from Shahed and Bauer [2]

BMEP is a performance metric relating the displacement V_d and the rated brake torque Tq_r of an engine [9], and can be interpreted as a displacement-normalized capacity to do work. From equation (2.1) we note that a smaller down-sized engine can produce the same brake torque as a non-downsized (baseline) unit, with an increased BMEP, where the increased BMEP is realized by a pressure charging system. Thus, the maximum BMEP of an engine is a good indication of its degree of downsizing.

$$BMEP = \frac{T q_r 4\pi}{V_d} \tag{2.1}$$

The compression ignition diesel (CI) engine has several features that favor high degrees of pressure charging, and can therefore achieve larger BMEP values than the spark ignition gasoline (SI) engine. These include low sensitivity to air-fuel ratio variations allowing lean operation, the absence of throttling, high torque, and tolerability in peak cylinder pressures and temperatures [6]. As a result, pressure charged CI engines are the preferred engine for medium-large applications, including marine propulsion. Figure 2.2 shows thermal efficiencies for a variety of engine types, indicating the high thermal efficiencies of turbocharged diesel engines.

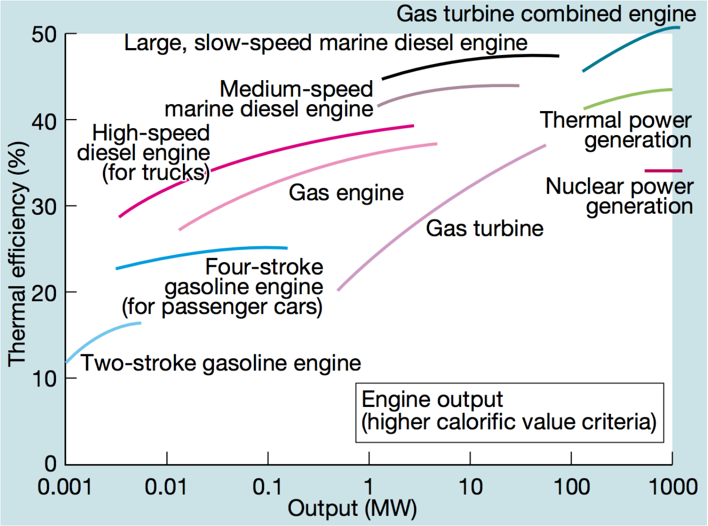

Figure 2.5: Thermal efficiencies of various types of engines. Retrieved from Takaishi et al. [1]

Even though a downsized turbocharged engine can achieve similar medium to high-speed steady-state performance as its baseline counterpart it will not be able to produce the same low-speed performance. According to Shahed and Bauer [2], a downsized turbocharged engines low speed maximum steady-state torque will be limited by the compressors surge line. This can be seen in Figure 2.6, where it is noted that the degree of downsizing further worsens low-speed steady-state performance. Surge and the surge line is explained in Section 2.4.1.

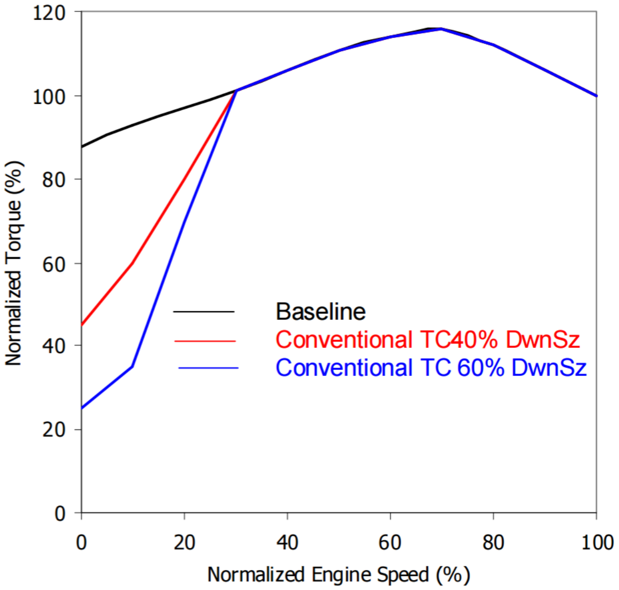

Figure 2.6: Comparison of maximum steady-state torque for baseline and downsized engines. Retrieved from Shahed and Bauer [2]

More interesting than steady state performance is how the engine behaves from one operating condition to the next. The transient response of turbocharged engines is characterized by a delay commonly referred to as turbo-lag. The delay is a result of the various dynamic delays associated with spooling up the turbocharger system. The responses shown in Figure 2.2 and 2.3 are all affected by turbo-lag, with the effect being more prominent in the speed increase event. The torque deficit in Figure 2.3 is a result of turbo-lag and fuel limiting action, and will be worse for more downsized engines.

Much effort has been put into minimizing turbo-lag while still harvesting the benefits of increased engine efficiency, which is also the primary purpose of this thesis. Several methods have been proposed and implemented, a summary of what has been done to address the problem is given in Section 2.6.

2.3 Forced Induction

In a naturally aspirated engine, air enters the combustion chamber as a result of atmospheric pressure acting against the lower pressure in the cylinders. The lower pressure in the cylinders is generated as the piston moves from top dead center (TDC) to bottom dead center (BDC) during the intake stroke. In contrast, forced induction[1] engines increase the intake pressure to above atmospheric pressure, by use of either air-injection systems, mechanically driven superchargers, exhaust gas driven turbochargers, or a combination of these. The density of air ρ assuming an ideal gas is given by equation (2.2), where P is the pressure, R_s the specific gas constant, and T the temperature.

$$\rho = \frac{P}{R_s T} \tag{2.2}$$

From equation (2.2) we see an increased intake pressure effectively increases the density of the intake air. Boost pressure is a term commonly used to indicate the amount the intake pressure exceeds atmospheric pressure. With more air in the cylinder, more fuel can be injected and combusted at the same air-fuel ratio increasing the power output of the engine. This can be illustrated in a cylinder pressure-volume (P-V) diagram. Figure 2.7 compares the dual combustion cycle of a naturally aspirated and supercharged engine, where 1-2 indicate compression, 2-4 combustion, and 4-5 expansion. It is seen that the boosted engine starts off with a pressure higher than ambient (1'), from 2'-4' the boosted engine with more air can burn more fuel generating a larger peak pressure. It follows that the net work output may be calculated from the integral $W = \int P dV$, in other words, the area inside the cycle which is larger for the supercharged engine [8].

---

[1] In this thesis, the words forced induction, pressure charging, and supercharging are used interchangeably to describe engines with a system to increase the inlet air density.

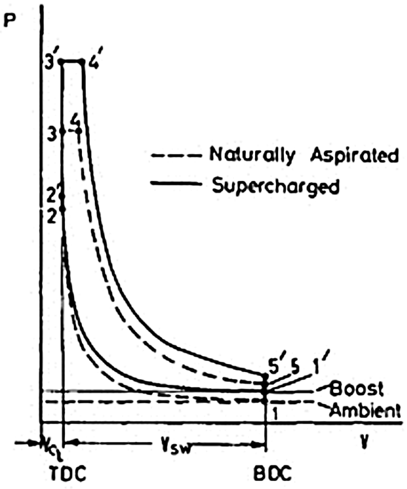

Figure 2.7: P-V diagram comparison of ideal dual-combustion for naturally aspirated and boosted engine. Retrieved from Watson and Janota [8]

2.4 Turbocharging

Due to its efficiency, the turbocharger has shown to be the most successful and popular realization of pressure charging. In short, it utilizes untapped energy in the exhaust to compress air into the engine. In terms of efficiency, this is advantageous over, for example, a mechanically driven supercharger which consumes part of the shaft power to drive the compressor.

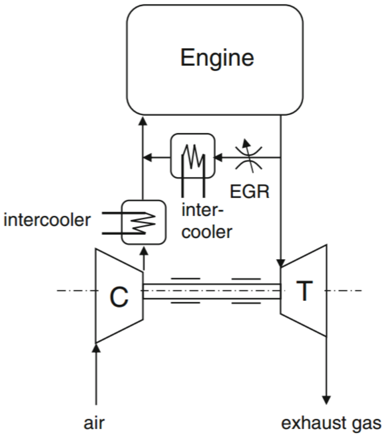

Figure 2.8: Schematic diagram of a turbocharger system with exhaust gas recirculation and intercooler. Retrieved from Nguyen-Schäfer [10]

A turbocharger consists of three main components, a turbine, a compressor and the center housing and rotating assembly (CHRA). The CHRA houses the shaft connected to the turbine and compressor, including a bearing- and a cooling/lubrication system to handle the high rotational speeds of the turbocharger, which range from 3000 rpm in large industrial machines all the way up to 350 000 rpm in automotive engines [10]. The turbine converts parts of the exhaust gas to mechanical energy which in turn drives the compressor at the cost of slightly increased pumping losses in the form of back pressure. The compressor then generates an increased pressure in the intake manifold.

It is common to use a charge air cooler (intercooler) to lower the temperature of the airflow from the compressor before it enters the engine. This further increases the density of air in the cylinder, see equation (2.2), hence power potential. A schematic diagram of the turbocharger system with exhaust gas recirculation (EGR) and intercooler can be seen in Figure 2.8. EGR is an emission reducing system for turbocharged diesel engines to limit nitrous oxide (NOx) emissions by re-burning some of the exhaust gases.

2.4.1 Turbocharger Matching

This section aims to explain how various turbocharger dimensions affect engine response, and how they are selected to match a turbocharger to a particular engine.

To ensure good performance, efficiency and stability engine manufacturers need to carefully select the best fit turbocharger for the given engine. The task is challenging as several design factors need to be balanced to achieve best possible performance for a wide range of operating conditions and transient events. A wide range of operating conditions implies operation over a wide range of air flow rates. However, the performance of a turbocharger depends on the angle the flow enters the turbine rotor and compressor impeller. Hence, a turbocharger will have optimal performance for a specific region of flow rates or operating points. Thus the matching procedure involves optimizing the turbocharger system to provide a best over-all performance for the particular application [8].

Turbocharger Performance Maps

Matching is usually done by simulating the engine together with compressor and turbine performance maps. The maps are experimentally obtained in turbocharger test benches and give the interrelationship between corrected turbocharger rotational shaft speed N_{corr}, isentropic efficiency η, corrected mass flow rate $\dot{m}_{corr}$, and pressure ratio Π. The corrections result from dimensional analysis, decoupling the maps from the experiment specific ambient temperatures and pressures, making them valid for other conditions [11][12].

Following the turbocharger air path, the subscripts 1, 2, 3, and 4 are used to denote variables before the compressor, before the engine, after the engine, and after the turbine respectively as seen in Figure 2.4.1.

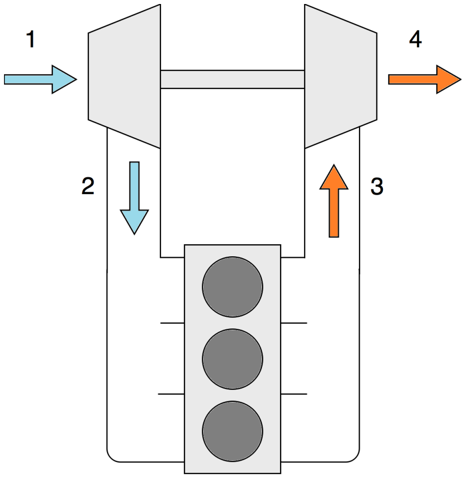

Figure 2.9: Diagram of turbocharger air path with corresponding subscripts

The compressor map is central in the matching process as it defines the most efficient operating area as well as the limitations of the compressor. The four performance variables related to the compressor map are the corrected mass flow $\dot{m}_{c,corr}$, the corrected shaft speed $N_{c,corr}$, the compressor pressure ratio Π_c, and the compressor isentropic efficiency η_c. The corrected mass flow for the compressor can be calculated from the actual compressor mass flow $\dot{m}_c$ by equation (2.3), where T_{1ref}, P_{1ref}, T_1 and P_1 indicated the experiment specific ambient temperature and pressure, and the actual ambient temperature and pressure respectively.

$$\dot{m}_{c,corr} = \dot{m}_c \frac{\sqrt{\frac{T_1}{T_{1ref}}}}{\frac{P_1}{P_{1ref}}} \tag{2.3}$$

The corrected shaft speed is defined in equation (2.4), where N is the actual turbocharger rotational speed.

$$N_{c,corr} = N \frac{1}{\sqrt{\frac{T_1}{T_{1ref}}}} \tag{2.4}$$

The compressor pressure ratio Π_c is given by equation (2.5) where P_2 is the downstream pressure.

$$\Pi_c = \frac{P_2}{P_1} \tag{2.5}$$

The compressors isentropic efficiency η_c is measure of how efficiently gas is compressed compared to an ideal isentropic process, given in equation (2.6), where γ_a is the isentropic exponent, or the ratio of specific heats for the charge air, and T_2 the downstream temperature.

$$\eta_c = \frac{\left(\frac{P_2}{P_1}\right)^{\frac{\gamma_a - 1}{\gamma_a}}}{\frac{T_2}{T_1} - 1} \tag{2.6}$$

The limitations of a compressor, namely surge, choke and maximum rotational speed are illustrated on the compressor map as boundaries of its operating region, see Figure 2.10.

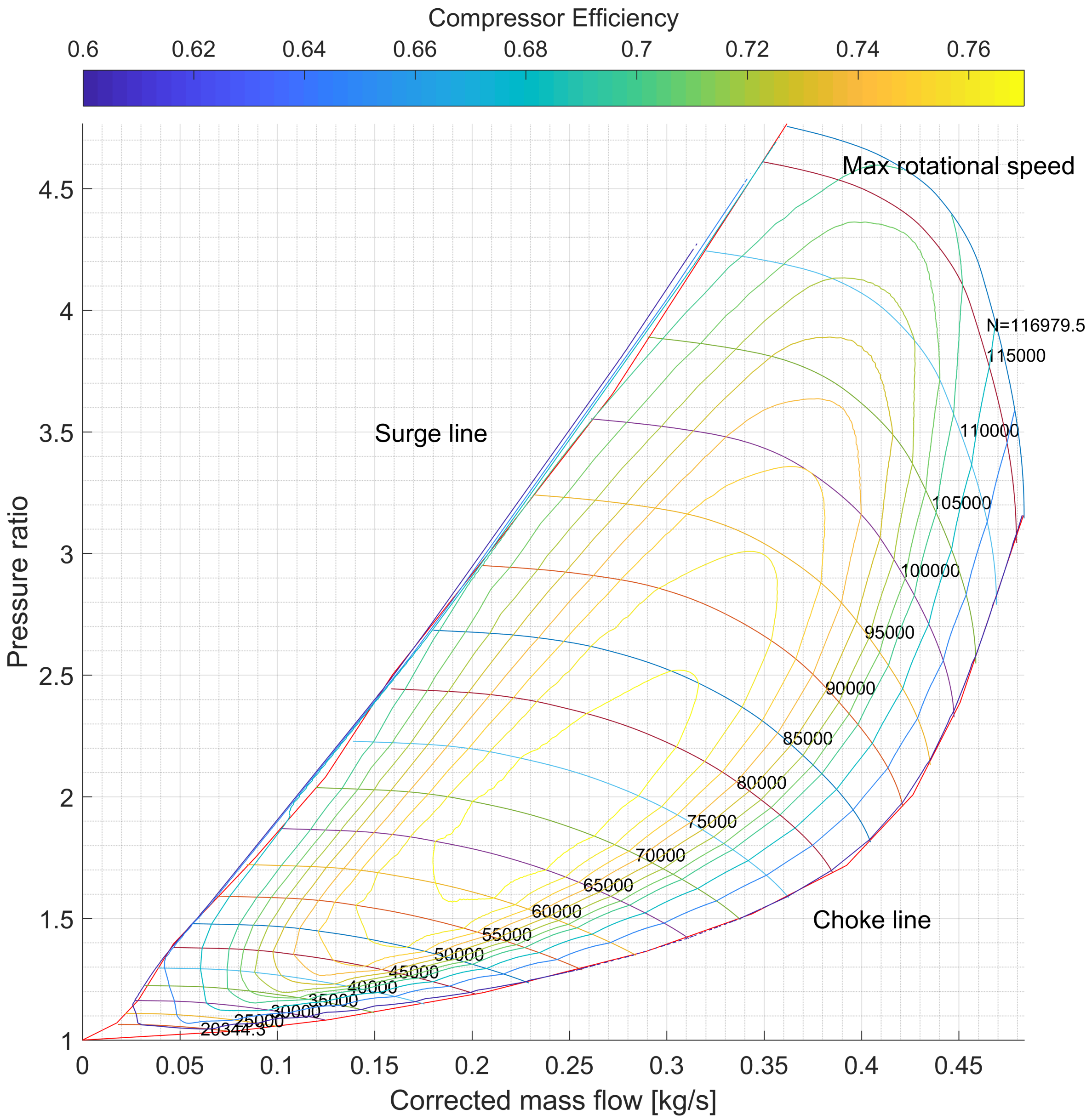

Figure 2.10: Compressor map for Scania DC1102 with indicated limits

The first limitation, surge, is a phenomena where the flow in the compressor wheel becomes unstable as the pressure generated becomes larger than the compressor can maintain. The phenomena is characterized by periodic fluctuations of mass flow rate and discharge pressure, resulting in significant performance drops and potential damage to the turbocharger due to vibrations and torsional loads to the shaft. The reduction of maximum low speed steady-state torque in downsized engines discussed previously is a result of this limitation. Choking is the second limitation, a condition when the flow reaches the speed of sound at some part of the compressor. This happens at high mass flow rates, and the mass flow rate can not be further increased without increasing the shaft speed [8]. The third and final limitation is the maximum rotational speed given by the mechanical restrictions of the device at high speeds from bearing capabilities and stress centrifugal forces.

The turbine map parameters are similar to those of the compressor map. The corrected turbine mass flow $\dot{m}_{t,corr}$ is given by equation (2.7), where T_{3ref}, P_{3ref}, T_3 and P_3 indicate the upstream exhaust temperature and pressure used when deriving the map, and the actual upstream exhaust temperature and pressure respectively.

$$\dot{m}_{t,corr} = \dot{m}_t \frac{\sqrt{\frac{T_3}{T_{3ref}}}}{\frac{P_3}{P_{3ref}}} \tag{2.7}$$

The corrected turbocharger shaft speed is given by equation (2.8).

$$N_{t,corr} = N \frac{1}{\sqrt{\frac{T_3}{T_{3ref}}}} \tag{2.8}$$

The turbine pressure ratio Π_t is given by equation (2.9), where P_4 is the downstream pressure.

$$\Pi_t = \frac{P_3}{P_4} \tag{2.9}$$

Finally, from thermodynamic equations the isentropic turbine efficiency is given by equation (2.10), where γ_e is the ratio of specific heats for the exhaust gas and T_4 the downstream temperature.

$$\eta_t = \frac{1 - \frac{P_3}{P_4}}{1 - \left(\frac{T_4}{T_3}\right)^{\frac{\gamma_e - 1}{\gamma_e}}} \tag{2.10}$$

A turbine map is given in Figure 2.11, where $\dot{m}_{t,corr}$ plotted against the turbine pressure ratio Π_t for constant turbocharger rotational speeds $N_{t,corr}$ on the left. On the right the turbine efficiency η_t is plotted against the turbine-blade-speed ratio $\tilde{c}_{us}$, given in equation (2.11), where r_t

is the mean turbine radius, and c_p the heat capacity at constant pressure [12].

$$\tilde{c}_{us} = \frac{r_t N_t}{\sqrt{2 c_p T_3 \left(1 - \Pi_t^{(1-\gamma_e)/\gamma_e}\right)}} \tag{2.11}$$

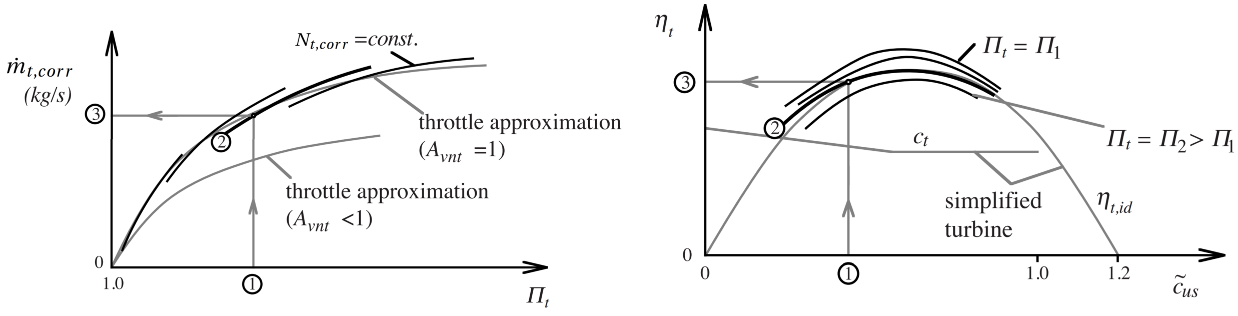

Figure 2.11: Simplified turbine map adapted from Guzzella and Onder [12]

On the turbine side, the matching procedure primarily involves selecting the optimal turbine area-radius ratio (A/R), where A is the inlet area, and R the radius from the turbine shaft to the center of the area illustrated in Figure 2.12. A small turbine A/R ratio will increase exhaust gas velocity improving turbine power at low speeds, consequently providing quicker boost buildup. However as the engine speed increases the turbine may exceed its maximum mechanical speed limit as well experiencing increased back pressure, worsening efficiency at high speeds. To prevent over-speeding and limit back pressure, many systems include a wastegate which redirects flow around the turbine if the exhaust pressure becomes too high. A negative aspect of bypassing flow is that exhaust energy that could be used to improve efficiency is wasted. One solution to this problem is variable geometry turbochargers (VGTs) which control the effective A/R ratio by control of active diffusers.

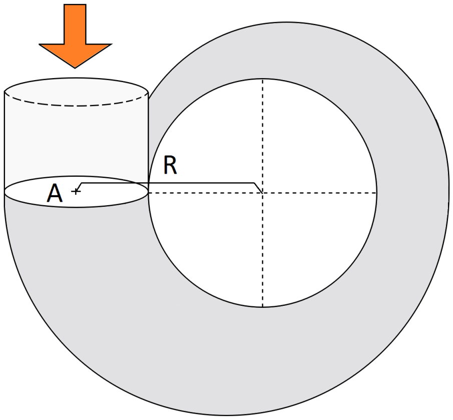

Figure 2.12: Turbine area and radius definition

The effect of increasing the A/R ratio, or similarly increasing the VGT diffuser angle, can be seen on the turbine map on the bottom right of Figure 2.13. A larger A/R ratio will increase the turbines maximum flow capacity, resulting in lower backpressure, better power, and efficiency at higher engine speeds, but will suffer from slow boost build-up as the lower flow rates have to overcome the inertia of the larger turbocharger. In general tuning the A/R ratio will be a compromise between torque at low speeds and power at high speeds [13].

Nguyen-Schäfer [10] gives a step-by-step procedure of turbocharger matching based on steady-state operating conditions. The whole process is summarized in Figure 2.13. First, the engine characteristics such as low-end torque, maximum torque, and nominal power are selected. For each of these operating conditions the required compressor mass flow rate[2] is determined by solving equation (2.12) for $\dot{m}_a$, where P, η_f, Q_f and $\frac{\dot{m}_f}{\dot{m}_a}$ is the engine power, combustion efficiency, fuel heating value and fuel-air ratio (FAR) respectively. The charge air density ρ_a is determined by equation (2.13), where η_v, V_d, and N_e is the volumetric efficiency, the engine displacement and engine speed in rotations per second respectively. Furthermore, the volumetric efficiency is given in equation (2.14), and is a measure of how efficient the intake process is [9], with m_a being the mass of air induced in the cylinder per cycle. The pressure ratio over the compressor Π_c can then be iteratively solved by equation (2.15). The pair of performance variables (Π_c,$\dot{m}_c$) can then be corrected and plotted on the compressor map. The value delta, δ, is then approximated by values for the operating condition of the engine together with a guessed turbocharger efficiency η_{TC}. The subscripts a and e indicate the specific heats for the air and exhaust gas respectively. This is then inserted in equation (2.16), together with Π_c to find the pressure ratio over the turbine Π_t. Based on equation (2.17) the mass flow of the turbine can be estimated and corrected. The pair ($\dot{m}_t$,Π_t) is then mapped onto the turbine map.

---

[2] With the absence of an intercooler we can use the same subscripts as defined previously. Where the mass flow of air $\dot{m}_a = \dot{m}_c$, and the charge air density $\rho_a = \rho_2$.

$$P = \dot{m}_a \eta_f Q_f \frac{\dot{m}_f}{\dot{m}_a} \tag{2.12}$$

$$\rho_a = \frac{2\dot{m}_a}{\eta_v V_d N_e} \tag{2.13}$$

$$\eta_v = \frac{m_a}{\rho_a V_d} \tag{2.14}$$

$$\Pi_c = \frac{\rho_a R_s T_1}{P_1}\left(1 + \frac{1}{\eta_c}\left[\Pi_c^{\left(\frac{\gamma-1}{\gamma}\right)_a} - 1\right]\right) \tag{2.15}$$

$$\Pi_c = \left(1 + \frac{c_{p,g}}{c_{p,a}} \underbrace{\frac{\dot{m}_t T_3}{\dot{m}_c T_1}\eta_{tc}}_{\delta} \left[1 - \Pi_t^{-(\frac{\gamma-1}{\gamma})_g}\right]\right)^{(\frac{\gamma}{\gamma-1})_a} \tag{2.16}$$

$$\dot{m}_t = \dot{m}_a \dot{m}_f = \dot{m}_a \left(\frac{AFR+1}{AFR}\right) \tag{2.17}$$

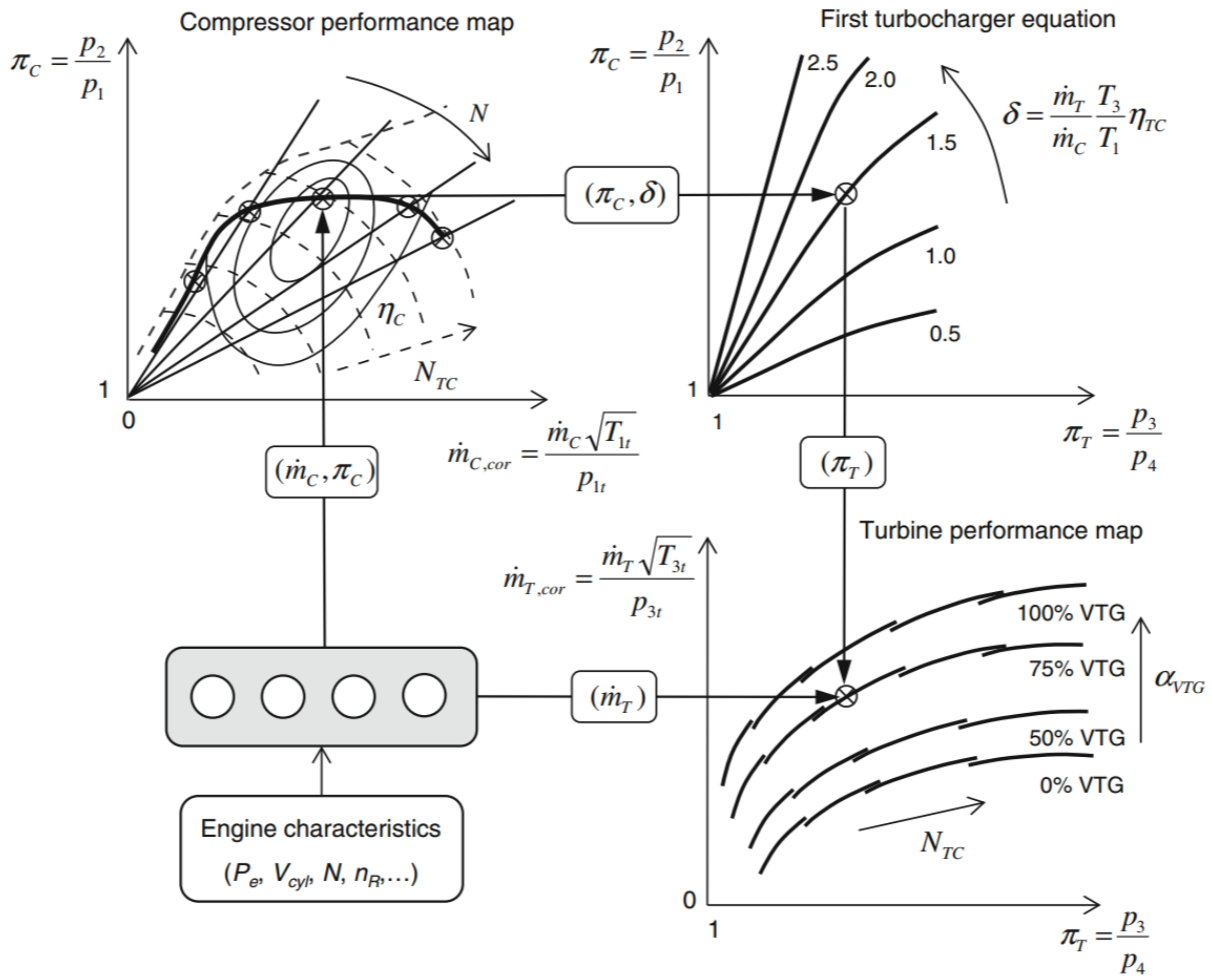
Compressor performance map
$\pi_C = \frac{p_2}{p_1}$
N
η_C
N_{TC}
1
0
(π_C, δ)
$(\dot{m}_C, \pi_C)$
$\dot{m}_{C,cor} = \frac{\dot{m}_C \sqrt{T_{1t}}}{p_{1t}}$
First turbocharger equation
2.5
2.0
1.5
1.0
0.5
$\delta = \frac{\dot{m}_T}{\dot{m}_C} \frac{T_3}{T_1} \eta_{TC}$
$\pi_T = \frac{p_3}{p_4}$
(π_T)
Turbine performance map
$\dot{m}_{T,cor} = \frac{\dot{m}_T \sqrt{T_{3t}}}{p_{3t}}$
100% VTG
75% VTG
50% VTG
0% VTG
α_{VTG}
$(\dot{m}_T)$
Engine characteristics
$(P_e, V_{cyl}, N, n_R, \ldots)$

Figure 2.13: Turbocharger matching procedure. Retrieved from Nguyen-Schäfer [10]

The whole process outlined above is iterated until guessed values converge. Different turbines and compressors can then evaluated by changing the maps used in the process. To summarize, the compressor is selected so that operation is within its constraints while the primary operating conditions are in the high-efficiency region. The turbine is selected such that the A/R ratio delivers required boost where the engine is most efficient.

2.5 Engine Control

The primary objectives of the diesel engine control system are to provide required torque as efficiently as possible while keeping the engine under safe operating conditions while also complying with exhaust gas emission regulations [12]. Several of these objectives contradict one another which makes the task of stating clear control objectives challenging. Often the control system is initially optimized for steady state conditions using maps relating the control parameters such as injection strategy, boost pressure and so on with engine speed and load. The control strategy under transient events will be more complex and have other requirements compared to steady state and depending on the type of operation. In operations where a fast torque and speed response is critical but conflicting with low emissions, a temporary increase of maximum allowable fuel-air ratio can be considered [6].

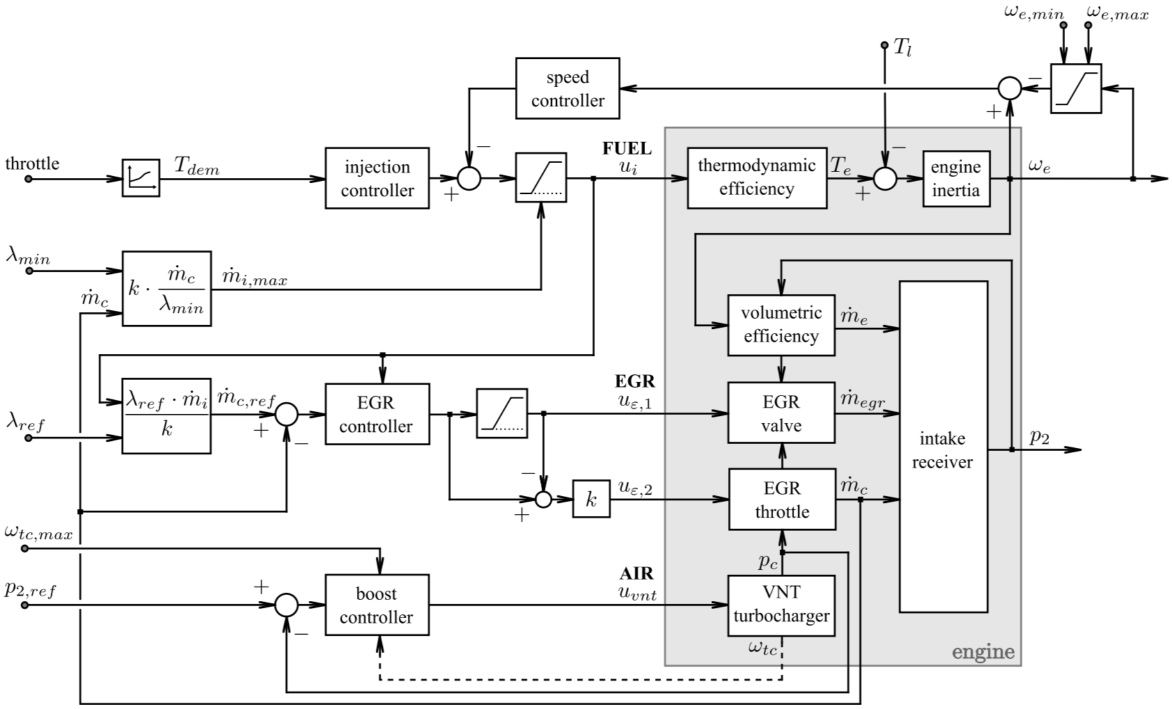
$\omega_{e,min}$
$\omega_{e,max}$
T_l
speed controller
throttle
T_{dem}
injection controller
FUEL
u_i
thermodynamic efficiency
T_e
engine inertia
ω_e
λ_{min}
$\dot{m}_c$
$k \cdot \frac{\dot{m}_c}{\lambda_{min}}$
$\dot{m}_{i,max}$
volumetric efficiency
$\dot{m}_e$
$\frac{\lambda_{ref} \cdot \dot{m}_i}{k}$
$\dot{m}_{c,ref}$
λ_{ref}
EGR controller
EGR
$u_{\varepsilon,1}$
EGR valve
$\dot{m}_{egr}$
intake receiver
p_2
k
$u_{\varepsilon,2}$
EGR throttle
$\dot{m}_c$
$\omega_{tc,max}$
$p_{2,ref}$
boost controller
AIR
u_{vnt}
p_c
VNT turbocharger
ω_{tc}
engine
+
−

Figure 2.14: Basic diesel engine control system structure. Retrieved from Guzzella and Onder [12]

A basic control structure for a turbocharged diesel engine with EGR and variable geometry/nozzle turbine (VGT/VNT) is seen in Figure 2.14, where Guzzella and Onder [12] highlighted three important control paths with bold letters, namely fuel, EGR, and air. In short, the fuel path determines the amount of injected fuel requested by the speed controller, while the EGR path controls the amount of exhaust gas to be recirculated to keep the combustion gas composition favorable for nitrogen oxide reduction. The air path is responsible for controlling either a wastegate, the position of the VGT diffusers, or fueling to keep the boost pressure and turbocharger speed within its operating limits, as well as controlling the engine backpressure. The model used in this thesis is equipped with neither EGR nor VGT. Hence its control system will mainly consist of the fuel path, coupled with the air path through a smoke limiter responsible for keeping the air-fuel ratio lean to avoid black smoke.

The smoke limiter is only active when the controller requests more fuel than is allowed by a specified maximum fuel-air ratio. Typically it activates for large steps in transient events starting at low loads and speeds, as is the case in Figure 2.3. As the step in engine speed is sensed by the controller, it quickly responds by increasing fueling resulting in a slight torque increase (A-B). However, the air supply to the engine does not respond as quickly due to the inertias of the turbocharger system. From B to 1600 rpm the air supply gradually increases, while the fuel limiter will respond by allowing more fuel to be injected while still keeping the system under lean conditions. From 1600 rpm to C the fuel limiter is no longer active.

The engine controller output for the same transient is given in Figure 2.15, where the dotted line indicates the limit imposed by the smoke limiter, the blue line the desired output and the red the actual output. The resulting fuel mass flow is also shown below.

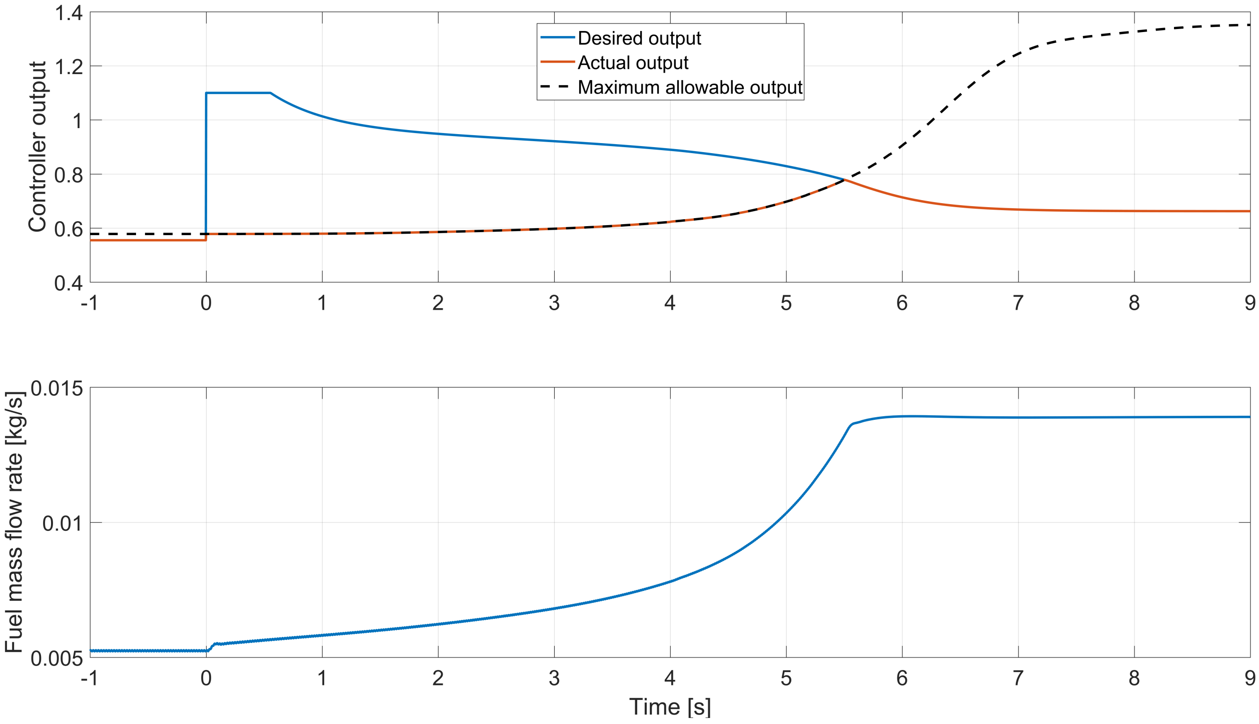

Figure 2.15: Controller output and fuel injection rate during a speed increase transient with active smoke limiter

2.6 Methods for Improving Transient Response

Several methods to improve the transient response of downsized internal combustion engines have been proposed. A short review of some of the methods and related work will be presented in this chapter. The methods discussed here include variable geometry turbine, air injection systems, multiple turbochargers, turbocharger compounding, and finally hybrid turbochargers.

In Figure 2.16 an overview of the dynamics during a transient event is shown. By either increasing the turbine exhaust gas energy or by assisting the compressor in delivering more air, the fuel limiting action is reduced ultimately leading to a faster response of the whole system.

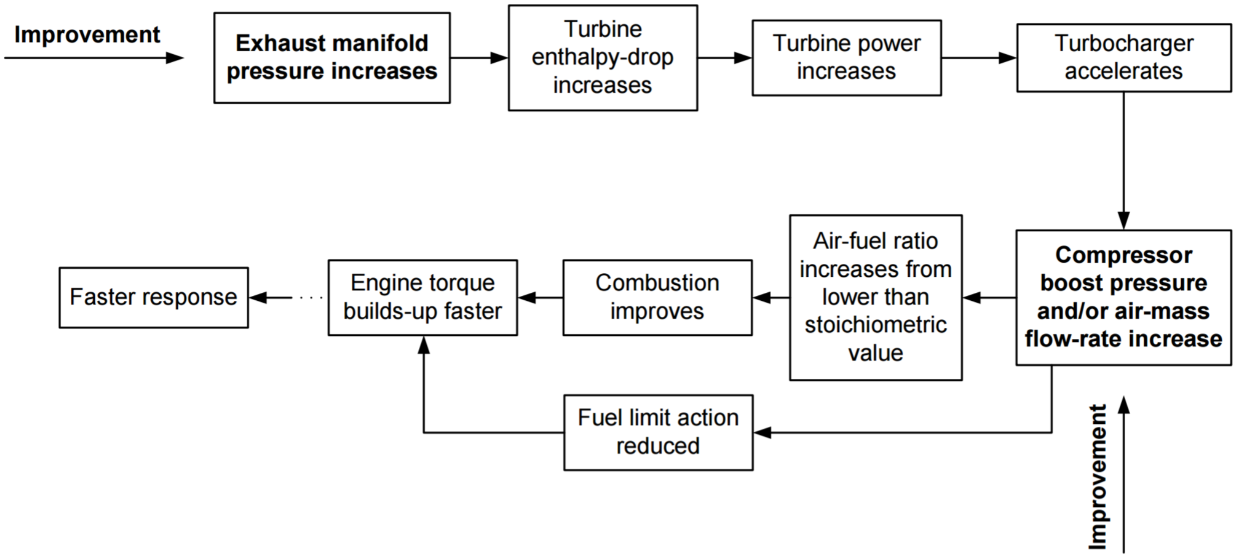
Improvement
Exhaust manifold pressure increases
Turbine enthalpy-drop increases
Turbine power increases
Turbocharger accelerates
Compressor boost pressure and/or air-mass flow-rate increase
Air-fuel ratio increases from lower than stoichiometric value
Combustion improves
Engine torque builds-up faster
Faster response
Fuel limit action reduced
Improvement

Figure 2.16: Cause and effect diagram of a turbocharger with response improvements. Retrieved from Rakopoulos and Giakoumis [6]

2.6.1 Variable geometry turbines

One option which has already been mentioned is VGT, which can be actively controlled to achieve favorable flow characteristics during a transient. In a simulation based study Filipi et al. [14] showed response improvements on 0-60 mph acceleration times for a 7.3l V8 CI truck, seen in Figure 2.17. A 2-second improvement over a conventional turbocharger can be seen from stand still to the end of first gear, where the turbo-lag effects are most prominent.

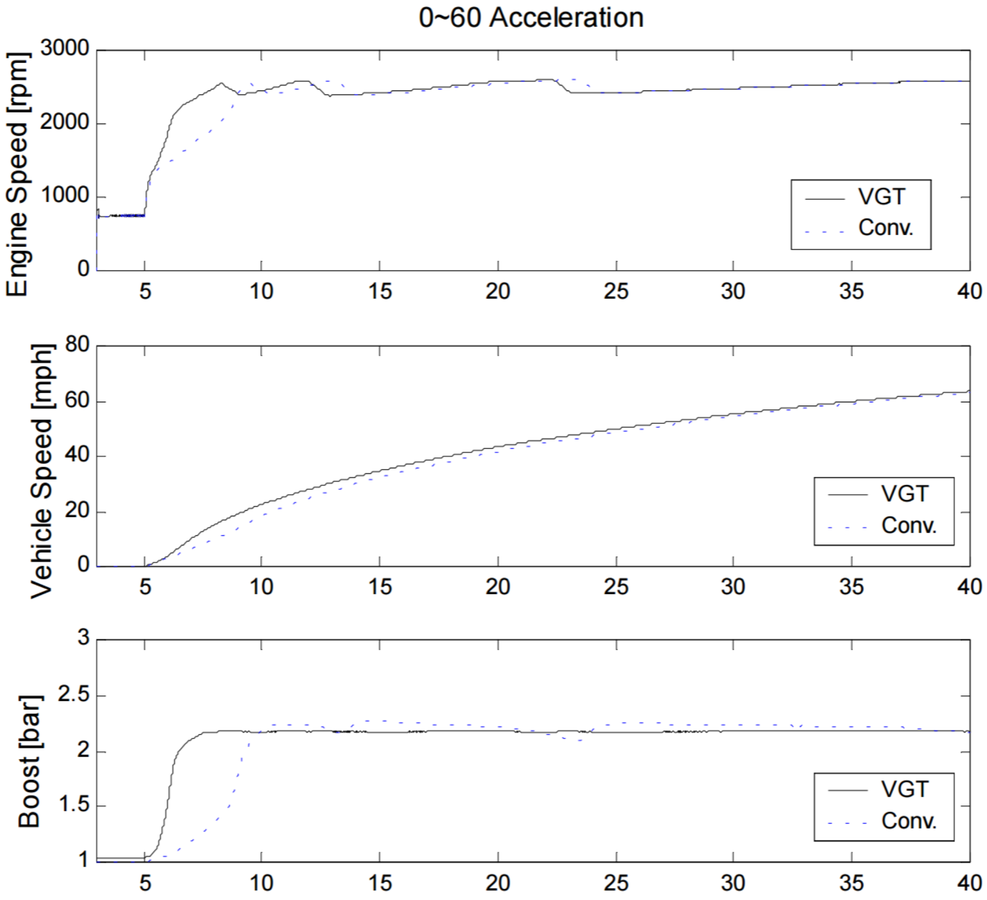

Figure 2.17: 0-60 mph response improvements by variable geometry turbine. Retrieved from Filipi et al. [14]

2.6.2 Air injection systems

Another solution is the use of gas pneumatic systems. Pressurized gas is stored in tanks and injected onto either the turbine, compressor or directly in the engine cylinder. Ledger et al. [15] showed that response times for load increase transients could be halved by injecting compressed air directly onto the compressor impellers. A schematic overview of an air injection system is given in Figure 2.18, where an external compressor keeps the tank pressurized. One challenge with air injection systems is the increased space requirements connected with the air tank.

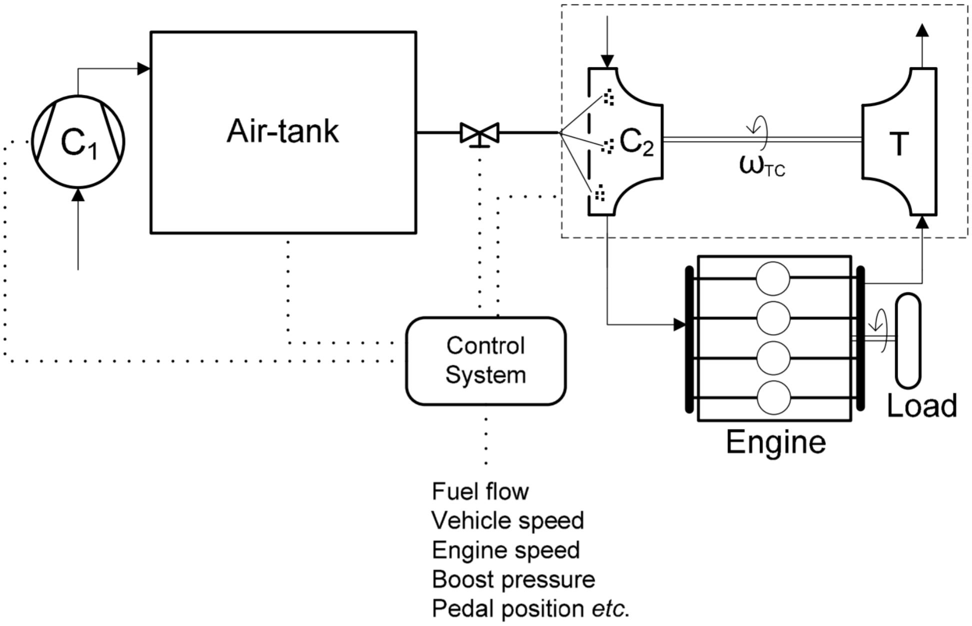
C1
Air-tank
C2
ωTC
T
Control
System
Engine
Load
Fuel flow
Vehicle speed
Engine speed
Boost pressure
Pedal position etc.

Figure 2.18: Schematic diagram of an air injection system in conjunction with a turbocharger. Retrieved from Rakopoulos and Giakoumis [6]

2.6.3 Combined Supercharging

The turbochargers efficiency advantage of the mechanical supercharger was briefly mentioned previously. However, an advantage of the mechanical supercharger is its ability to produce boost even at low engine speeds. The boost pressure generated by a mechanical supercharger is directly related to the engine speed, and pressure is readily available at low engine speeds. Combined supercharging is an attempt to merge the benefits of each. The mechanical supercharger assists the turbocharger at low speeds and is disengaged via a clutch mechanism at high speeds or low loads to maintain efficiency. Schmitz et al. [16] showed vehicular acceleration improvements of 30 % over conventional turbocharging. A schematic diagram of a combined supercharging system can be seen in Figure 2.19. The drawbacks of such a system are increased cost and space requirements.

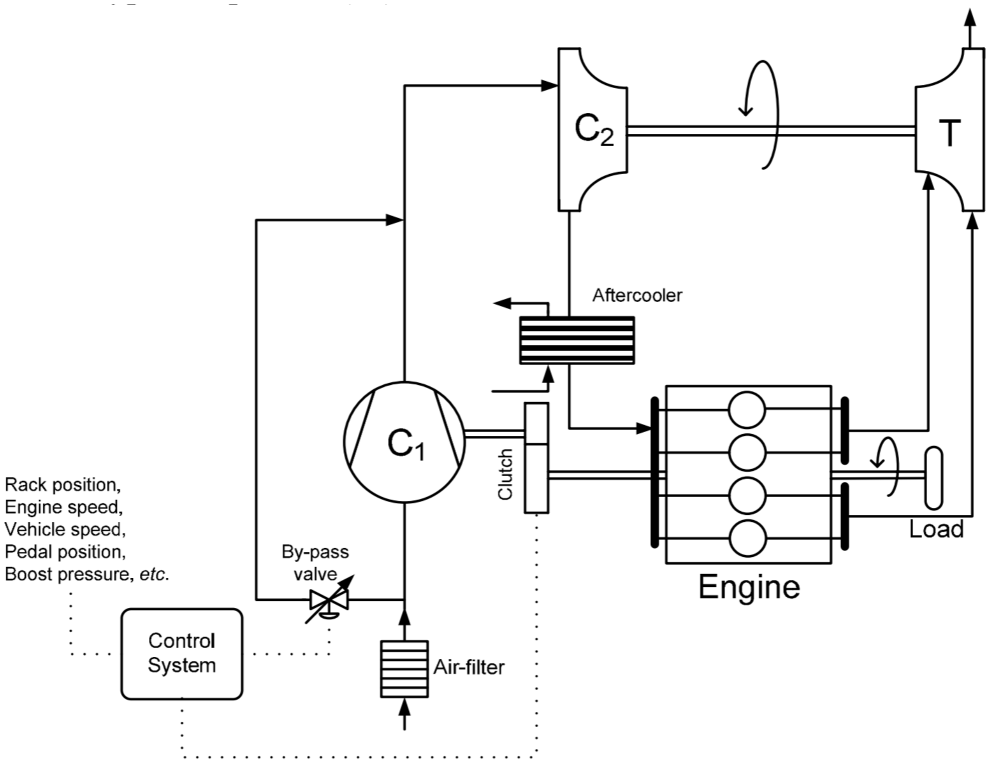
C2
T
Aftercooler
C1
Clutch
Rack position,
Engine speed,
Vehicle speed,
Pedal position,
Boost pressure, *etc.*
By-pass valve
Control System
Air-filter
Engine
Load

Figure 2.19: Schematic diagram of combined supercharging. Retrieved from Rakopoulos and Giakoumis [6]

2.6.4 Multiple Turbochargers

Assuming a turbocharger can be resembled by a cylinder with length D and diameter D its moment of inertia J_{tc} will be proportional to its diameter to the fifth power $J_{tc} \propto m_{tc}D^2 \propto \rho_{tc}D^5$, where m_{tc} is the turbochargers mass and ρ_{tc} the density of the turbocharger [10]. Hence a slight reduction of diameter will significantly reduce its moment of inertia while using lighter alloys for the construction will have less impact on the moment of inertia. One immediate effect of using multiple smaller turbochargers over a single larger unit is the lower total turbocharger moment of inertia. As will be shown later, a lower turbocharger inertia will contribute to improved transient response. There are several ways to configure multiple turbochargers, namely

- Twin/Bi configuration
- Two-stage configuration
- Sequential configuration

A Twin/Bi configuration is the most straight forward implementation, where n turbochargers in parallel run on, and feed $1/n$ cylinders each. The lower total turbocharger moment of inertia improves response compared to single turbocharger configuration. A downside common for all systems with multiple turbochargers are increased cost and space required.

Two-stage turbochargers run two turbochargers in series, with one low-pressure unit and one high-pressure unit, seen in Figure 2.20. This configuration is considered for applications requiring very high BMEP values and thus pressure ratios, such as large marine CI engines. The intake charge air and exhaust undergo two stages of compression and expansion respectively. This makes it possible generate high pressure ratios while maintaining efficiency over an acceptable flow range compared to a single stage high-pressure unit [8]. Response improvements come from the reduced turbocharger inertias connected with multiple smaller turbochargers. Downsides of two-stage configurations are more complex control and matching.

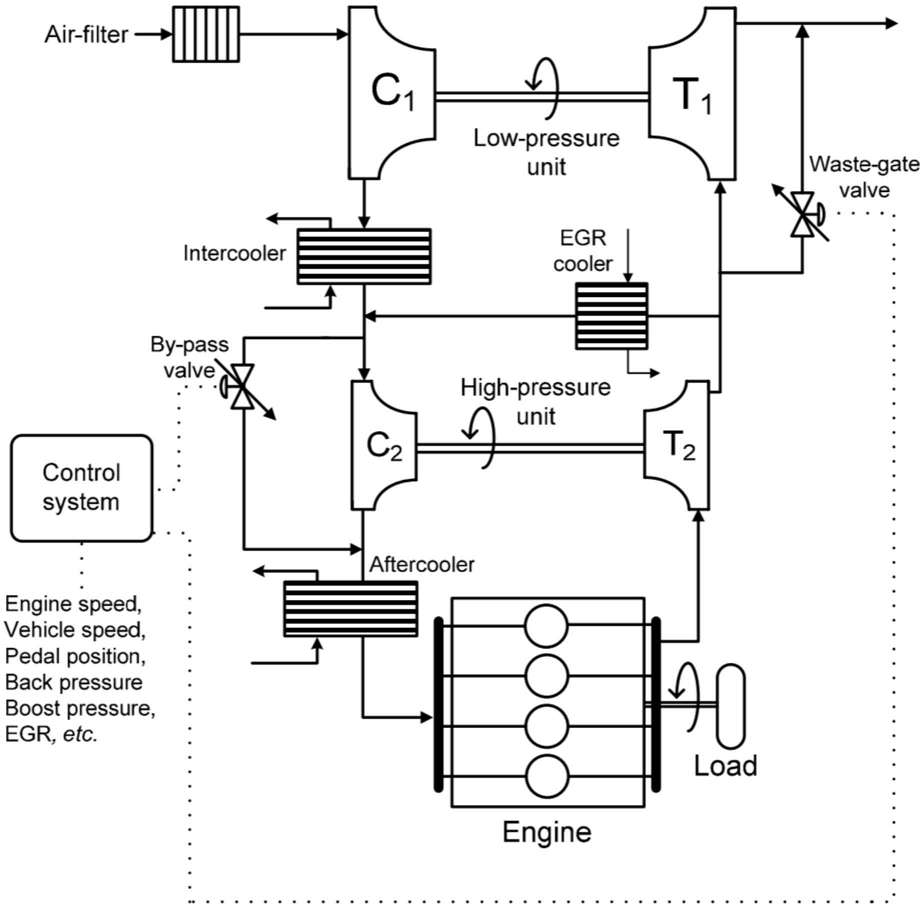
Air-filter
C1
T1
Low-pressure unit
Waste-gate valve
Intercooler
EGR cooler
By-pass valve
High-pressure unit
C2
T2
Control system
Aftercooler
Engine speed,
Vehicle speed,
Pedal position,
Back pressure
Boost pressure,
EGR, etc.
Load
Engine

Figure 2.20: Schematic diagram of a two-stage turbocharger configuration. Retrieved from Rakopoulos and Giakoumis [6]

A sequential arrangement consists of two turbochargers in parallel much like the twin/bi configuration, but with shared intake and exhaust manifolds. Together with controllable valves, this allows for activating either or both of the turbochargers depending on engine speed, effectively widening the flow range. A transient from low to high engine speed can then utilize one turbocharger for the first part of the transient and open valves connecting the second turbocharger for the final part of the transient. An arrangement of a sequential turbocharger scheme can be seen in Figure 2.21. The sequential system will like the two-stage system be more complex regarding matching and control.

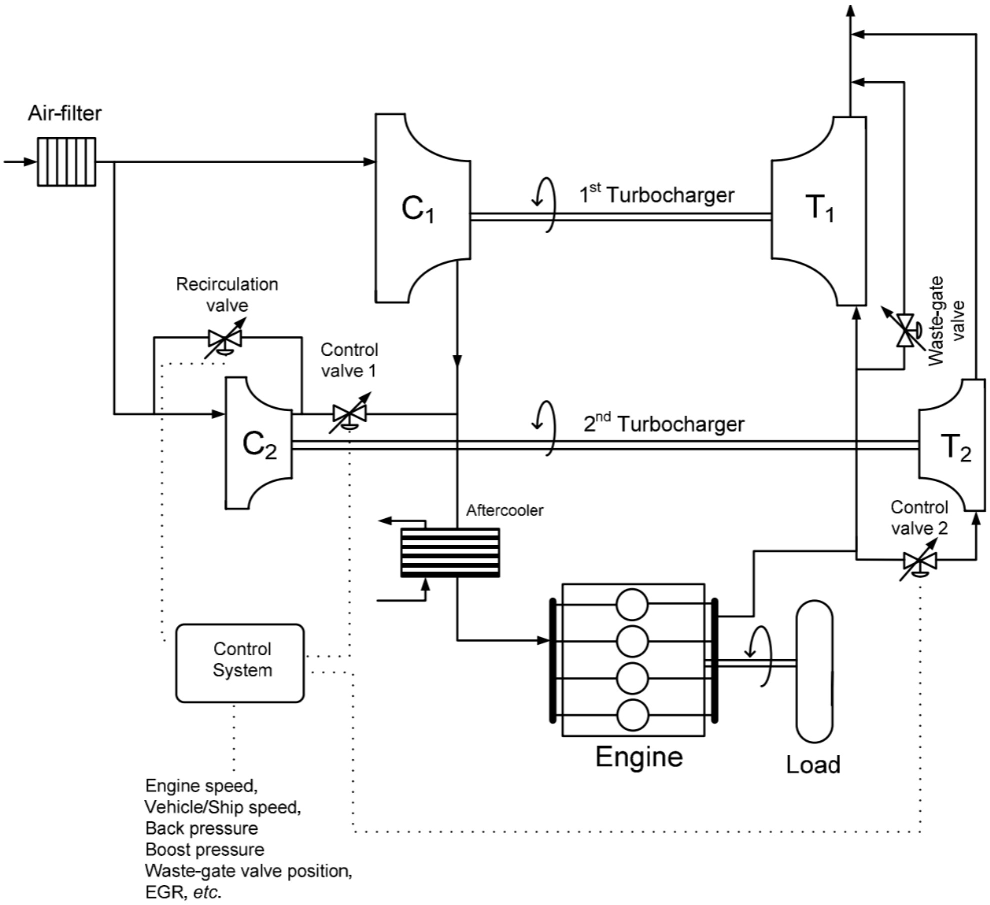
Air-filter
C1
1st Turbocharger
T1
Recirculation valve
Control valve 1
Waste-gate valve
C2
2nd Turbocharger
T2
Aftercooler
Control valve 2
Control System
Engine
Load
Engine speed,
Vehicle/Ship speed,
Back pressure
Boost pressure
Waste-gate valve position,
EGR, etc.

Figure 2.21: Schematic diagram of a sequential turbocharger configuration. Retrieved from Rakopoulos and Giakoumis [6]

Galindo et al. [17] compared the torque development for a 4-cylinder 2.2l CI engine with sequential and conventional turbocharging seen in Figure 2.22. It can be seen that improvements from the sequential charging scheme were comparable to that of a 2.7l conventional turbocharged engine.

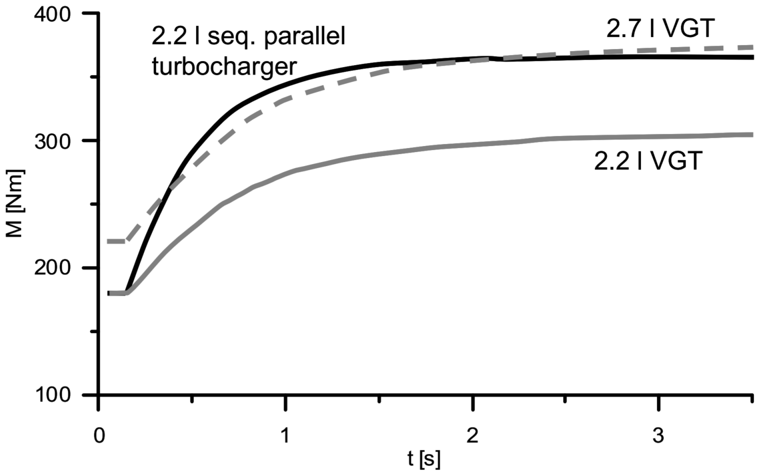

Figure 2.22: Comparison of torque development for a sequential turbocharged and conventional turbocharged engine. Retrieved from Galindo et al. [17].

2.6.5 Hybrid Turbochargers

With recent technological advances in high-speed motor designs, hybrid turbocharger systems have gained increasing interest and been subject to several studies over the past decade. Both the use of an electric motor to improve response and the use of a generator to extract and store excess exhaust gas energy at high speeds and loads has been studied. Two main configurations of hybrid turbochargers have been proposed, namely

- Electrically assisted turbochargers (EATC)
- Electrically assisted compressor (EAC)

The electrically assisted turbocharger consists of an electric motor/generator coupled to the turbocharger shaft. A schematic overview of the configuration is seen in Figure 2.23. During transients, the electric motor assists the turbocharger by accelerating the shaft. At high loads and speeds, the motor can work as a generator effectively doing the same job as a VGT or wastegate solution by imposing a counteracting torque on the turbocharger and harvest and store the energy at the same time.

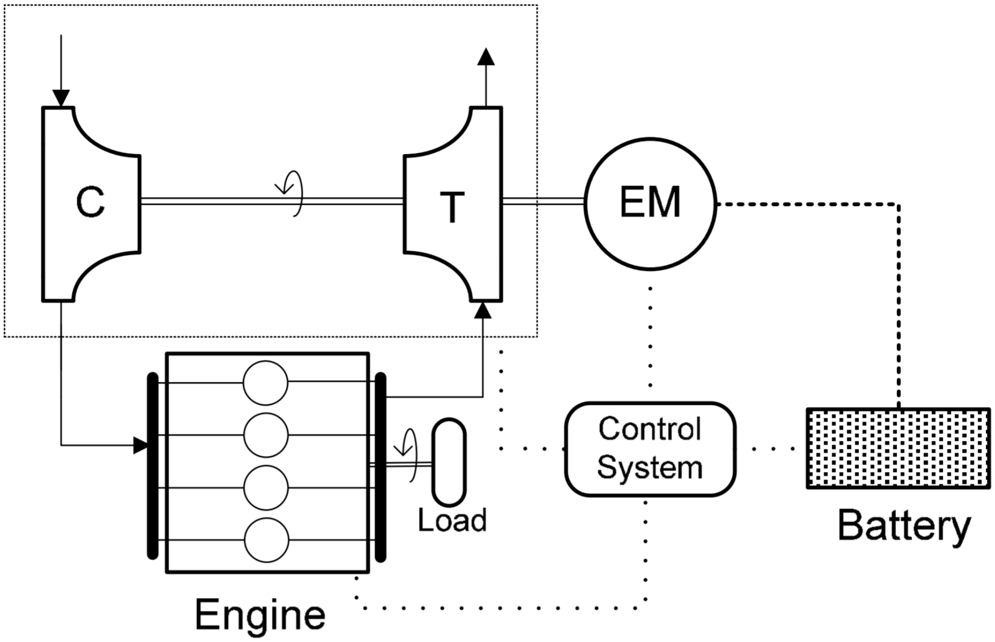

Figure 2.23: Schematic overview of the electrically assisted turbocharger configuration. Retrieved from Rakopoulos and Giakoumis [6]

An extensive study was performed by Millo et al. [3], where it was shown that an EATC improved the time to reach the desired boost level during a load increase by up to 30 %. The transient improvements obtained by Millo et al. [3] can be seen in Figure 2.24 for a 7.8l inline-6 CI engine. The same study also showed fuel consumption reductions by up to 5 % for driving cycles, by alternating between motoring and generating modes. An induction motor capable of producing 1 Nm up to 60 000 rpm, and a continuous power of 6.3 kW up to 120 000 rpm was used in this study and developed in Bumby et al. [18].

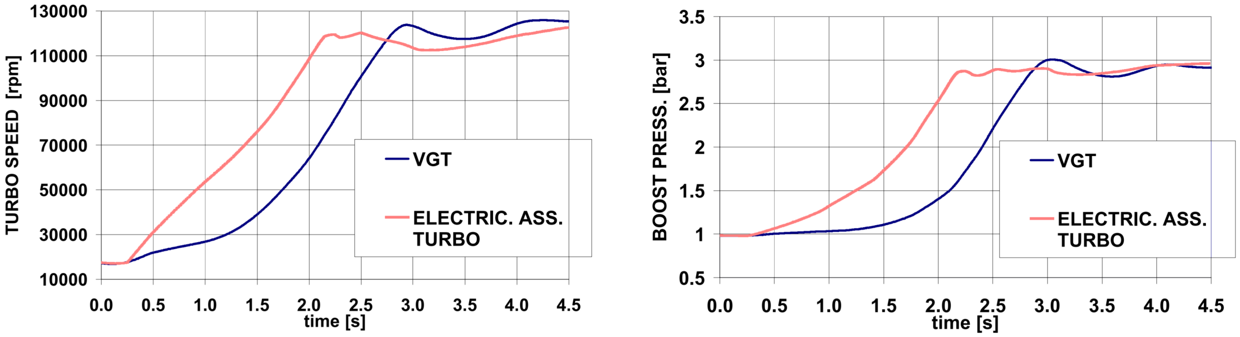

Figure 2.24: Turbocharger speed, and boost pressure response improvements by electrically assisting the turbocharger. Retrieved from Millo et al. [3]

Katrašnik et al. [4] did a similar study on a 6.9l inline-6 CI engine using two different asynchronous motors. The first motor (EM2) had half the torque to mass moment of inertia of the second motor (EM3), with a motor inertia of $J_m = 0.6$ kgcm^2 producing a maximum torque of 0.2 Nm and 0.4 Nm respectively. The response improvements obtained during vehicular acceleration for turbocharger speed, engine power, boost pressure and equivalence ratio λ[3] for the two motors assisting up to both 70 000 rpm, and 80 000 rpm can be seen in Figure 2.25

In terms of motor types used for assistance, both Millo et al. [3] and Katrašnik et al. [4] proposed a solution using induction machines (IM). Permanent magnet synchronous machines (PMSM) has also been developed for the same purpose in Noguchi et al. [19], and Noguchi et al. [20]. In short, the PMSM has higher efficiencies than the IM, whereas the IM has a construction better suited for high speeds and reduced cost compared to the PMSM. A comparison of the detailed dynamics and features of the two will not be covered by this thesis. However, a detailed comparison of the available high-speed motor technologies is given in Gerada et al. [21].

---

[3] In the remainder of this thesis the fuel-air equivalence ratio $F = 1/\lambda$ is used to describe the equivalence ratio.

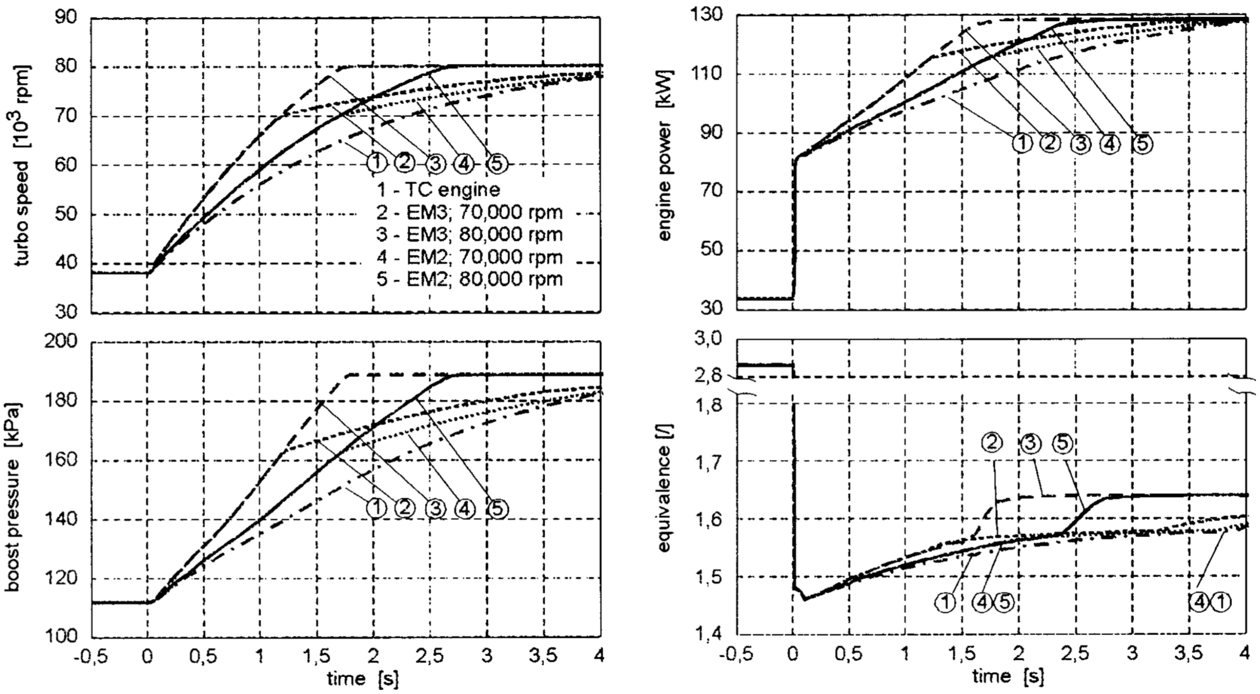

Figure 2.25: Vehicle acceleration response improvements for turbocharger speed, engine power, boost pressure and equivalence ratio obtained by Katrašnik et al. [4] with an EATC.

Münz et al. [22] proposed some challenges of the EATC while promoting the electrically driven compressor configuration. An EATC connected directly to the shaft has to cover the entire operating range of the turbocharger even when it is not in use, the induced voltages as a result of the rotational speed of the turbocharger could negatively effect the operation of the turbocharger. Also, re-balancing issues related to connecting a motor directly to shaft capable of rotating at very high speeds is avoided. The EAC uses a separate electrically powered compressor, seen in Figure 2.26, placed either up- or downstream of the turbocharger resembling the compressor side of the two-stage turbocharger scheme. Torque and boost pressure response improvements obtained by Münz et al. [22] can be seen in Figure 2.27. On the downside, the EAC configuration will be less compact than the EATC, and also have additional costs by requiring an additional compressor. Furthermore, it can not be used to extract energy at high speeds.

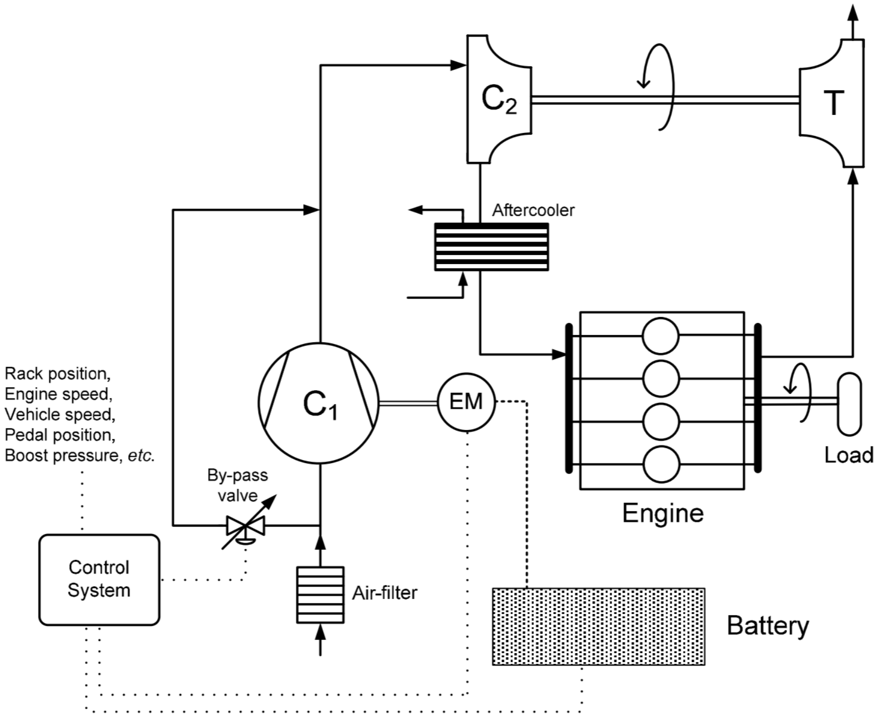
C$_2$
T
Aftercooler
Rack position,
Engine speed,
Vehicle speed,
Pedal position,
Boost pressure, *etc.*
C$_1$
EM
Load
Engine
By-pass
valve
Control
System
Air-filter
Battery

Figure 2.26: Schematic overview of the electrically driven compressor configuration. Retrieved from Rakopoulos and Giakoumis [6].

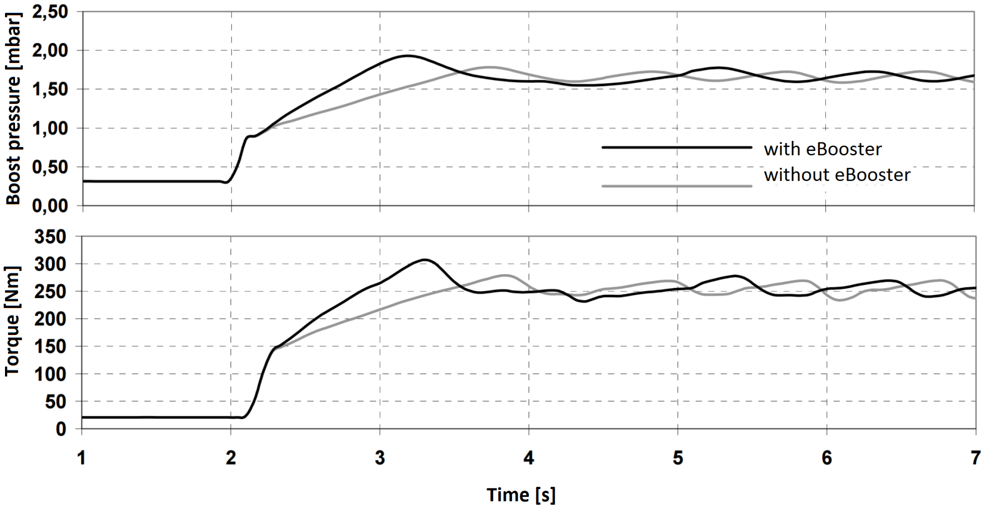

Figure 2.27: Response improvements for boost pressure build up and torque development using EAC. Retrieved from Münz et al. [22].

2.6.6 Comparison of systems

A comparison of the systems introduced above are summarized in Table 2.1 with their potential degree of response improvements and their challenges. Among the systems the hybrid turbocharger could be a competitive method.

Method	**Potential degree of response improvements**	**Challenges**
VGT	considerable	cost / control / matching
Air-injection	moderate	cost / space
Combined supercharging	considerable	cost / space
Twin/bi	considerable	cost / space
Two-stage	moderate-significant	cost / control / space
Sequential	moderate-significant	cost / control / space / matching
Hybrid turbocharging	considerable	cost / control

Table 2.1: Comparison of methods to improve transient response showing the potential response improvements and challenges. Adapted from Rakopoulos and Giakoumis [6]

Chapter 3

Hybrid Turbocharged Diesel Engine Model

Simulations of mathematical engine models are useful to gain an increased understanding of the dynamics of the machinery. In this thesis simulations are used as a tool to evaluate the electrically assisted turbocharger concept, aiding the early stages of the design process by providing design parameters and key insights before the concept could be realized on the real system. In the following sections, the bond graph and modified pseudo bond graph methods will be introduced followed by an explanation of the components in the dynamic process turbocharged diesel model. The assumptions that are made in the mathematical model are also mentioned.

3.1 Bond Graph as Modeling Framework

In this thesis, the bond graph method is used as the modeling framework for simulating the engines dynamic behavior. This framework is selected since the model itself, and its components have already been developed and refined over the years at NTNU, and will only need to be slightly modified to include the hybrid turbocharger. Furthermore, the model is of the zero-dimensional type, which means the spatial flow is not considered. Since there is a trade-off between model complexity and computational time the zero-dimensional model could be a proper choice with the objective being to show improved transient response with an EATC, and performing a parametric analysis on the parameters of the electrically assisted turbocharger (EATC). A zero-dimensional model can capture the general trends of variables of interest during transient operation with slightly slower than real-time computational speed [6].

3.1.1 General Bond Graph Method

The bond graph method is a graphical approach to model physical systems. The energy flow of the real system is identified and modeled with a set of basic elements connected with bonds. Each bond represents the instantaneous lossless power transfer between the connected basic elements. Where each basic element represents how the energy is stored, dissipated, supplied, and interchanged. A list of the basic elements, their constitutive laws, and physical examples are given in Table 3.1. In Table 3.1 it is seen that a physical effect in one energy domain is analogous to a physical effect in another energy domain; thus the same symbolism can be used to represent the power interaction regardless of energy domain.

Power is carried from one element to the other by the bond in the direction of the arrow through the power variables effort $e(t)$ and flow $f(t)$ who's product is the instantaneous power $P(t)$. Another set of variables which describe the state of the system are the energy variables. The energy variables momentum $p(t)$ and displacement $q(t)$ are defined as the the time integral of the power variables (3.1). Where $e(0)$ and $f(0)$ are the initial conditions.

$$
\begin{aligned}
p(t) &= \int_0^t e(t) + e(0)\,dt \\
q(t) &= \int_0^t f(t) + f(0)\,dt
\end{aligned}
\tag{3.1}
$$

Causality indicated by a vertical line at either end of a bond indicates which of the power variables are inputs or outputs of the basic elements, i.e. cause and effect. In Figure 3.1 it is seen how the causal stroke defines effort as input to B, flow as output of B, and the other way around for A. This causal information tells us something about the physical structure of the system and at the same time ensures the correct computational order of the variables.

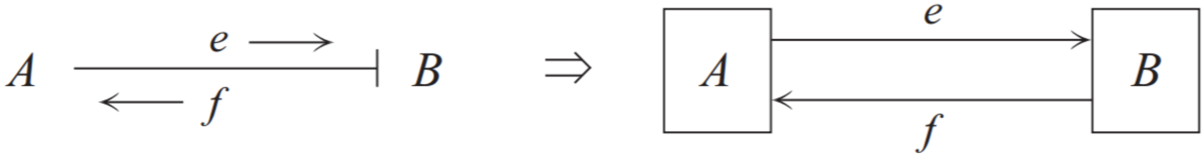

Figure 3.1: Causal stroke definition

Using an algorithm, the state-space model of the system can be obtained directly from the bond graph. The state space equations can then be solved to simulate the dynamics of the system [23].

Name	**Bond graph**	**Constitutive relations**	**Physical analogies**
Source effort	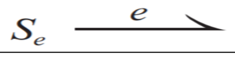	$e = e(t)$	Ideal source of effort
Source flow	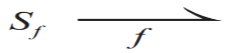	$f = f(t)$	Ideal source of flow
Capacitor	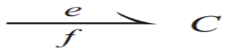	$e = \Phi_C(q)$	Spring, electrical capacitor, fluid storage tank
Inertia	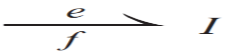	$f = \Phi_I(p)$	Mass, moment of inertia, electrical inductance, fluid inertance
Resistor	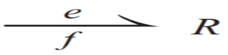	$e = \Phi_R(f)$	Damping, friction, heat transfer, electrical resistance
Transformer	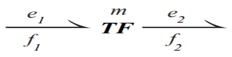	$e_1 = me_2$ $mf_1 = f_2$	Gears, piston crank mechanism, electrical transformer
Gyrator	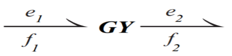	$e_1 = rf_2$ $ef_1 = e_2$	Conversion of energy in a DC motor
0 - junction	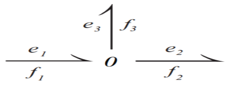	$e_1 = e_2 = e_3$ $f_1 - f_2 - f_3 = 0$	Electrical node
1 - junction	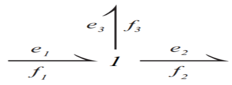	$f_1 = f_2 = f_3$ $e_1 - e_2 - e_3 = 0$	Common mass point in a physical system

Table 3.1: Basic bond graph elements

3.1.2 Pseudo Bond Graph Modified for Engine Process Modeling

The general bond graph approach can also be used to model thermo-fluid systems. If the product of the bond were to be true power as in the general approach, the effort variable would have to be temperature T and the flow variable the rate of change of entropy $\dot{S}$. For most engineering applications it is more common and intuitive to work with the effort variables pressure and tem-

Thermodynamic Property	**General Function**
Gas constant	R=R(P,T,F)
Enthalpy	H=H(P,T,F)
Internal Energy	U=U(P,T,F)
Entropy	S=S(P,T,F)
Specific heat capacities	C=C(P,T,F)

Table 3.2: Thermodynamic properties and the semi-empirical relations with the efforts

perature, and the flow variables mass/volume flow and energy flow. Karnopp [24] developed the concept of pseudo bond graphs by introducing additional bonds between the basic elements to include the more intuitive state variables mentioned above.

In Pedersen and Engja [25] a further modification of the pseudo bond graph is proposed to capture the transient behavior of engines efficiently, which is also the method used for the model in this thesis. Under the assumption that there is an excess of oxygen during combustion, the resulting product is a mixture of ideal gases, and dissociation occurs, the thermodynamic properties can be semi-empirically correlated to temperature, pressure, and fuel-factor F alone [26], as in Table 3.2. The fuel factor F is defined in equation (3.2) as the fuel-air ratio, over the stoichiometric fuel-air ratio f_s.

$$F = \frac{m_b}{m_{air} f_s} = \frac{m_b}{(m - m_b) f_s} \tag{3.2}$$

The state variables for the modified pseudo bond graph are given in Table 3.3, and the general constitutive relations for the C- and R-field is provided in Table 3.4.

Efforts	**Flows**	**State variables**
P - Pressure	$\dot{m}$ - Total mass flow	m - Total mass
T - Temperature	$\dot{E}$ - Energy flow	E - Total energy
F - Fuel-factor	$\dot{m}_b$ - Mass flow of burnt product	m_b - Total mass of burnt product
		V - Total volume

Table 3.3: State variables for the modified pseudo bond graph

Bond graph element representation	**Constitutive laws**
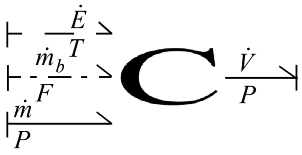 $\dot{E}$ T $\dot{m}_b$ F $\dot{m}$ P C $\dot{V}$ P	$P = \Phi_P(m, m_b, E, V)$ $F = \Phi_F(m, m_b, E, V)$ $T = \Phi_T(m, m_b, E, V)$
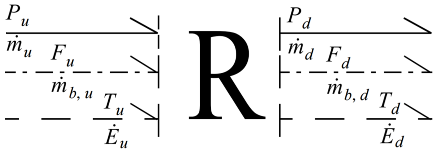 P_u $\dot{m}_u$ F_u $\dot{m}_{b,u}$ T_u $\dot{E}_u$ R P_d $\dot{m}_d$ F_d $\dot{m}_{b,d}$ T_d $\dot{E}_d$	$\dot{m} = \Phi_{\dot{m}}(P_1, P_2, F_1, F_2, T_1, T_2)$ $\dot{m}_b = \Phi_{\dot{m}_b}(P_1, P_2, F_1, F_2, T_1, T_2)$ $\dot{E} = \Phi_{\dot{E}}(P_1, P_2, F_1, F_2, T_1, T_2)$

Table 3.4: Constitutive laws for C- and R-fields. Figures adapted from Pedersen and Engja [25]

3.2 Model Implementation

The model is composed of several interconnected mechanical and thermo-fluid subsystems. The latter are represented as a series of control volumes, linked by valves that interchange mass and energy by the principles of conservation of energy and mass. This zero-dimensional flow assumption is also termed as a filling and emptying approach in the literature [9]. One assumption of the filling and emptying approach is that it does not consider the momentum of the gas flow. The neglection of gas momentum can be physically appropriate for engines with exhaust manifolds where the momentum of gas flow is not exploited by the turbocharger.

The mechanical subsystems exchange energy with the thermo-fluid system via the turbocharger shaft and the crank mechanism. An overview of the system is provided in Figure 3.2, showing the energy flow for the system, as well as which subsystems set efforts and flows via the causality strokes.

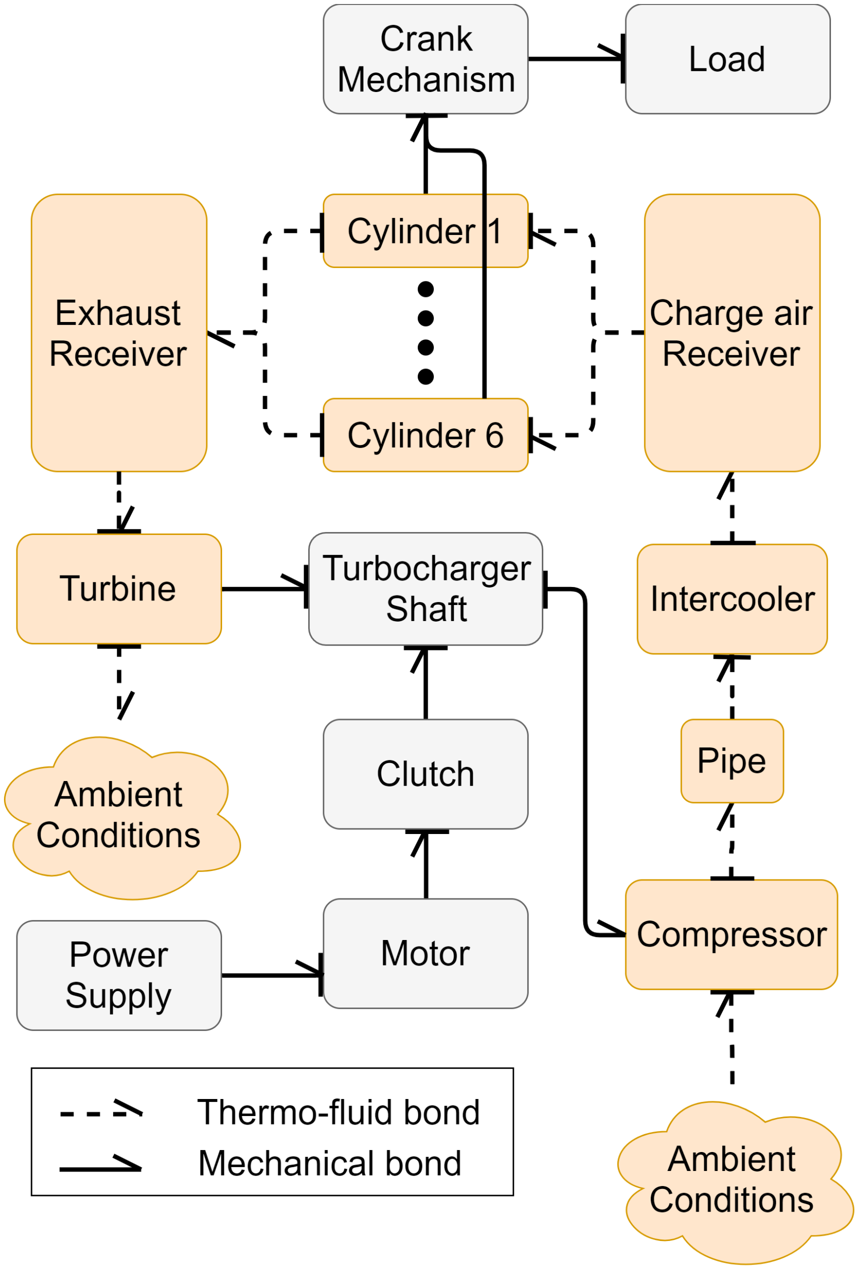
Crank Mechanism
Load
Exhaust Receiver
Cylinder 1
Cylinder 6
Charge air Receiver
Turbine
Turbocharger Shaft
Intercooler
Ambient Conditions
Clutch
Pipe
Power Supply
Motor
Compressor
Thermo-fluid bond
Mechanical bond
Ambient Conditions

Figure 3.2: Word bond graph for the engine model

3.2.1 Cylinder

An overview of the cylinder model is given Figure 3.3 together with efforts and flows. The dashed, blue, orange and black bonds represent thermo-fluid, hydraulic, thermal and mechanical rotation energy domains respectively.

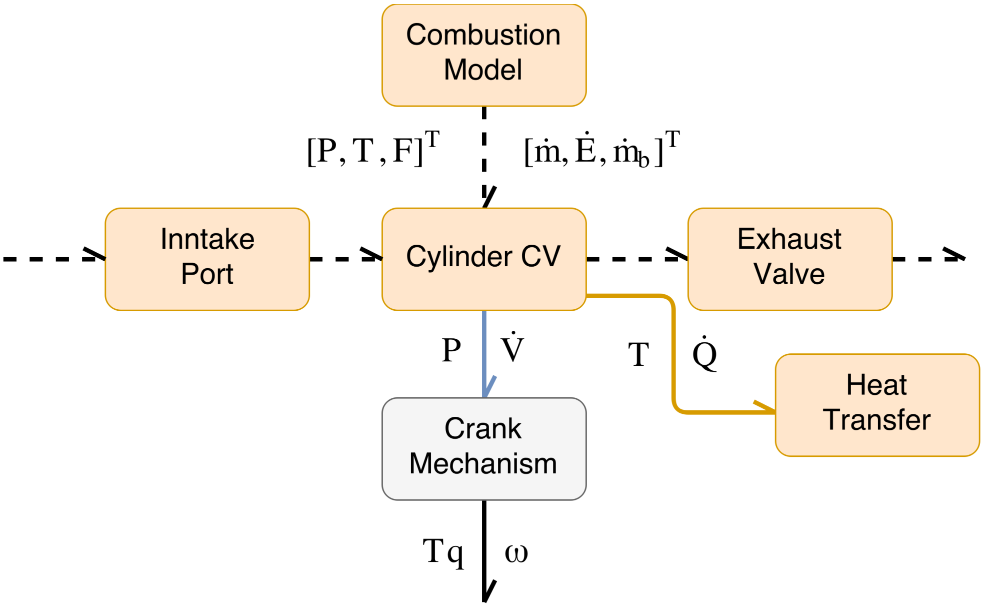
Combustion Model
$[P, T, F]^T$
$[\dot{m}, \dot{E}, \dot{m}_b]^T$
Inntake Port
Cylinder CV
Exhaust Valve
P
$\dot{V}$
T
$\dot{Q}$
Heat Transfer
Crank Mechanism
Tq
ω

Figure 3.3: Overview of cylinder model with sub-models

Cylinder Control Volume

The cylinder control volume is modeled as a gas accumulator, with the assumption of uniform pressure, temperature, and gas composition[1].

---

[1] This is often referred to as a single zone model in engine modeling literature.

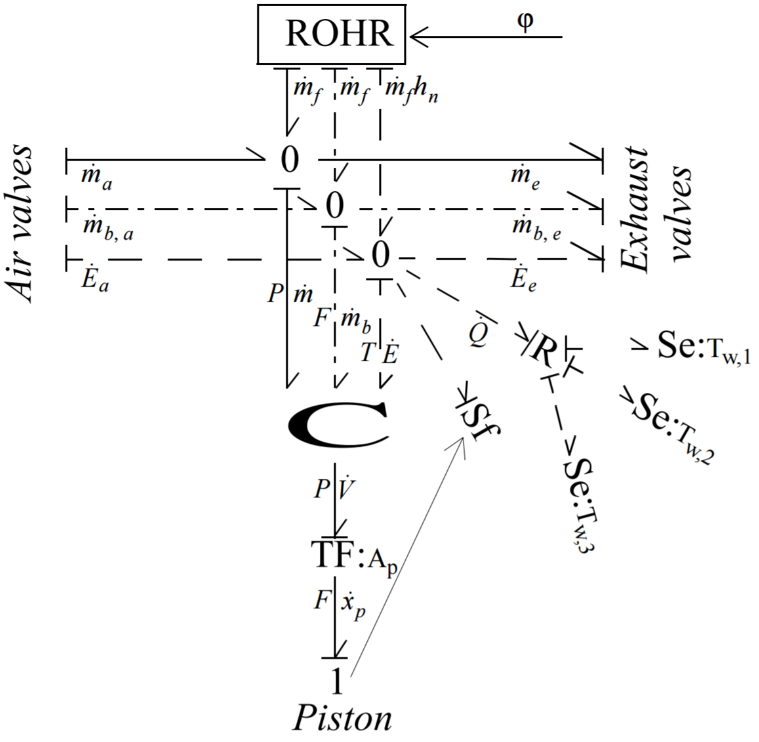
ROHR
φ
$\dot{m}_f$
$\dot{m}_f$
$\dot{m}_f h_n$
0
0
0
Air valves
$\dot{m}_a$
$\dot{m}_{b,a}$
$\dot{E}_a$
$\dot{m}_e$
$\dot{m}_{b,e}$
$\dot{E}_e$
Exhaust valves
P $\dot{m}$
F $\dot{m}_b$
T $\dot{E}$
$\dot{Q}$
R
Se:$T_{w,1}$
Se:$T_{w,2}$
Se:$T_{w,3}$
Sf
C
P $\dot{V}$
TF:A_p
F $\dot{x}_p$
1
Piston

Figure 3.4: Pseudo bond graph of the engine cylinder. Retrieved from Pedersen and Engja [25].

The bond graph for a cylinder control volume can be seen in Figure 3.4. The 0-junctions express the conservation of total mass, the mass of burnt product, as well as the first law of thermodynamics. Following the notation in the Figure 3.4 the resulting state equations are given in equation 3.3.

$$\begin{aligned}
\dot{m} &= \dot{m}_a - \dot{m}_e + \dot{m}_f \\
\dot{E} &= \dot{m}_a h_a - \dot{m}_e h_e - P\dot{V} + \dot{Q} + \dot{m}_f h_n \\
\dot{m}_b &= \dot{m}_{b,a} - \dot{m}_{b,e} + \dot{m}_f
\end{aligned} \tag{3.3}$$

The source flow element Sf added to the thermal 0-junction represents the work performed on the piston $P\dot{V}$ which is removed from the control volume. The C-field integrates the flows from the zero junctions to obtain the states of mass, internal energy, and mass of burned fuel as in equation (3.4), where subscript 0 denote initial states. With the time-varying volume in the case of a cylinder, the rate of change of volume is also integrated to get the volume of the cylinder

V_{cv}.

$$\begin{aligned} m &= \int \dot{m} + m_0 dt \\ E &= \int \dot{E} + E_0 dt \\ m_b &= \int \dot{m}_b + m_{b,0} dt \\ V_{cv} &= \int \dot{V} + V_0 dt \end{aligned} \tag{3.4}$$

The constitutive laws as given in Table 3.4 are then calculated. First, the specific internal energy u is calculated from the states of the control volume as in equation (3.5).

$$u = \frac{E}{m} \tag{3.5}$$

The temperature for the ideal gas can then be obtained by iteratively solving the implicit equation (3.6). Since the specific heat as a function of temperature $c_v(T)$ is monotonic increasing, iteration techniques such as NewtonRaphson converge quickly.

$$T = \frac{u}{\left(\frac{m-m_b}{m}\right) c_{v,a}(T) + \left(\frac{m_b}{m}\right) c_{v,b}(T)} \tag{3.6}$$

The obtained temperature is then used to equate the pressure according to (3.7). The specific gas constant is given as $R = \frac{R_0}{M}$, where R_0 is the universal gas constant and M the molecular mass of the component.

$$P = \frac{T}{V_{cv}} (mR + m_b R_b) \tag{3.7}$$

Finally the fuel factor is calculated according to equation (3.8) where f_s is the stoichiometric fuel-air ratio.

$$F = \frac{m_b}{(m - m_b) f_s} \tag{3.8}$$

Both the manifolds and the pipe connecting the compressor and intercooler are also modeled as gas accumulators. The calculation scheme is identical to that of the cylinder control volume with the exception of fuel injection, and a varying volume, hence their models will not be covered explicitly in this thesis.

Combustion Model

The combustion or rate of heat release (ROHR) model provides the mass flow of injected fuel $\dot{m}_f$ and the heat released from its combustion $\dot{m}_f h_n$. Furthermore, the mass flow of injected fuel is assumed to be burnt as it is injected. A combustion process can be divided into four stages, namely ignition delay, premixed combustion period, mixing controlled combustion period and late combustion period, seen in Figure 3.5.

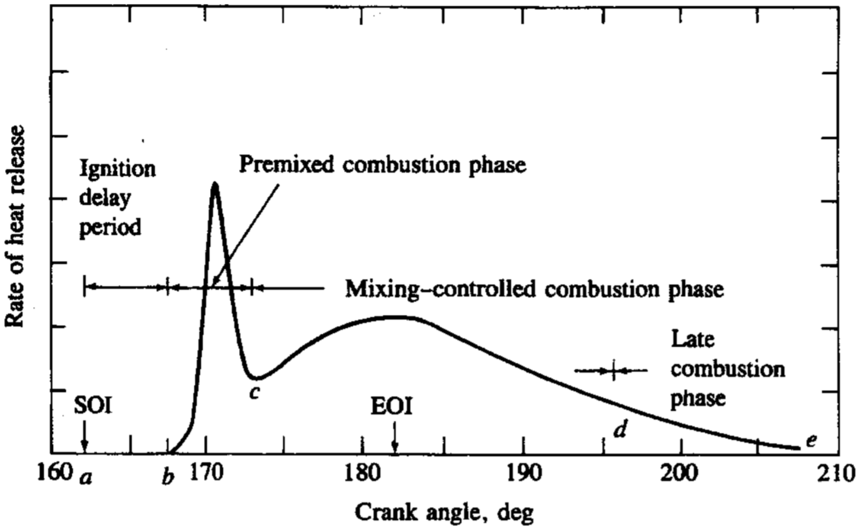

Figure 3.5: Stages of a typical CI engines combustion process as rate of released heat with respect to crank angle, with start of injection (SOI) and end of injection (EOI). Retrieved from Heywood [9]

The ignition delay τ_{id} can be calculated by the semi-empirical formula (3.9) proposed by Heywood [9]

$$\tau_{id} = aP^{-n}e^{\frac{E_A}{RT}} \tag{3.9}$$

where a and n are combustion specific parameters, and E_A is the activation energy required for autoignition. The ignition delay is converted to crank angle by $\phi_{id} = \tau_{id}\frac{180\omega}{\pi}$, where ω is the engine speed.

Based on the requested mass of fuel m_f to be injected by the engine controller, Wiebe parameters are calculated. Wiebe parameters express how heat is released based on the development of the crank angle like in Figure 3.5, and have to be fitted to the specific engine. The heat released from a single Wiebe function can be given as [25]

$$\dot{m}_f h_n = a\left(m_f h_n\right)(m+1)\,Y^m e^{aY^{m+1}} \tag{3.10}$$

with a, and m defining the shape of the Wiebe function, Y specifies the time from combustion start, and h_n the absolute fuel enthalpy. Dividing equation (3.10) by h_n we also also obtain an expression for the mass flow of fuel $\dot{m}_f$.

The model in this thesis is based on three Wiebe parameters since a single Wiebe function is not capable of producing the three distinct phases after ignition delay, as seen in Figure 3.5. The specific implementation of the three Wiebe parameters is given in detail in Yum [27].

The heat released and mass flow of fuel is then given by the Wiebe curve when the crank angle of the engine fulfills the inequality $\phi > \phi_{soi} + \phi_{id}$, where the crank angle for start of ignition ϕ_{soi} is a specified parameter. An example of the increasing mass flow rate of fuel $\dot{m}_f$ for the model during a speed increase transient can be seen in Figure 3.6, where we also note the three distinct phases.

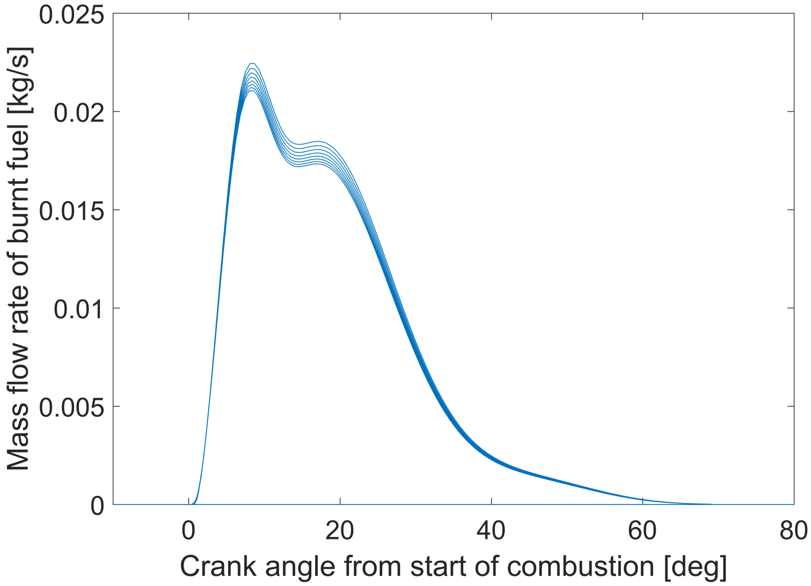

Figure 3.6: Development of mass flow rate of fuel $\dot{m}_f$ during a speed increase transient

Intake Port and Exhaust Valve

The intake port and exhaust valves act as restrictions connecting the cylinder control volume with the exhaust and intake manifold control volumes. The restriction determines the flow of mass and energy between the control volumes by the isentropic nozzle equation, given the pressures, temperatures and gas compositions on both sides. If we denote the pressure ratio Π as the downstream to upstream pressure

$$\Pi = \frac{P_d}{P_u} \tag{3.11}$$

the mass flow rate through the isentropic nozzle equation is given as [9]

$$\dot{m} = \frac{C_D A_R P_u}{\sqrt{R_u T_u}} \Pi^{\frac{1}{\gamma}} k \qquad k = \begin{cases} \left(\frac{2\gamma}{\gamma-1}\left[1-\Pi^{\frac{\gamma-1}{\gamma}}\right]\right)^{\frac{1}{2}}, & \text{if} \quad \Pi > \left(\frac{2}{\gamma+1}\right)^{\frac{\gamma}{\gamma-1}} \\ \sqrt{\gamma}\left(\frac{2}{\gamma+1}\right)^{\frac{\gamma+1}{2(\gamma-1)}}, & \text{otherwise} \end{cases} \tag{3.12}$$

where γ, and R_u are the ratio of specific heats for incoming flow and the specific gas constant for incoming flow respectively. C_D is the discharge coefficient and A_R the geometric valve flow area. The product $C_D A_R$ specifies the effective valve area A_{eff} which is in this model calculated according to

$$A_{eff} = aC_D(L_{valve})L_{valve} \tag{3.13}$$

where a is a constant depending on the valve design, L_{valve} is the valve lift which is given by a valve lift profile table relating valve lift to crank angle ϕ. The discharge coefficient also varies as a function of valve lift due to the geometry of the valve. For the specific parameters used the reader is referred to Yum [27]. An example of the effective area A_{eff} over an engine cycle is given in Figure 3.7 as a function of crank angle.

The calculation of mass flow of burnt product is given in equation (3.14), as the fraction of burnt product upstream times the calculated mass flow $\dot{m}$.

$$\dot{m}_b = \dot{m}\frac{f_s F_u}{1 + f_s F_u} \tag{3.14}$$

The conservation of energy yields the energy flow in and out of the nozzle as in equation (3.15), where h_{in} is the enthalpy given by the upstream pressure temperature and fuel factor as in Table 3.2.

$$\dot{E} = \dot{m} h_{in} \tag{3.15}$$

The equations are implemented using an R-field as seen in Table 3.1, with the additional signal input of the crank angle ϕ.

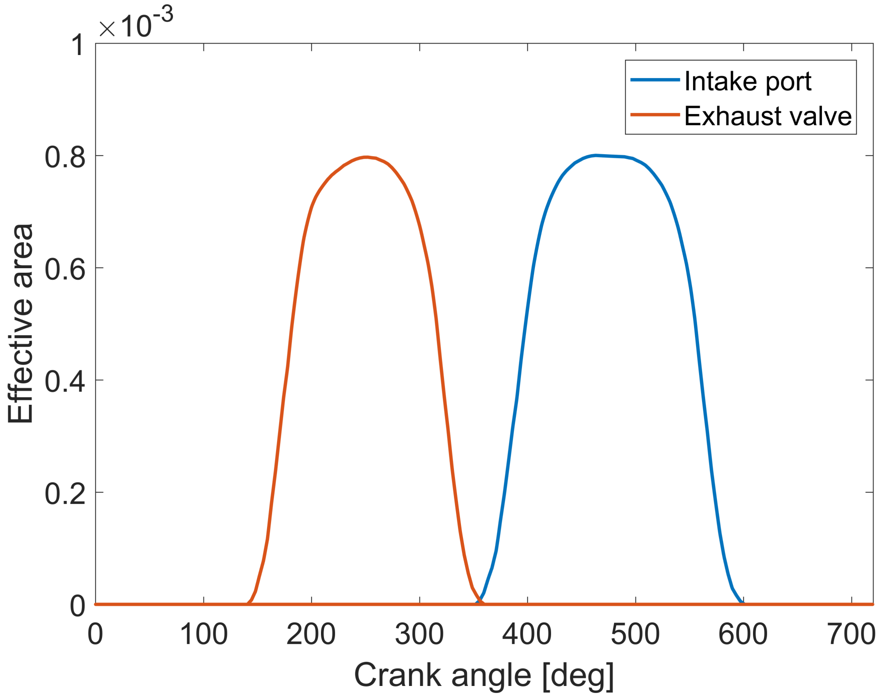

Figure 3.7: Effective area for intake and exhaust valve as a function of crank angle over one engine cycle

Heat Transfer

The heat loss in the cylinder is modeled as convective heat transfer from the cylinder gas to the cylinder wall by

$$\dot{Q} = hA(T_{cyl} - T_w) \tag{3.16}$$

where $\dot{Q}$ is the heat transfer rate, h the heat transfer coefficient, T_{cyl} the temperature of the gas in the cylinder, and T_w the temperature of the cylinder wall. The heat transfer coefficient for a cylinder-wall application is implemented as proposed by Finol and Robinson [28]

$$h = \alpha_{ht} C_m^{1/3} \sqrt{P_{cyl} T_{cyl}} \tag{3.17}$$

where α_{ht} is a factor for empirically correlating the model to the specific engine, $C_m = \frac{s\omega}{\pi}$ is the mean piston speed[2], and P_{cyl} the cylinder pressure. Furthermore, A is the area, consisting of the piston head, the cylinder top, and the cylinder liner, hence the total area as a function varying cylinder volume V is given by equation (3.18), where B is the bore of the cylinder.

$$A = 2\frac{\pi B^2}{4} + \frac{4V}{B} \tag{3.18}$$

The model is implemented with an R-element similar to the R-element in Figure 3.4.

Crank Mechanism

The crank mechanism transforms energy between the cylinder and the shaft. Figure 3.8 shows the transformation of energy between the energy domains from the hydraulic to the mechanical translation to the mechanical rotation and vice versa.

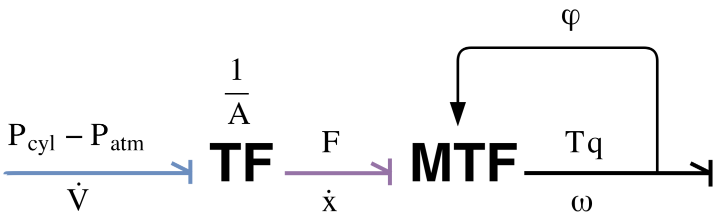

Figure 3.8: Bond graph implementation of the crank mechanism

The atmospheric pressure is subtracted from the cylinder pressure to obtain the net pressure working on the piston P. The transformation between the hydraulic and the mechanical translation power variables are given by the transformer modulus m_1, and the constitute relations below, where F is the force produced, $\dot{x}$ the speed of the piston, A is the area the pressure is working on and B the bore.

$$\begin{aligned} P &= m_1 F \\ m_1 \dot{V} &= \dot{x} \\ m_1 &= \frac{1}{A} = \frac{4}{\pi B^2} \end{aligned} \tag{3.19}$$

---

[2] Where s is the stroke, and ω the engine speed.

The transformation between the pistons linear translational energy and the shafts rotational energy is obtained from geometric properties of the crank slider mechanism seen in Figure 3.9. The kinematic relation m_2 is implemented as in equation (3.20).

$$m_2 = a + \left(\sin\phi \frac{\lambda \sin\phi \cos\phi}{\sqrt{1-(\lambda \sin\phi)^2}} \right) \tag{3.20}$$

Where a is the crank radius, l the connecting rod length, and lambda the ratio between the two $\lambda = \frac{a}{l}$. The constitutive relations give the following transformation

$$\begin{aligned} Fm_2 &= Tq \\ \dot{x} &= m_2\omega \end{aligned} \tag{3.21}$$

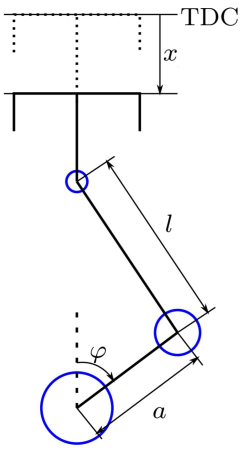

Figure 3.9: Crank slider mechanism indicating the crank radius a and the connecting rod length l. Retrieved from Yum et al. [29]

Engine Friction

The total friction of the engine is composed of mechanical, and auxiliary friction. The mechanical friction is the dissipation of energy by relative movements of components in the engine, and the auxiliary friction is the work absorbed by components like pumps, fans, and valve springs etc. The total friction is modeled as a friction torque as a function of mean piston speed C_t and the maximum pressure in the cylinder P_{max} given by

$$Tq_f = aC_m + bP_{max} + c \tag{3.22}$$

where a, b and c are constants fitted to the specific engine.

3.2.2 Intercooler

The intercooler is placed between the compressor and charge air receiver with the purpose of cooling the air before entering the engine. In this model the intercooler is modeled as a heat exchanger where the downstream temperature T_d is determined from the upstream temperature T_u, the upstream water temperature T_w and a heat exchanger effectiveness parameter ϵ:

$$T_d = T_u - \epsilon(T_u - T_w) \tag{3.23}$$

It assumed that the intercooler can be viewed as a flow restriction, hence the mass flow rate and mass flow rate of the burnt product is calculated as in equations (3.12) and (3.14). The energy flow in $\dot{E}_u$ and out $\dot{E}_d$ of the intercooler is then determined as in equation (3.24) where the heat transferred to the water is subtracted from the outgoing energy flow [25].

$$\begin{aligned}
\dot{E}_u &= \dot{m}h(P_u, F_u, T_u) \\
\dot{Q} &= h(P_u, F_u, T_u) - h(P_d, F_d, T_d) \\
\dot{E}_d &= \dot{m}h(P_u, F_u, T_u) - \dot{Q}
\end{aligned} \tag{3.24}$$

3.2.3 Turbocharger

There are several ways to model a turbocharger from mathematical models to computational fluid dynamic (CFD) approaches. The development of a mathematical model would involve many simplifications affecting the accuracy [25], and a full CFD approach will greatly increase the computational complexity. A common approach is the use of look-up tables in the form of turbocharger performance maps which were described in Chapter 2.4.1. At each step in the simulation, two known variables are interpolated to find two unknown variables. This approach is computationally very fast. However, some challenges regarding its accuracy for transient simulations are given by Rakopoulos and Giakoumis [6]. The turbocharger is assumed to behave in a quasi-steady manner, i.e. following steady-state operating conditions from the performance maps to model the transient behavior of the turbocharger. In reality, the behavior of the turbocharger is unsteady, especially in the turbine. This could be an oversimplification, but due to the lack of better alternatives and since the time constants related to the general trends of response improvements are much larger than those of the unsteady effects in the turbine, this assumption should hold. Another limitation of the look-up tables, as will be seen later, is the difficulty in obtaining turbocharger operating conditions for low-load low-speed conditions consequently limiting the scope of the engine model.

An overview of the hybrid turbocharger model is given in Figure 3.10 showing the thermal components (turbine and compressor), and the mechanical parts connected to the turbocharger shaft. Both the turbine and compressor are implemented as R-fields.

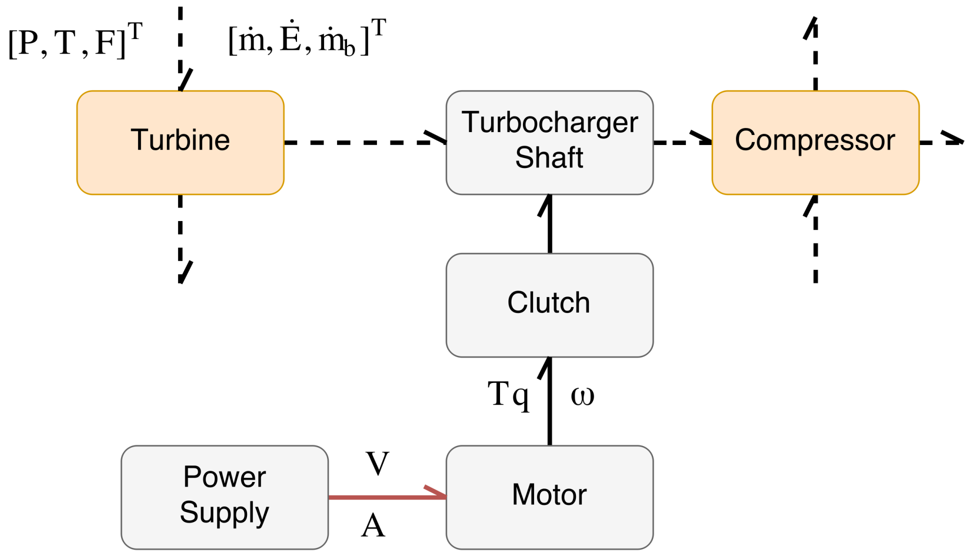

Figure 3.10: Turbocharger model with sub-models

Turbine

The mass flow rate through the turbine is modeled as an isentropic nozzle as given in equation (3.25), where C_t is the turbine flow coefficient given by the turbine map as function of pressure ratio Π_t and the turbine blade-speed ratio $\tilde{c}_{us}$ as defined in equation (2.11).

$$\dot{m}_t = \frac{C_t A_t P_u}{\sqrt{R_u T_u}} \Pi_t^{\frac{1}{\gamma}} k \qquad k = \begin{cases} \left(\frac{2\gamma}{\gamma-1} \left[1 - \Pi_t^{\frac{\gamma-1}{\gamma}} \right] \right)^{\frac{1}{2}}, & \text{if} \quad \Pi_t > \left(\frac{2}{\gamma+1} \right)^{\frac{\gamma}{\gamma-1}} \\ \sqrt{\gamma} \left(\frac{2}{\gamma+1} \right)^{\frac{\gamma+1}{2(\gamma-1)}}, & \text{otherwise} \end{cases} \tag{3.25}$$

$$\begin{aligned} C_t &= MAP_{Ct}(\Pi_t, \tilde{c}_{us}) \\ \eta_t &= MAP_{\eta_t}(\Pi_t, \tilde{c}_{us}) \end{aligned} \tag{3.26}$$

The isentropic efficiency η_t is also given as a function of pressure ratio and turbine-blade speed ratio given in equation (3.26). The mass flow rate of burnt product is given by

$$\dot{m}_b = \dot{m}_t \frac{f_s F_u}{1 + f_s F_u} \tag{3.27}$$

The calculation of change in specific enthalpy is given by (3.28), where $T_{is,d}$ is the isentropic temperature and γ the ratio of specific heats for incoming flow.

$$\begin{aligned} \Delta h_t &= \frac{h_{is,d}(P_d, T_{is,d}, F_d) - h_u(P_u, T_u, F_u)}{\eta_t} \\ T_{is,d} &= T_u \Pi_t^{\frac{\gamma-1}{\gamma}} \end{aligned} \tag{3.28}$$

The energy flows in and out are then given according to

$$\begin{aligned} \dot{E}_u &= \dot{m}_t h_u \\ \dot{E}_d &= \dot{m}_t (h_u + \Delta h_t) \end{aligned} \tag{3.29}$$

The torque produced from the expansion over the turbine Tq_t is given by equation (3.30) where ω_{tc} is the turbochargers rotational speed.

$$Tq_t = \frac{\dot{m}_t \Delta h_t}{\omega_{tc}} \tag{3.30}$$

Compressor

The corrected mass flow $\dot{m}_{c,corr}$ and compressor isentropic efficiency η_c are obtained from the compressor map given the corrected turbocharger rotational speed, calculated according to equation (2.4), and pressure ratio over the compressor. Furthermore, the compressor mass flow $\dot{m}_c$ is found by converting the corrected value back to actual value, and the compressor efficiency is directly obtained from the map given in equation (3.31).

$$\begin{aligned} \dot{m}_c &= \frac{\frac{P_u}{P_{u,ref}}}{\sqrt{\frac{T_u}{T_{u,ref}}}} MAP_{\dot{m}_{c,corr}}(\Pi_c, \omega_{tc,corr}) \\ \eta_c &= MAP(\Pi_c, \omega_{tc,corr}) \end{aligned} \tag{3.31}$$

The mass of burnt product is equated as in equation (3.14), and the change in specific enthalpy as in (3.28) given by

$$\begin{aligned} \Delta h_c &= \frac{h_{is,d}(P_d, T_{is,d}, F_d) - h_u(P_u, T_u, F_u)}{\eta_c} \\ T_{is,d} &= T_u \Pi_c^{\frac{\gamma-1}{\gamma}} \end{aligned} \tag{3.32}$$

The energy flows in and out are then give according to

$$\begin{aligned} \dot{E}_u &= \dot{m}_c h_u \\ \dot{E}_d &= \dot{m}_c (h_u + \Delta h_c) \end{aligned} \tag{3.33}$$

The torque required to compress the air Tq_c is then given by

$$Tq_c = \eta_{v,c} \frac{\dot{m}_t \Delta h_c}{\omega_{tc}} \tag{3.34}$$

where $\eta_{v,c}$ is the volumetric efficiency of the compressor.

Shaft

The mechanical part of the turbocharger consists of a 1-junction with an inertia element representing the turbocharger inertia J_{tc}, and a resistor element representing the friction. The friction was modeled by empirically fitting results from Vanhaelst et al. [30] to a quadratic function as in

(3.35) with the constants $a = 5 \cdot 10^{-3}$, $b = 6 \cdot 10^{-7}$ and $c = -4 \cdot 10^{-12}$, relating friction torque and turbocharger speed.

$$Tq_{tc,fric} = a + b\omega_{tc} + c\omega_{tc}^2 \tag{3.35}$$

The electric motor is in one proposed configuration connected to the turbocharger shaft via a clutch mechanism. The torque transmitted by the clutch Tq_f is modeled as in Pedersen and Engja [23], given by

$$Tq_f = F_n(\mu_s tanh(s\omega) - 0.5(\mu_s - \mu_c)tanh(s(\omega - \frac{6.5}{s})) + tanh(s(\omega + \frac{6.5}{s})) + \mu_v\omega) \tag{3.36}$$

where μ_s, μ_c, and μ_v are the static, coulomb and viscous friction coefficients respectively, s is the slope and F_n is the normal force given by a clutch engagement profile. The implementation of the clutch is done with a resistor element. The values used for the friction coefficients are given in Table 3.5.

Coefficient	**Value**
μ_s	0.2
μ_c	0.3
μ_v	0.3
s	1000

Table 3.5: Friction coefficients for the clutch configuration

3.2.4 Engine Controller

Compared to the basic control structure for a turbocharged diesel engine presented in Chapter 2.5, the model is equipped with neither EGR or a VGT/wastegate. Hence the control system in the model will consist only of the fuel path coupled to the air path through the smoke limiter. The engine speed control is realized by proportional, integral, derivative (PID) controller[3], and a smoke limiter. The inputs to the PID are the desired engine speed ω_{ref} and the measured engine speed ω, where the error is given by $e = \omega_{ref} - \omega$. The measured speed is filtered by a fourth-order Butterworth filter to remove the high-frequency speed changes caused by the torque changes related to the engine cycles of the cylinder. Also, the output of the smoke limiter $uGov_{sl}$ is compared with a saturated signal $uGov_{sat}$ where the smallest of them is sent back into the integral action as an anti-windup term. A block diagram of the control scheme can be seen in Figure 3.11.

---

[3] See Appendix A.1 for more on PID control.

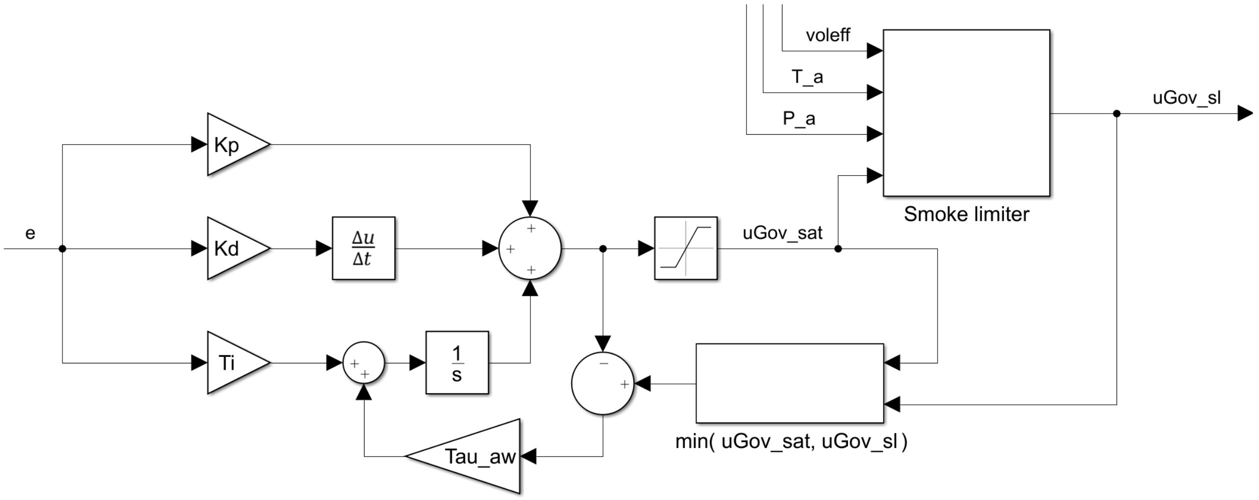

Figure 3.11: Block diagram representation of the engine control unit.

The smoke limiter calculates (or estimates) the mass of air in the cylinder per cycle m_a, as in equation (3.37) based on the charge air pressure and temperature P_a, T_a, the volumetric efficiency η_v, the specific gas constant for dry air R ,and the engine displacement V_d.

$$m_a = \frac{P_a}{RT_a} V_d \eta_v \tag{3.37}$$

Then based on a maximum allowable fuel-air equivalence ratio F_{max}, the ratio of maximum allowable m_f to maximum possible mass of fuel $m_{f,max}$ (given by fuel rail design) for the cycle is calculated. The computation can be expressed as

$$uGov_{sl} = \begin{cases} \frac{m_a F_{max} f_s}{m_{f,max}} \quad , & uGov_{sat} > \frac{m_a F_{max} f_s}{m_{f,max}} \\ uGov_{sat} \quad , & \text{otherwise} \end{cases} \tag{3.38}$$

The final output $uGov_{sl}$ is then a measure of the amount of fuel to be injected used by the combustion model to calculate the Wiebe curves.

3.2.5 Electric motor model

Electrical motors consist of a rotating part (rotor) and a stationary part (stator). In a permanent magnet direct current (PMDC) motor the rotor is a current-carrying coil placed inside a constant magnetic field (stator). The current flowing through the coil, often called armature, will generate its own magnetic field, resulting in a force acting on the rotor. The torque produced by the force can be described by equation (3.39), where $T_{q,em}$ is the torque produced, i_a the armature current, and k_t the torque constant. The torque constant represents the transfer from current to torque and is a function of constructive motor parameters, such as the number of rotors, the number of windings, magnetic field density, and so on.

$$T_{q,em} = k_t i_a \tag{3.39}$$

When a coil is rotated within a magnetic field it will experience an induced voltage, called the electromotive force (EMF). The EMF is given by equation (3.40), where ω represents the rotor's rotational speed, k_e the back-emf constant. For PMDC motors the torque constant is equal to the back-emf constant, $k_t = k_e$.

$$EMF = k_e \omega \tag{3.40}$$

Equations (3.39) and (3.40) form the constitutive law for the gyrator element in the bond graph relating the electrical domain to the mechanical. The series circuit on the electrical side has equal current flow over the components, while the directed sum of voltages represents the voltage drop across each component, i.e. Kirchoff's voltage law.

An equivalent circuit and a corresponding bond graph of a DC motor can be seen in Figure 3.12, where L_a, and r_a denote the armature inductance and resistance respectively.

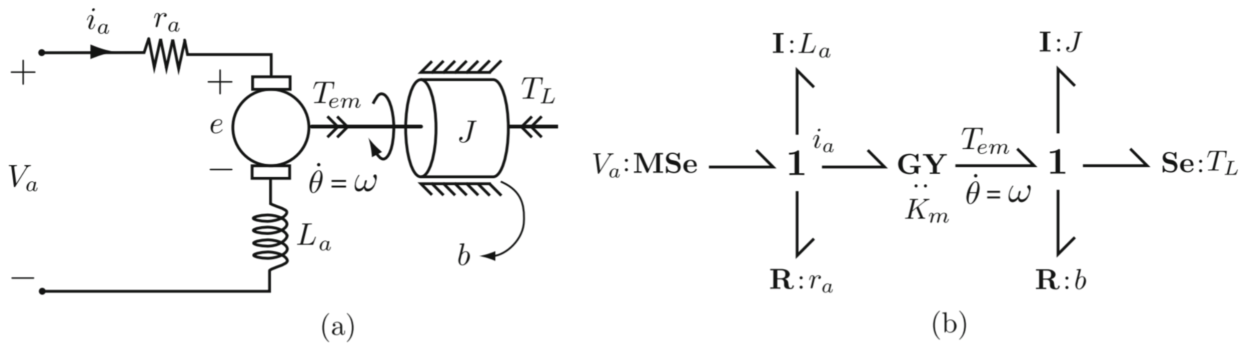
i_a
r_a
+
+
e
−
T_{em}
T_L
J
V_a
$\dot{\theta}=\omega$
L_a
b
−
(a)
$\mathbf{I}:L_a$
$\mathbf{I}:J$
$V_a:\mathbf{MSe}$
$\mathbf{1}$
i_a
$\mathbf{GY}$
K_m
T_{em}
$\dot{\theta}=\omega$
$\mathbf{1}$
$\mathbf{Se}:T_L$
$\mathbf{R}:r_a$
$\mathbf{R}:b$
(b)

Figure 3.12: Permanent magnet DC-motor represented as; a) equivalent circuit b) bond graph. Retrieved from Junco and Donaire [31]

One of the design proposals includes a mechanism to break the armature circuit. The circuit breaker is included in the model as a transformer element between the 1-junction and gyrator. To break the circuit, the transformer modulus is set to zero otherwise it is set to one.

The series DC motor was also modeled and considered due to its ability to produce very high torques at low speeds. Its equations are similar to those of the PMDC described above, the difference being the magnetic field is self-exited from the field windings opposed to the constant field from the permanent magnet. The flux linkage ψ_f induced by the field windings is a function of field current i_f, and field inductance L_f. In a series connection the field and armature currents are equal $i_f = i_a$. Neglecting magnetic hysteresis the torque and EMF of a series DC motor is given in equation (3.41)[31], where K represents constructive motor parameters. The equivalent circuit and bond graph of the series DC motor is depicted in Figure 3.13

$$\begin{aligned}
T_{q,em} &= K'\psi_f i_a \\
&= K' L_f i_f i_a \\
&= K i_a^2 \\
EMF &= K'\psi_f \omega \\
&= K' L_f i_f \omega \\
&= K\omega i_a
\end{aligned} \tag{3.41}$$

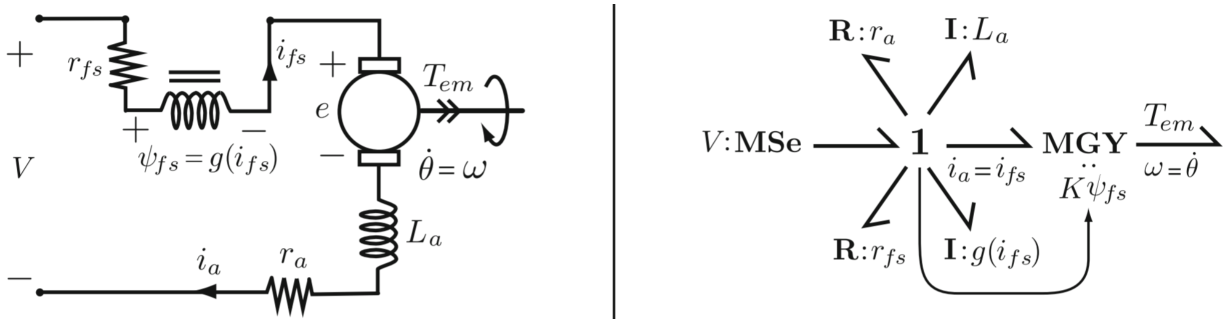
+
r_{fs}
i_{fs}
+
T_{em}
e
+
−
$\psi_{fs} = g(i_{fs})$
−
V
$\dot{\theta} = \omega$
L_a
i_a
r_a
−
$\mathbf{R}:r_a$
$\mathbf{I}:L_a$
V:MSe
1
MGY
T_{em}
$i_a = i_{fs}$
$K\psi_{fs}$
$\omega = \dot{\theta}$
$\mathbf{R}:r_{fs}$
$\mathbf{I}:g(i_{fs})$

Figure 3.13: Series DC-motor represented as equivalent circuit (left), and bond graph (right). Retrieved from Junco and Donaire [31]

Motor Controller

The speed control of the motors was realized with a cascaded PI controller. The inner loop controls the armature current and the outer loop the speed. A block diagram representation of the control system is given in Figure 3.14. The blocks PI speed and PI current represent the proportional and integral action of each of the controllers. The torque and voltage limiters keep the motor within its constraints, and the final output is the voltage supplied to the motor.

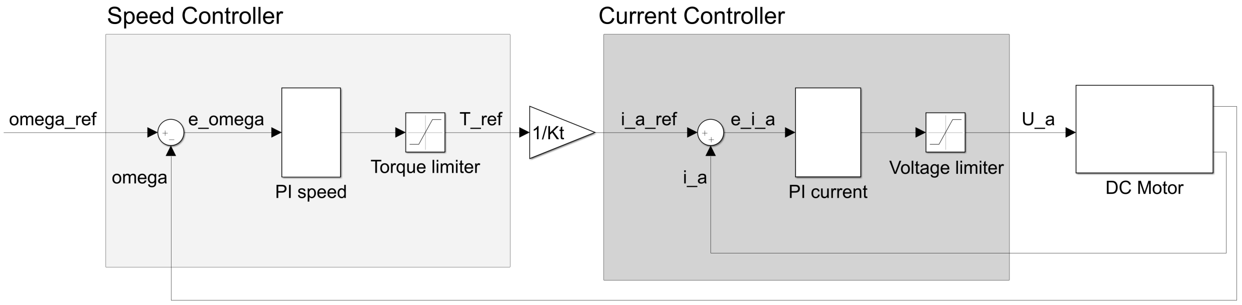
Speed Controller
Current Controller
omega_ref
e_omega
T_ref
1/Kt
i_a_ref
e_i_a
U_a
omega
PI speed
Torque limiter
i_a
PI current
Voltage limiter
DC Motor

Figure 3.14: Block diagram representation of the cascaded speed controller for the motors

Chapter 4

Model Validation

In this chapter, the model is validated against a similar engine in the laboratory. Validating the model with real measurements from a controlled laboratory test gives an indication of the accuracy of the model. By comparing the model and experimental results, it can be determined if the model provides adequate fidelity to describe the physical process of interest.

In Chapter 2.1.2 some of the challenges of transient testing was mentioned, consequently making the process of validating and tuning the model to fit experimental results exactly, difficult and time-consuming. To add to the complexity, several engine parameters are not given by the engine manufacturer and have to be approximated, including the control strategy, which significantly influences the transient behavior of the system. With these challenges in mind, the purpose of the validation here is to confirm that the time constants related to turbo-lag phenomenon are similar.

4.1 Experimental Model Validation

The model is based on a slightly different engine than the one in the lab. Basic engine specifications for the model and the lab engine are given in Table 4.1. From the table, we see that the model has somewhat higher power and torque ratings, a slightly larger displacement and an additional cylinder.

Engine	**Model**	**Experiment**
Name	Scania DC1102	Scania DI09 072M
Principle of Operation	4-stroke	4-stroke
Cylinder alignment	Inline-6	Inline-5
Displacement [l]	10.64	9.3
Bore x stroke [mm]	127 x 140	130 x 140
Maximum power [kW]	280	221
Maximum torque [Nm]	1750	1623
Optimum SFC [g/kWh]	191	191

Table 4.1: Model and laboratory engine specifications

Adapting the model to the lab engine could be done by removing a cylinder component. This would require a reconfiguration of cam angle related calculations in the valves and combustion components. Furthermore, other engine parameters would have to be obtained from either data sheets or approximated through steady-state testing. Given the time frame and scope of this thesis, a reconfiguration with full steady-state validation was not done. Naturally, these differences will contribute to some discrepancies between the model and experimentally obtained data.

4.1.1 Experimental setup

Several tests were performed to validate that the time constants involved in the transient events were within the same magnitude. Specifically, three transient tests were performed in the lab with initial and final values given in Table 4.2.

	Speed [rpm]		**Load** [Nm]	
	Initial	Final	Initial	Final
Run 1	850	1100	1030	1125
Run 2	1100	1650	1125	1250
Run 3	1600	2100	867	916

Table 4.2: Initial and final values of engine speed and loads for experimental validation of three transient runs

The load setting for the dynamometer was set to a constant value, while the load generated had a quadratic torque-speed relation of the type seen in equation (4.1), where Tq_{load} is the generated torque, ω the engine speed, and C_1, C_2 constants. The load was implemented in the model by fitting the experimental data from each run to the quadratic relation below.

$$Tq_{load} = C_1 + C_2\omega^2 \tag{4.1}$$

4.1.2 Analysis of Results

In Figures 4.1 to 4.3 we see some of the variables[1] related to the turbocharger dynamics for the three transient tests. For engine speed response, the simulation is in good agreement with experimental data for run 1 but is too fast in run 2 and 3. The same trends can also be seen in the response of turbocharger speed and charge air manifold pressure.

A stricter smoke limiter was imposed in an attempt to better fit the experimental results. The value of F_{max} in equation (3.38) was changed from 0.9 to 0.85 and the volumetric efficiency η_v used in equation (3.37) was modified from 1 to its calculated value which is around 0.9. Both these reductions contribute to a 15 % total reduction in maximum allowable fuel over the whole operating range.

In terms of transient performance, the modified smoke limiter does not affect the simulation for run 3 since this run is at speed- and load conditions where there smoke limiter is not active. In run 2 the modified smoke limiter slowed down the response by almost a second, which is closer to the response of the lab engine. Whereas in run 1 the stricter smoke limiter caused the engine to stall for the same initial operating conditions, forcing a comparison at a higher engine speed. At a slightly higher engine speed, the response time was similar to that of the original smoke limiter and experimental result.

---

[1] Simulated engine variables are filtered to remove the oscillatory dynamics associated with the engine cycles to enhance the presentation in plots.

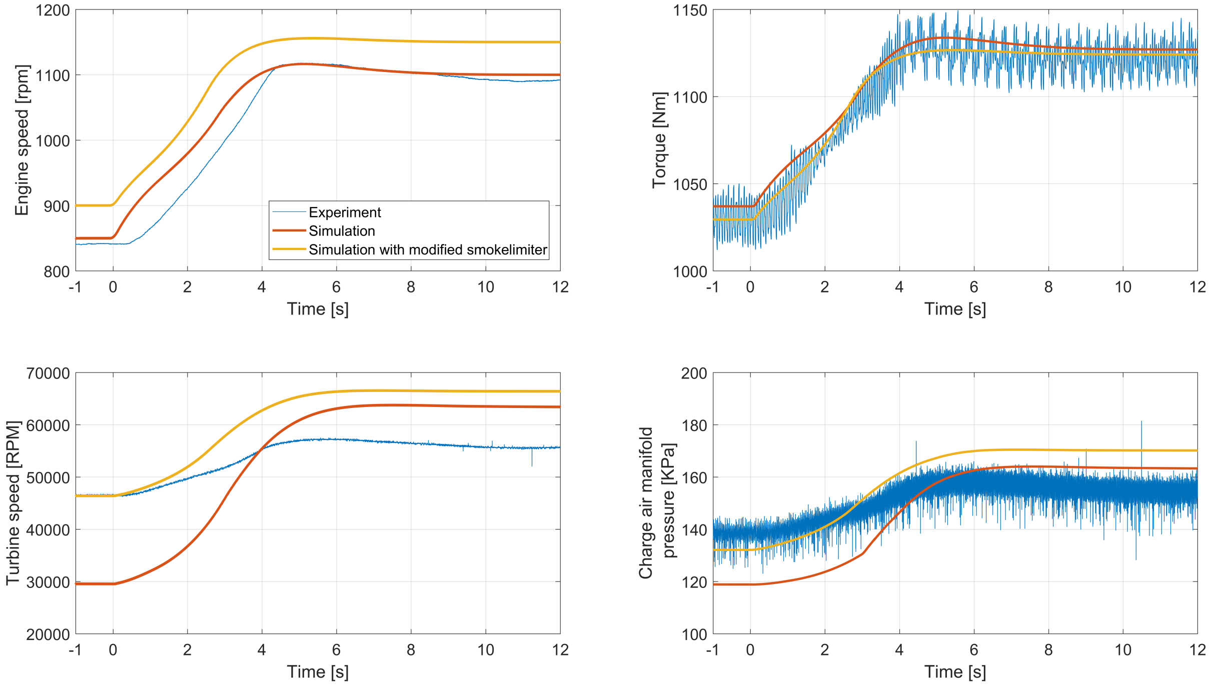

Figure 4.1: Engine speed, load, turbocharger speed, and manifold pressure for run 1

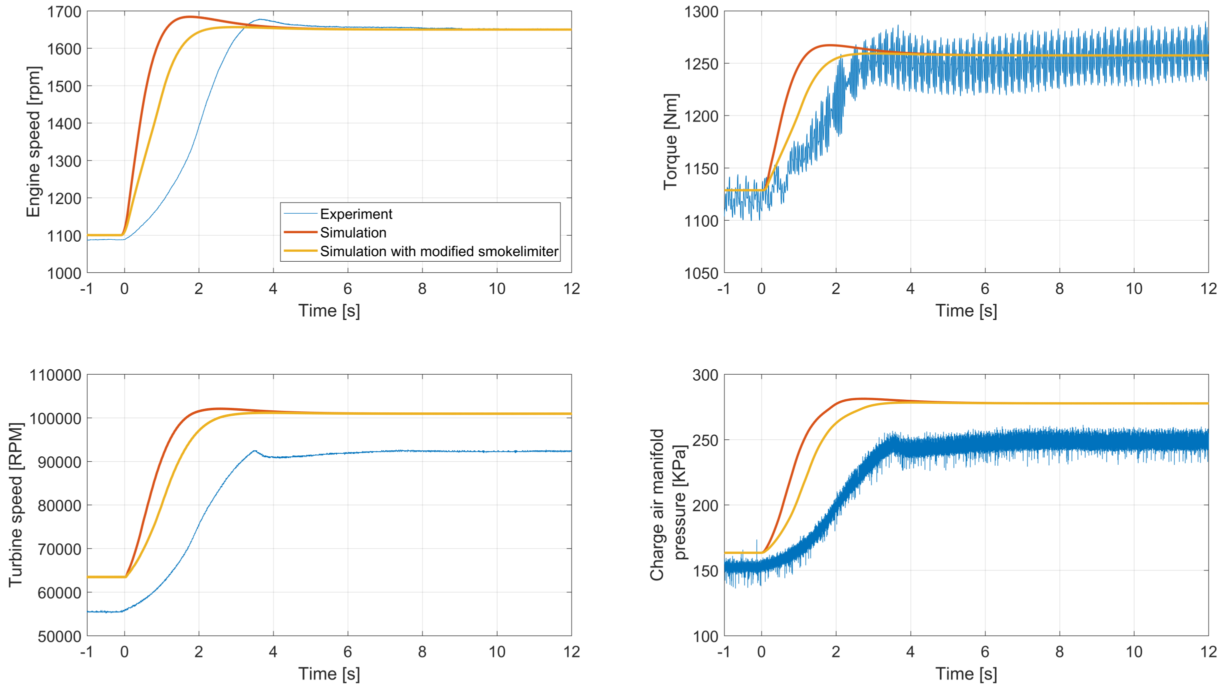

Figure 4.2: Engine speed, load, turbocharger speed, and manifold pressure for run 2

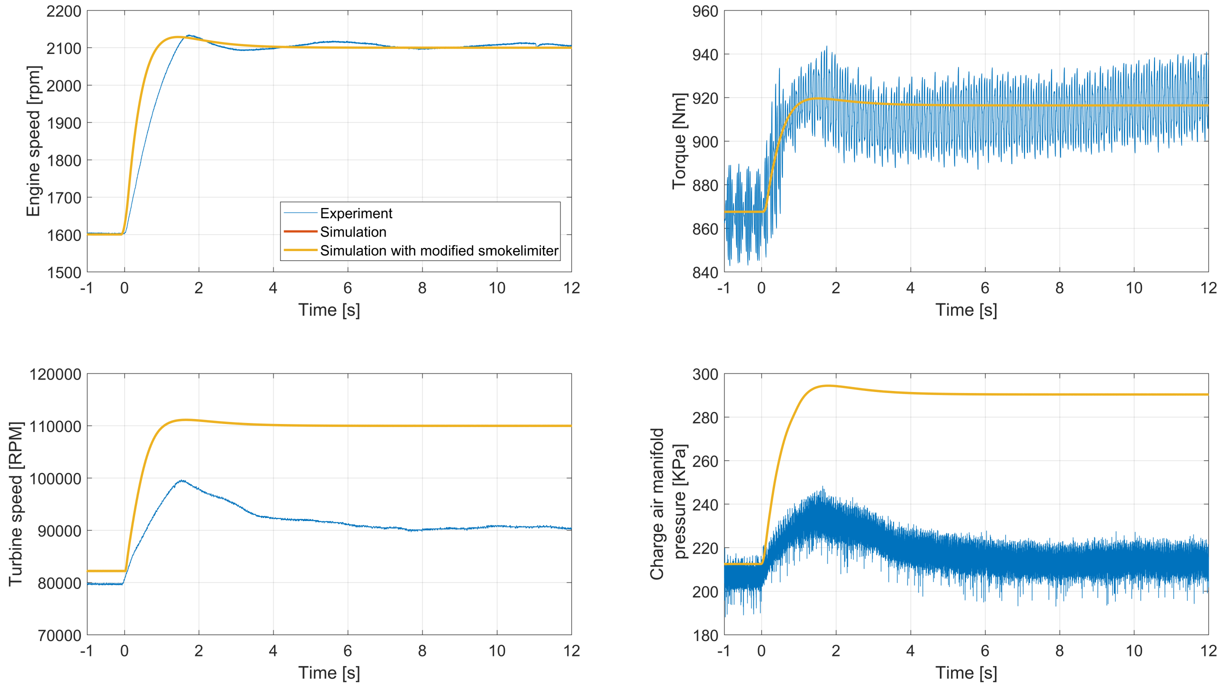

Figure 4.3: Engine speed, load, turbocharger speed, and manifold pressure for run 3

A comparison of operating points before and after the transients provides an indication of how the model compares in steady-state conditions. A summary of how the simulation compares for run 2 and 3 in steady state conditions can be seen in Table 4.3, where the general trend shows larger values for the mode. A comparison of steady-state values is not done for run 1 due to the different initial and final operating conditions.

	Turbocharger speed		**Manifold pressure**	
	Initial	Final	Initial	Final
Run 2	+14 %	+9 %	+8 %	+9 %
Run 3	+3 %	+18 %	+5 %	+25 %

Table 4.3: Steady-state differences of the simulation compared to experiment.

A comparison of the two smoke limiter settings on maximum steady-state torque can be seen in Figure 4.4. The stricter settings reduce maximum torque over the whole operating range. Compared to Table 4.1, and Figure 2.1 the original smoke limiter compares better than the modified one. However, the opposite is the case during transients. The modified smoke limiter was still selected as it has more realistic values, i.e., $F_{max} = 0.85$ and $\eta_v = 0.9$.

The shaded area in Figure 4.4 indicates regions of operation where the compressor operates at lower pressure ratios and mass flows than what is defined by the map. When the operating point wanders to far from the defined map, the mass flow through the compressor is set zero causing the simulation to crash, effectively limiting the scope of the model. A similar situation also occurs at high speeds (due to the model lacking boost control), where pressure ratios and mass flows are no longer defined by the map. This is what limits the maximum steady-state torque for both the modified and original smoke limiter from 2000-2100 rpm seen in figure 4.4.

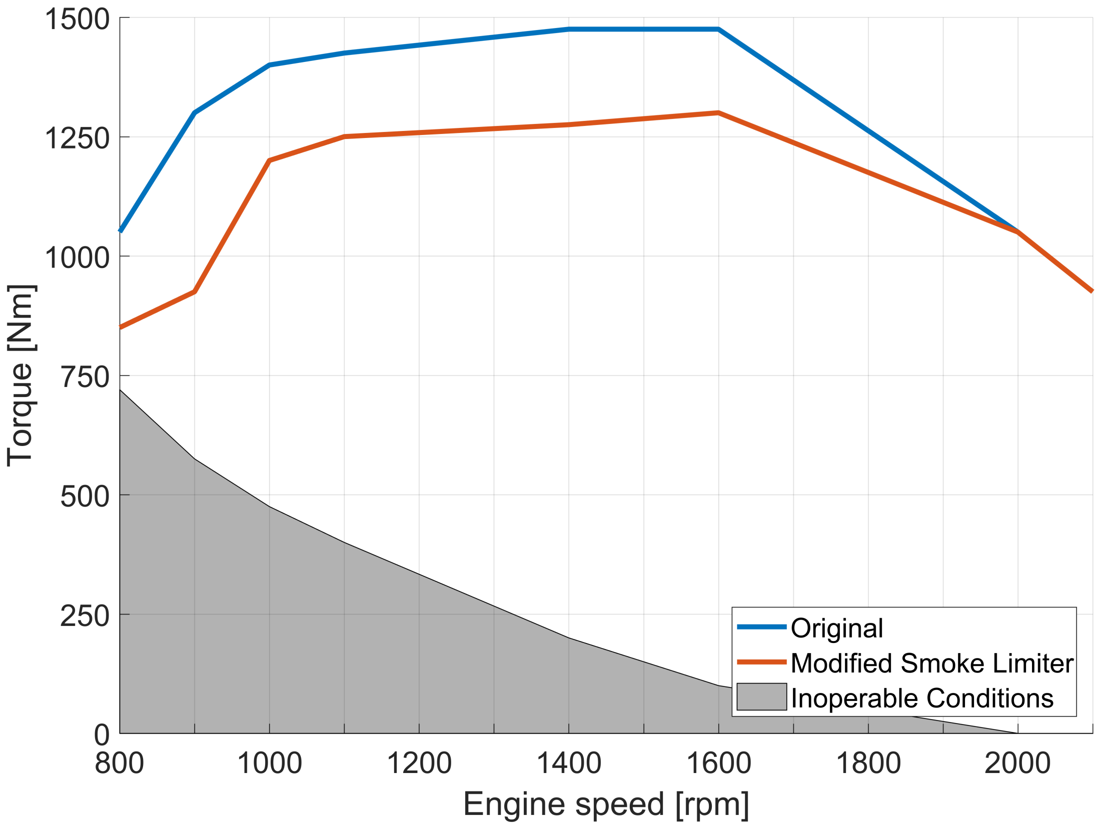

Figure 4.4: Effect of stricter smoke limiter on maximum steady-state torque, and operating conditions outside the scope of the model

Some of the differences seen between the engine and model are naturally a result of slightly different engine parameters. It is also likely that much of the discrepancies seen in transient response can be attributed to the differences in the control strategy. In the model there is no control path to regulate the boost pressure and turbocharger speed, whereas in the real engine a mechanism to avoid exceeding the turbocharger limitations is likely implemented, actuated by reducing fueling. Comparing the charge air pressures and turbocharger speeds for the three runs, it seems as if run 1 operates well below any maximum boost pressure or turbocharger speed limit. In runs 2 and 3 the possible effects of boost control could be explained by the sharp decreases in charge air pressure and turbocharger speeds. This could also be a contributing factor for the large deviations in steady-state values after the transient.

To summarize, the simulated time constants are similar to the experimental results for the low engine speed case, and around 50 % faster for the higher engine speeds. The differences can be attributed to the differences between the engine and model parameters, as well as the differences in control strategy between the two. Despite the differences, it is assumed that general trends in response improvements seen in simulations for transients similar to run 1 will apply to the real engine. However, the specific parameters outlined in the parametric study, and consequently response improvements must be seen in context of the differences shown here.

Chapter 5

Simulation and Results

In this chapter response improvements by use of an electronically assisted turbocharger (EATC) is determined in simulations. First, in Section 5.1 simulation cases used to evaluate the response improvements are selected. Next, in Section 5.2 a parametric analysis is performed on the selected cases, establishing response improvements for various degrees of electrical assistance. Finally in Section 5.3 a permanent magnet DC (PMDC) and a series DC motor is proposed attempting to fulfill the requirements outlined by the parametric study. The PMDC motor is also simulated together with the engine for several configurations of how the EATC could be implemented.

5.1 Selection of Simulation Cases

Several load acceptance tests were performed to learn which transients are most affected by turbo-lag, and consequently find suitable transients to test the EATC for. Load increase transients were performed for low, medium and large steps applied linearly over a 1 second period at three different engine speeds. In Table 5.1 the selected initial and final step values are shown in percentage of the maximum steady-state load for each engine speed. It can be noted that the step magnitudes are smaller for the lower engine speeds due to restrictions imposed by the compressor map as seen in Figure 4.4.

	Initial and final load in % of full load		
Engine speed	Low-Medium	Medium-High	Low-High
1000 rpm	40-60 %	50-70 %	40-70 %
1400 rpm	20-50 %	50-75 %	20-75 %
2000 rpm	0-50 %	50-95 %	0-95 %

Table 5.1: Load increase steps given in initial and final load in % of maximum load at given engine speed.

The general trends of turbo-lag are evident from the engine speed development for the different load increase tests shown in Figure 5.1. The low-medium and medium-high load cases show fairly quick responses for all engine speeds, and little difference between them is seen. In the 2000 rpm case the rise time[1] is unaffected by the magnitude of the step, while the speed drop increases with increasing step size. In the 1400 rpm and 1000 rpm cases the larger steps cause a significant delay in rise time. The delay in rise time is seemingly more severe for the 1400 rpm case, but from Table 5.1 we note that the low-high step is much larger in this case than for the 1000 rpm case. If it were possible to simulate a similar step for the 1000 rpm case the delay would be even bigger, if not leading to engine stall.

---

[1] The time to reach the reference engine speed after the load is applied is referred to as rise time.

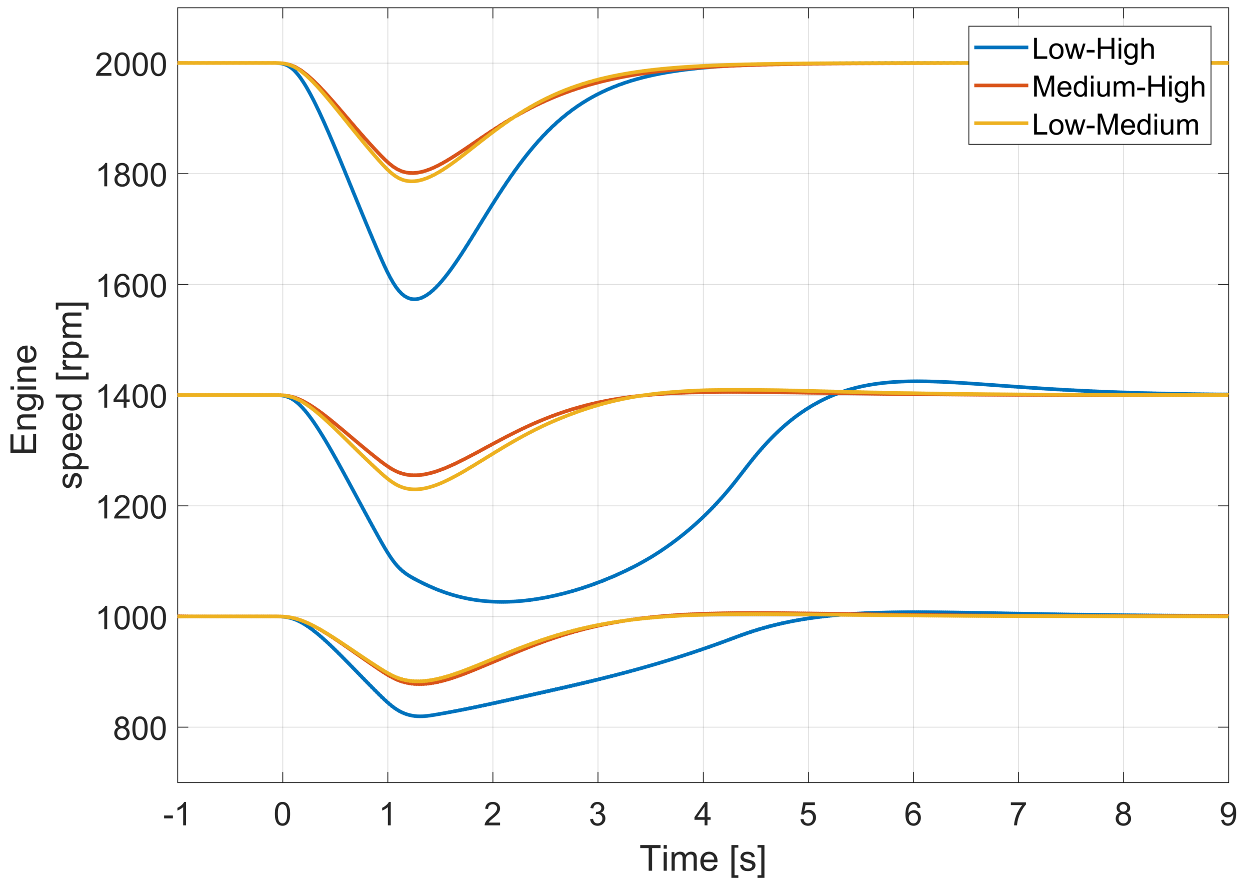

Figure 5.1: Engine speed development for load acceptance transients given in Table 5.1.

A comparison of torque, turbocharger speed, fuel factor F and mass flow of fuel responses for the 1000 rpm and 2000 rpm load increase tests are given in Figure 5.2. The same plot for the 1400 rpm case is given in Appendix A.2. The fuel limiting effects are visible for the low-high load increase in the 1000 rpm case. The maximum fuel factor is reached during the step, consequently followed by fuel limiting and a slow turbocharger speed response. In the 2000 rpm case, there is sufficient air-supply to increase fueling during the transient with little signs of significant turbo-lag.

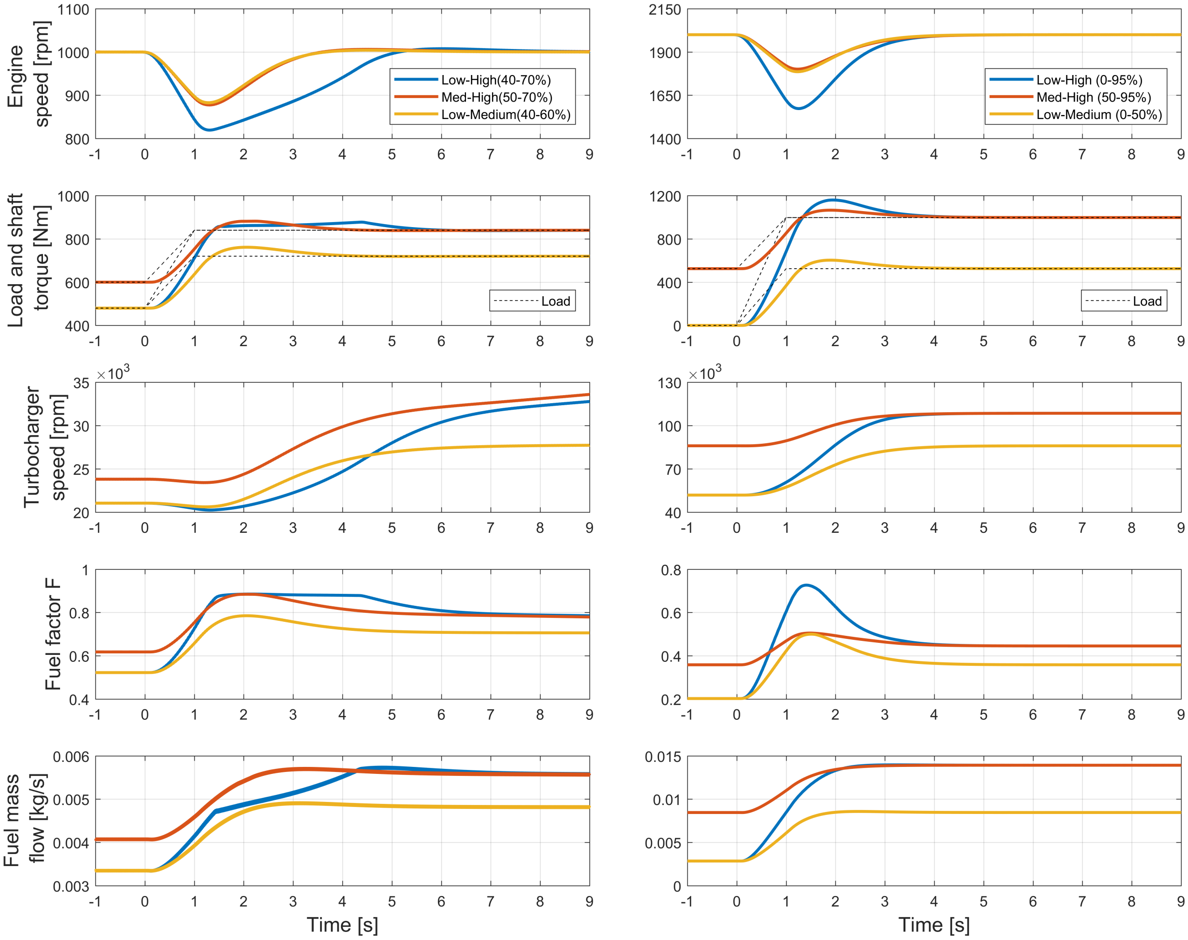

Figure 5.2: Enigne speed, torque, turbocharger speed, fuel factor F and mass flow of fuel responses for the 1000 rpm (left) and 2000 rpm (right) load acceptance tests.

Hence, turbo-lag is more severe for large steps starting at low load and speed conditions, and consequently low turbocharger speeds and boost pressures. The same trend is also seen in speed increase events with large enough steps, where turbo-lag is harsher the lower the initial loads and speeds.

From these findings, while keeping in mind that the time constants for the model were more accurate for the low-speed transients, a speed increase transient and load increase transient with fuel limiting effects depicted in Figure 5.3, was selected for the parametric analysis on the EATC. In the speed increase case the load is applied as a function of engine speed as in (4.1), with initial and final loads of 70 % and 80 % of full load respectively. The load increase transient is the same as the 1000 rpm case tested above. Some room was left on either side of the indicated speed increase transient arrow to allow parametric sweeps without exceeding the limitations of the compressor map.

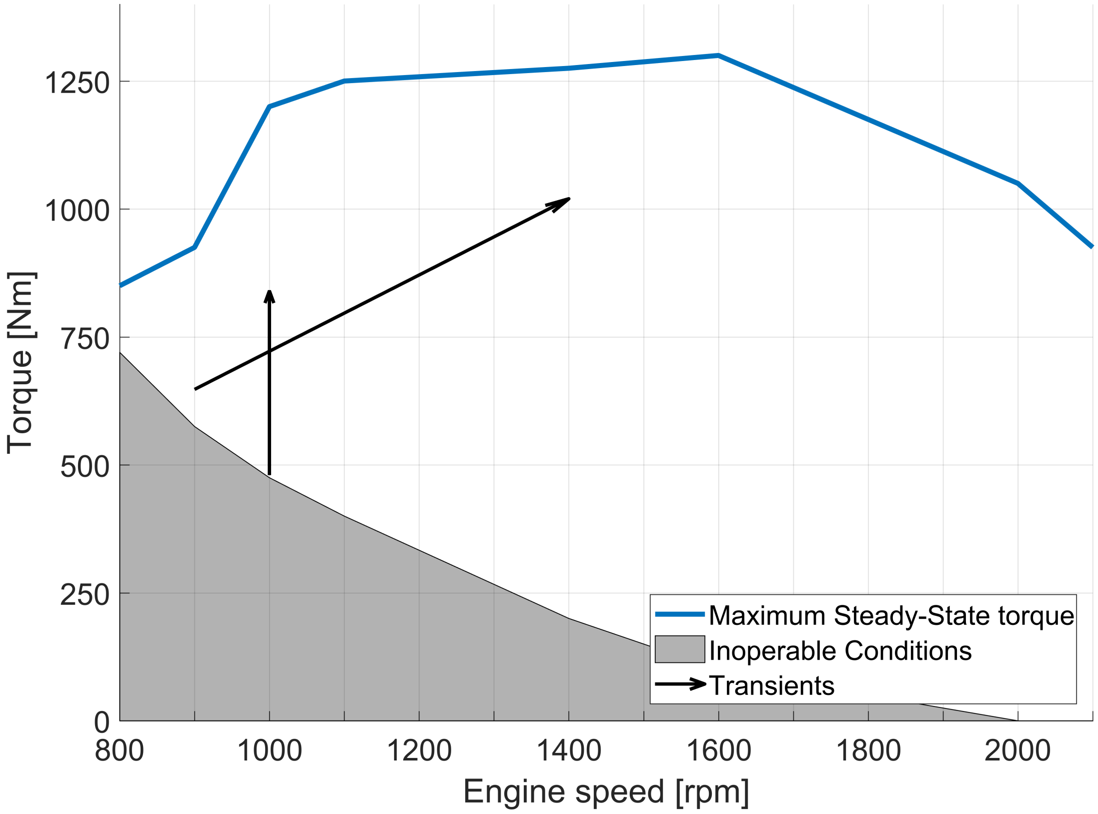

Figure 5.3: Load and speed increase transients selected for the parametric analysis

5.2 Parametric Study of Response Improvements

A parametric study is useful to determine how individual parameters influence a system. This can be done by varying individual parameters and observe how they affect a defined performance index.

5.2.1 Performance Criteria

The overall trends of turbo-lag are well captured by the response of the engine speed, hence to evaluate changes in transient response a performance index based on engine speed was selected. For the speed increase event, performance was measured based on the time to reach 90 % of the final engine speed (τ_{90}). This was selected to avoid including too much of the dynamics associated with the derivative effects from the speed controller as the engine speed gets close to its reference speed. In Figure 5.4 we see the definition of τ_{90}, together with engine speed, reference speed and 90 % of the step size.

For the load increase transient, performance was measured in terms of rise time τ_{rt}, defined as the time to reach reference engine speed after the load is applied. To avoid derivative effects the time was measured from 950 to 950 rpm as seen in Figure 5.5.

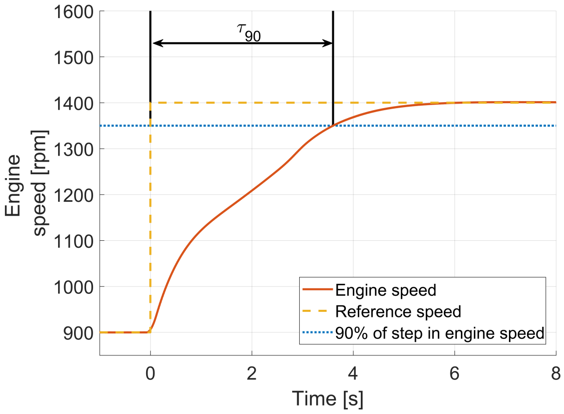

Figure 5.4: Definition of the performance index τ_{90}

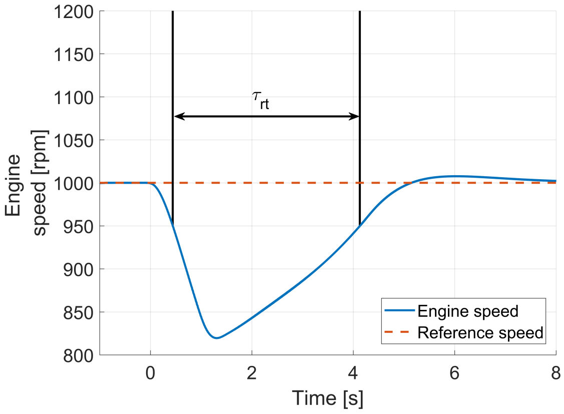

Figure 5.5: Definition of the performance index τ_{rt}

5.2.2 Motor Torque and Inertia

From the compressor map in Figure 2.10 we see that by increasing the turbochargers rotational speed the pressure ratio and/or mass flow rate increases, in turn reducing fuel limiting action, ultimately improving the response. Hence, the EATC must somehow accelerate faster than the conventional turbocharger. The angular acceleration $\dot{\omega}$ is related to rotational inertia J and torque Tq as in equation (5.1).

$$\dot{\omega} = \frac{Tq}{J} \tag{5.1}$$

Requiring a faster angular acceleration from the EATC we get

$$\begin{gathered}\dot{\omega}_{eatc} > \dot{\omega}_{tc} \\ \frac{(Tq_t - Tq_c - Tq_f) + Tq_m}{J_{tc} + J_m} > \frac{(Tq_t - Tq_c - Tq_f)}{J_{tc}}\end{gathered} \tag{5.2}$$

where subscripts tc, t, c, f and m denote turbocharger, turbine, compressor, friction and motor respectively. By solving equation (5.2) for motor torque Tq_m and simulating the selected transient for various motor inertias, an initial estimate for the minimum motor torque as a function of motor inertia J_m is seen in Figure 5.6.

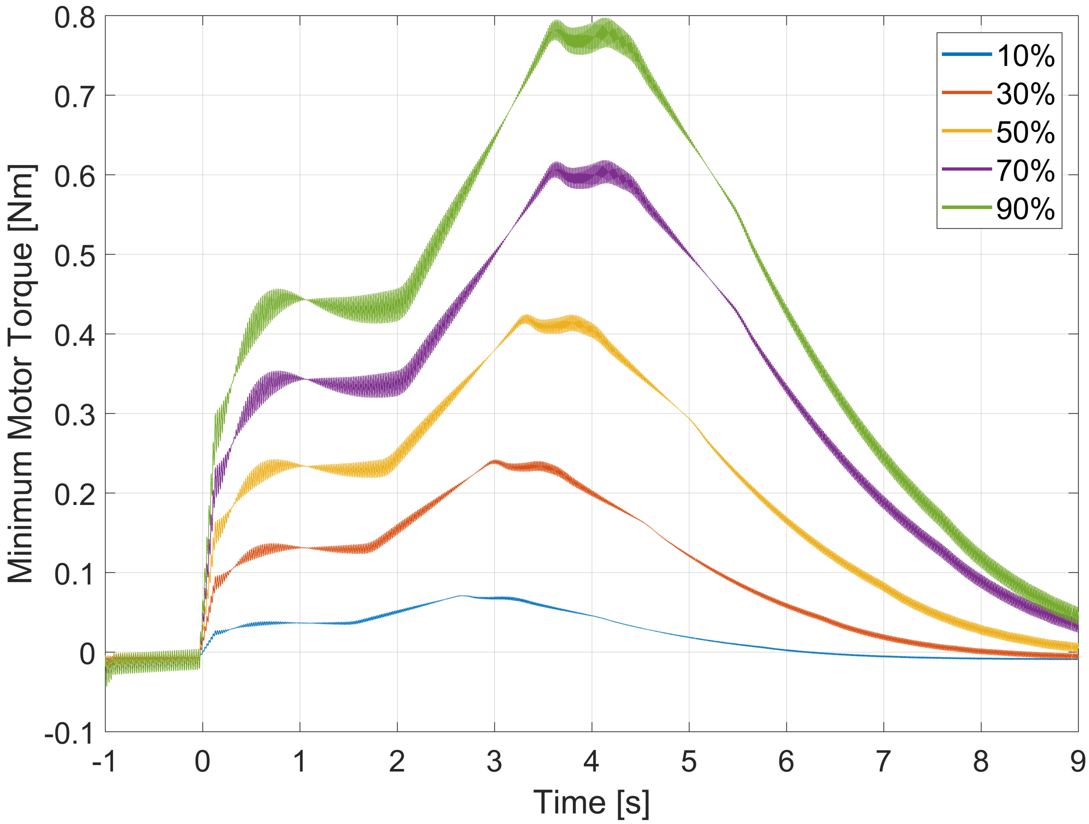

Figure 5.6: Minimum motor torque Tq_m for equation (5.2) to be valid. The motor inertias J_m are labeled as a percentage of the turbocharger inertia J_{tc}.

From the obtained results we can conclude:

- The minimum torque required is larger the larger the motor inertia

- The electric motor should produce at least 0.3 Nm of torque for successful acceleration for the first part of the transient with a motor inertia up to 50 % of the turbochargers inertia.
- The torque requirements for successful acceleration are lower for the first part of the transient.

To further investigate how the turbocharger moment of inertia impacts the transient performance, the turbocharger inertia was varied linearly from half to twice the original moment of inertia as seen in Figure 5.7. A linear increase in response time τ_{90} can be expected for an increased turbocharger moment of inertia. It is also seen that a reduced turbocharger moment of inertia improves response times. The engine speed, turbocharger speed and boost pressure development for three of the simulations can be seen in Figure 5.8. The same trend in response, as for the engine speed can also be seen in turbocharger speed and boost pressure.

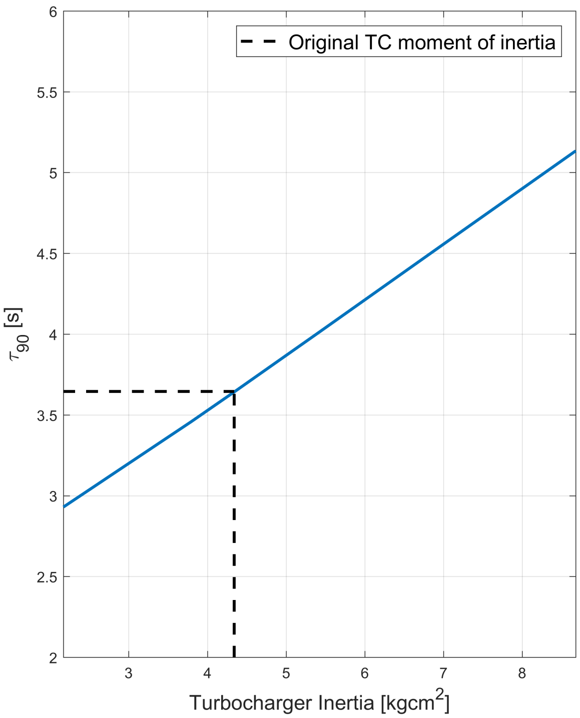

Figure 5.7: Response time τ_{90} with varying turbocharger inertia

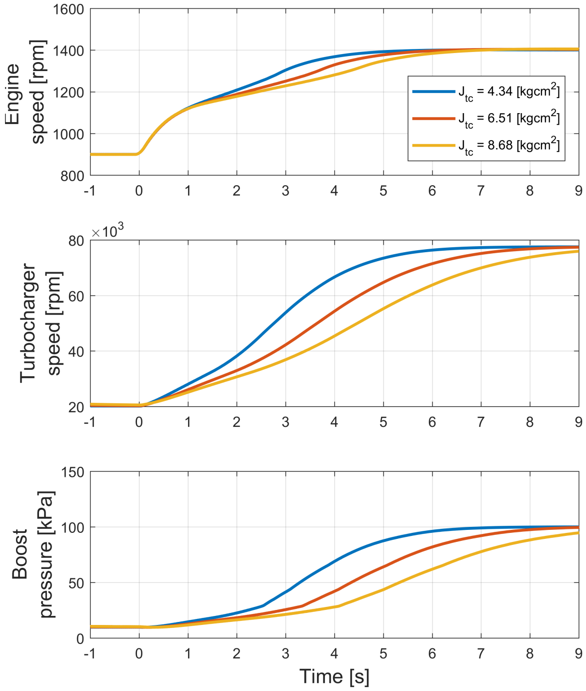

Figure 5.8: Engine speed, turbocharger speed and boost pressure responses for increasing turbocharger inertias

To summarize, the net moment of inertia on the turbocharger shaft should be as small as possible. Also, less torque is required for the initial part of the transient for the EATC to accelerate faster than the conventional turbocharger.

5.2.3 Ideal Motor

To establish how the magnitude and duration of assisted torque affect the engine response a factorial experiment was set up with an ideal motor for the speed increase event. The ideal motor was modeled as a source of torque Tq_{im} producing the requested value over the specified duration. Moreover, the applied torque was provided at the start of the transient with no delay. It was assumed that the ideal motor had no moment of inertia to isolate the impacts of torque and duration. The torque was varied linearly between 0 and 2 Nm, and the duration between 0 and 3 seconds. In Figure 5.9 we see that an assisted torque in the range of 0.5-1 Nm over a duration in the range of 1-1.5 seconds corresponding to 3.5-8.8 kW of maximum power gives between 20-30 % reduction in τ_{90}. Further increases in either parameter see diminishing returns in terms of response improvements.

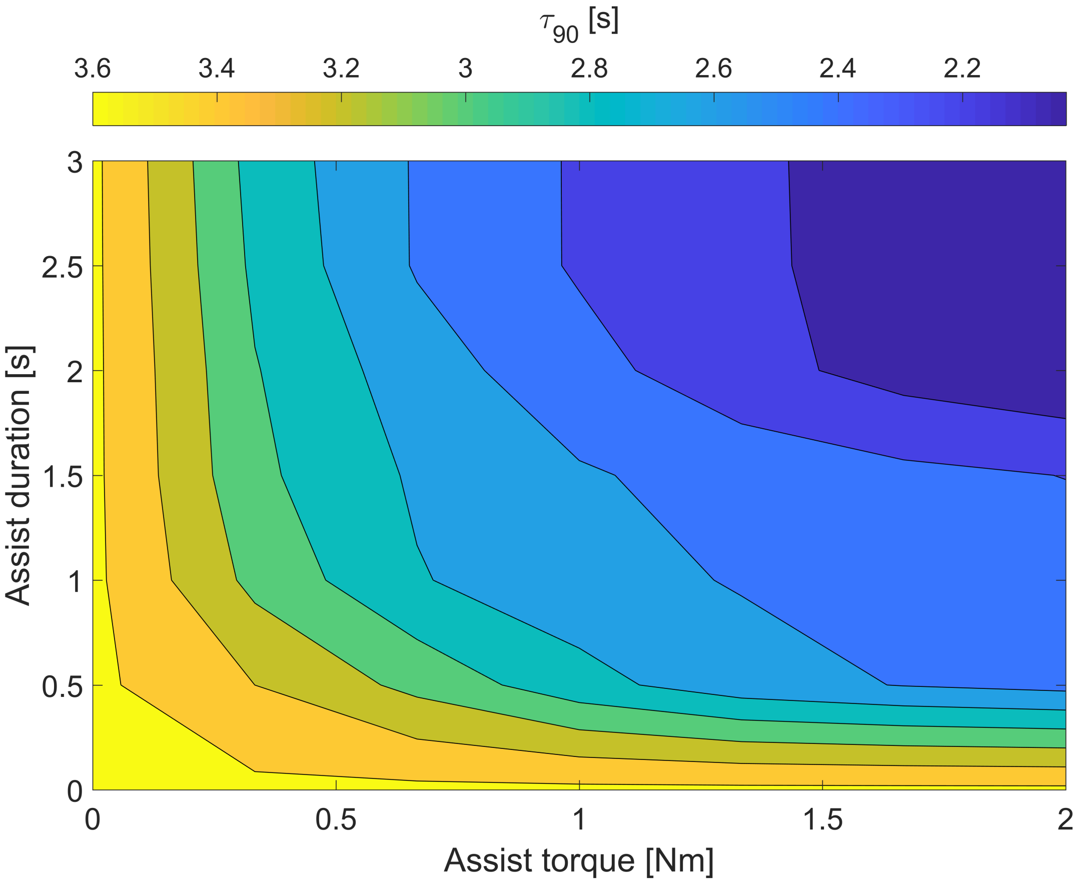

Figure 5.9: τ_{90} response times with ideal motor assistance for varying torques and durations

In figure 5.10 several variables related to the engine can be seen for the ideal motor producing 0, 0.5 and 1 Nm over 1.5 seconds for the speed increase event. Response improvements are seen in engine speed, torque, and turbocharger speed. From the fuel factor and mass flow of fuel, it can be seen that fuel-limiting effects are reduced. With assistance, both the isentropic efficiency of the turbine and compressor are improved throughout the transient. The compressor efficiency improvements are also visible in the compressor map for the three cases seen in Figure 5.11. The assisted transients move the compressor operating points closer to the center of the compressor map where efficiency is higher. The operating points are also far from the boundaries of the compressor map.

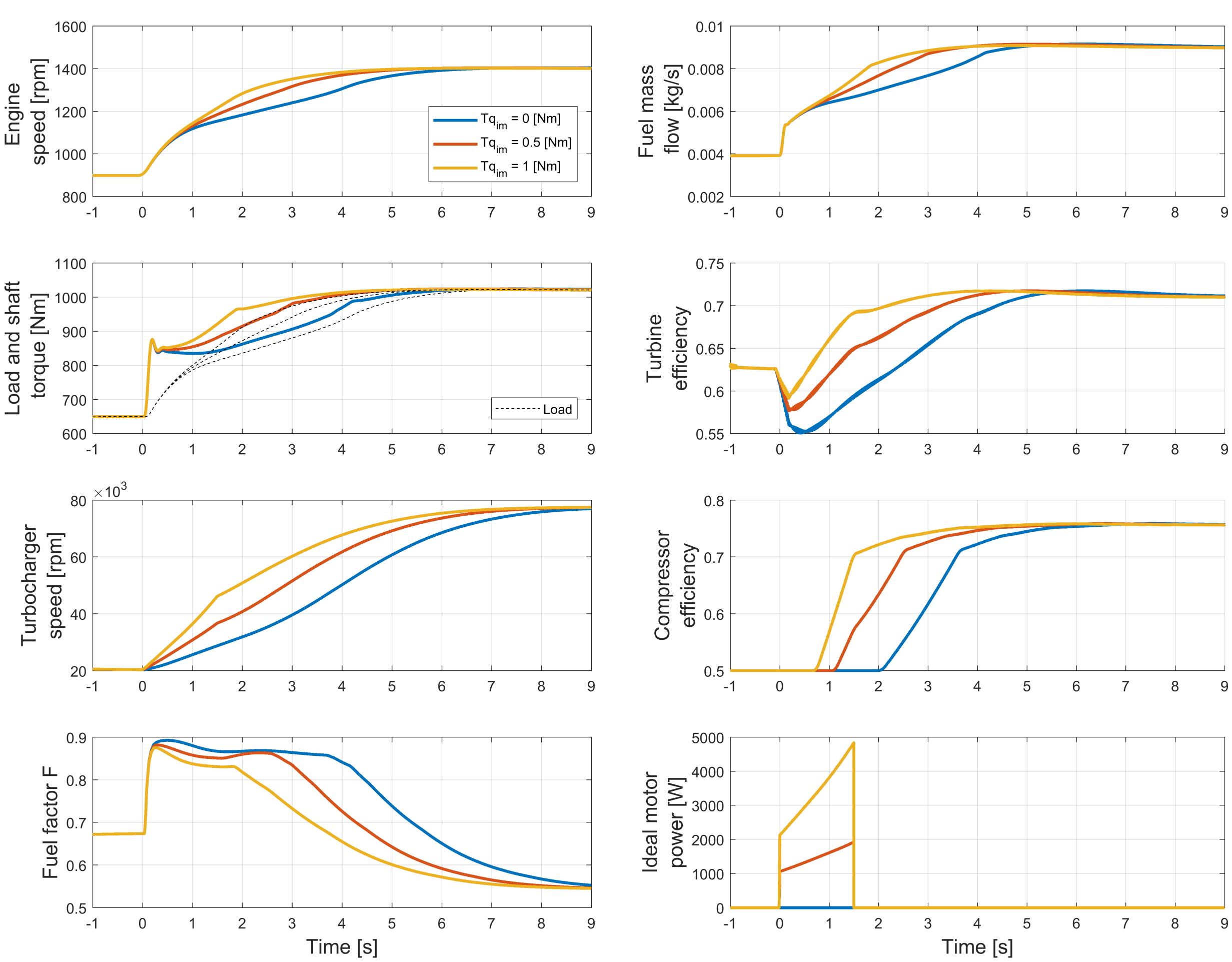

Figure 5.10: Effects on engine speed, torque, turbocharger speed, fuel factor F, mass flow of fuel, turbine isentropic efficiency, compressor isentropic efficiency, and power with an ideal motor assistance of 0, 0.5, and 1Nm over 1.5 seconds

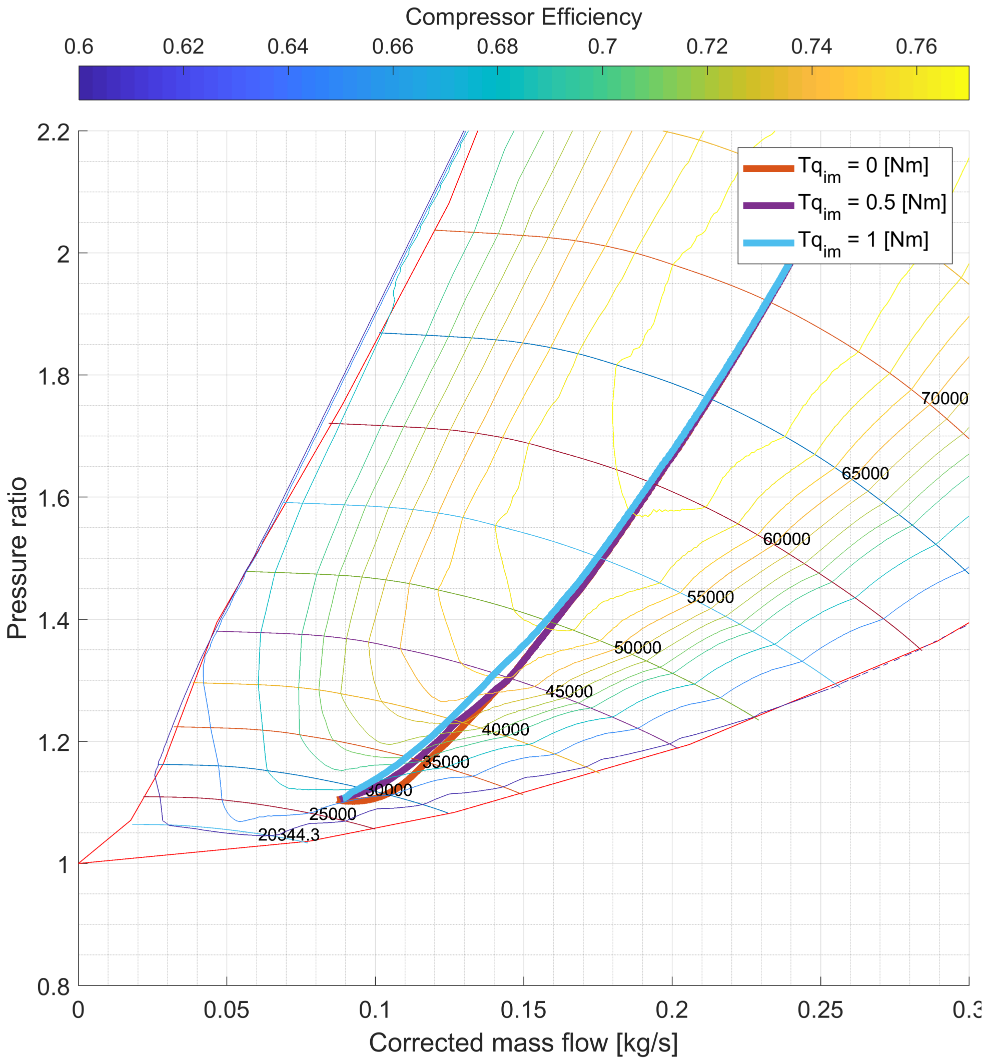

Figure 5.11: Operating points on compressor map plotted for three degrees of ideal motor assistance during a speed increase event

The power of the motor is given by the product of torque and rotational speed, hence increasing degrees of assistance see increasing the power requirements as a result of faster rotational speeds, which can be seen in Figure 5.10. This is further exemplified in Figure 5.12 where it can be seen that an assistance of 0.6 Nm over a 1-second duration requires a maximum of 2.5 kW of power, whereas an assistance of 1.5 Nm over a 2-second duration requires a maximum power of 12.5 kW.

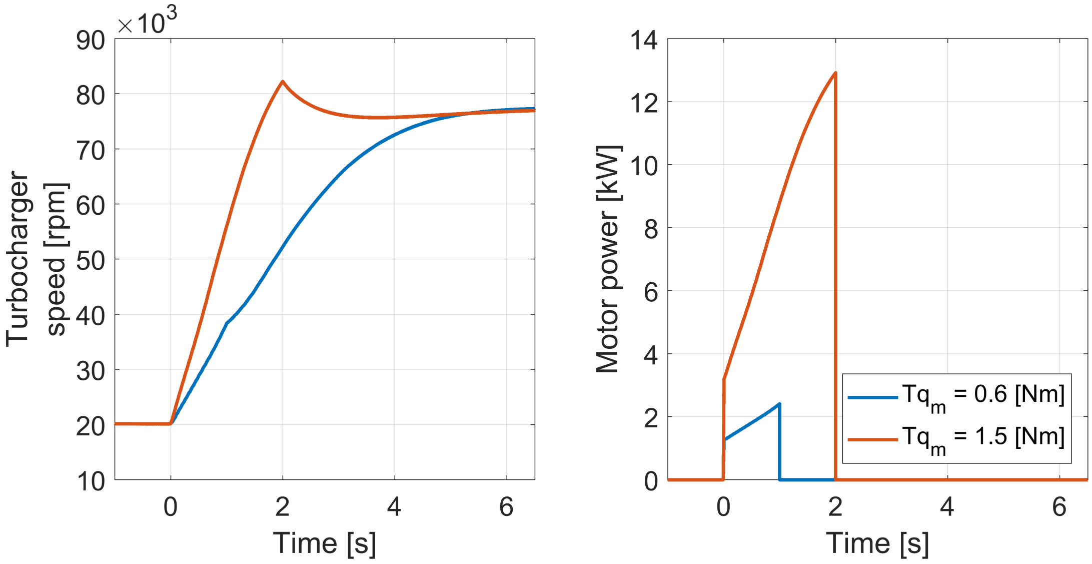

Figure 5.12: Comparison of turbocharger speed and power required for two ideal motors: One producing a torque of $Tq_m = 0.6$ Nm over 1 second and the other a torque of $Tq_m = 1.5$ Nm over 2 seconds

To establish the effects of a delay in the onset of the motor, a delay Δ_d from the start of the transient to the start of the assistance was included in the ideal motor. The time constant τ_{90} was obtained for an ideal motor producing a torque of 0.6 Nm over 1 second with a delay Δ_d ranging from 0 to 3 seconds seen in Figure 5.13. It can be seen that τ_{90} increases for larger delays as one would expect. Additionally, the increasing response times τ_{90} diminish for larger delays. This is a result of less of the assistance given while the fuel limiting effects are present, hence the total response improvements are less significant.

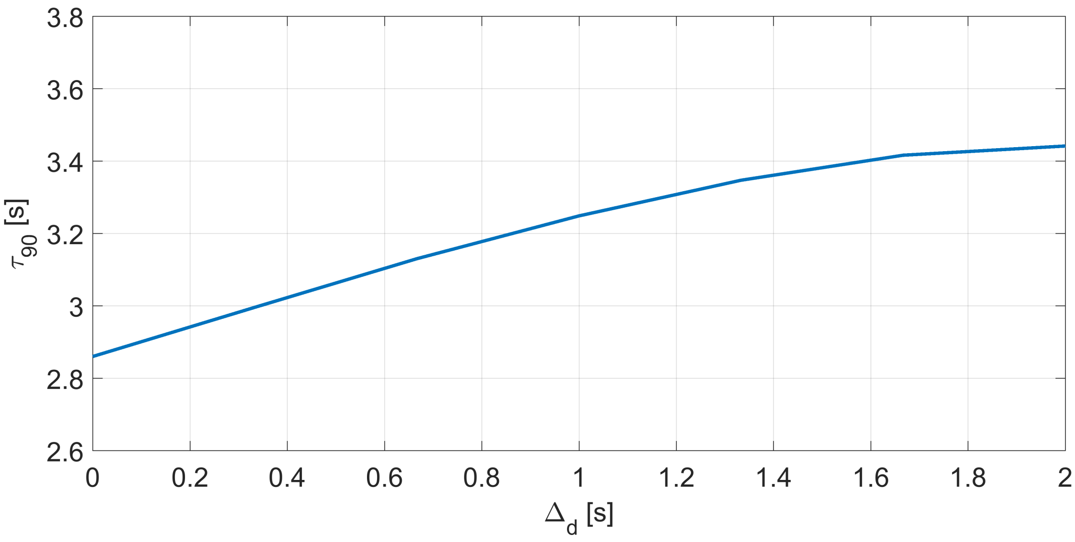

Figure 5.13: Response time τ_{90} with increasing delays from start of transient to start of assistance for an ideal motor producing 0.6 Nm over 1 second

From the parametric study with an ideal motor for the speed increase transient, the following suggestions are given:

- The motor should produce between 0.5 and 1 Nm above the minimum requirements imposed by the inertia of the motor.
- The duration of assistance should be between 1 and 1.5 seconds.
- The two recommendations above require a motor with a maximum power between 3.5 and 8.8 kW.
- The delay from the start of transient to the onset of assistance should be as small as possible.

The effects of torque and duration with an ideal motor on the load increase case can be seen in Figure 5.14. It is seen that less torque over shorter periods is required for significant response improvements than in the speed increase case. In this case a 37-50 % improvement in terms of τ_{rt} is seen with a torque from 0.5-1 Nm over 0.5-1 seconds. Due to the lower turbocharger speeds also significantly less power, from 1.3-3.9 kW, is required. Larger response improvements are seen in this case due to the lower turbocharger speeds throughout the transient. The general trends are the lower the turbocharger speed the more potential an EATC has on improving response. Response improvements for transients starting with larger turbocharger speeds than what has been simulated here will on the other hand see lesser improvements for the same assistance.

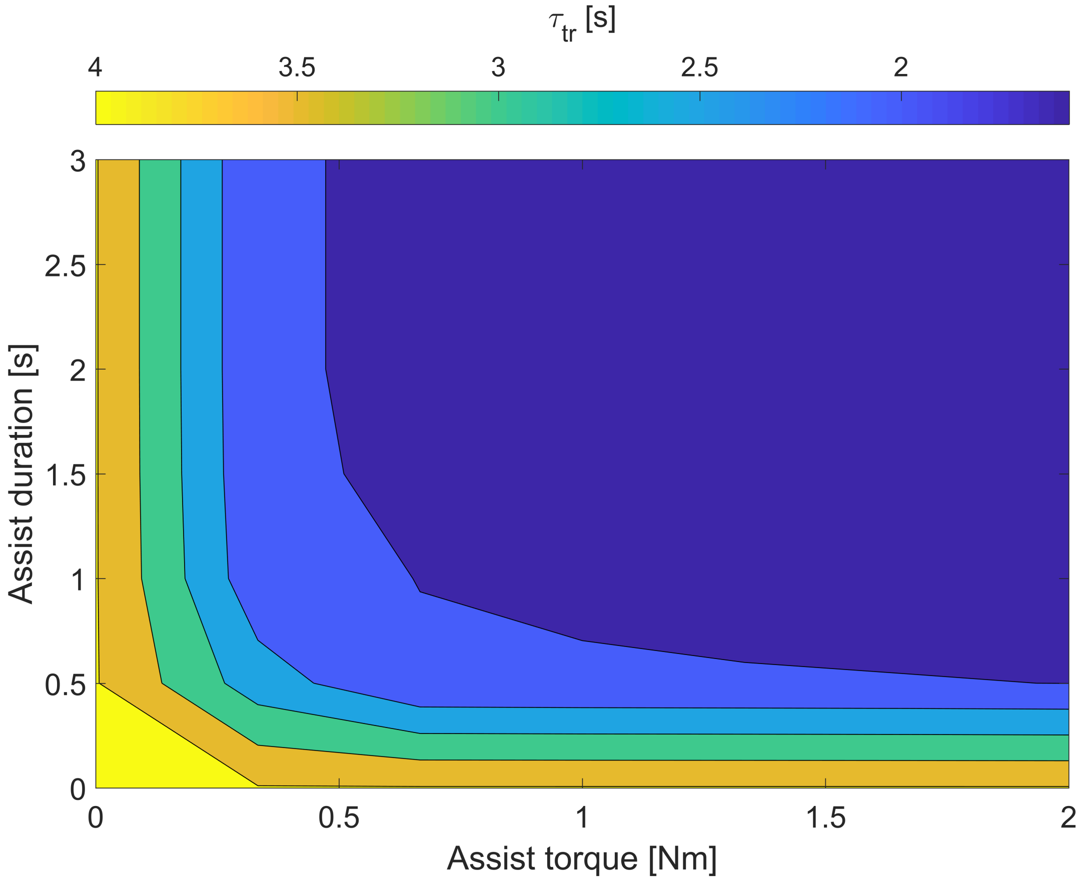

Figure 5.14: Response time τ_{rt} with ideal motor assistance for varying torques and durations

The compressor operating points under ideal motor assistance for 0, 0.5, and 1 Nm of torque over 1 second for the load increase event can be seen in Figure 5.15. The operating points are, as for the speed increase event, well within any boundaries. Hence, a rematch of the compressor is likely not necessary.

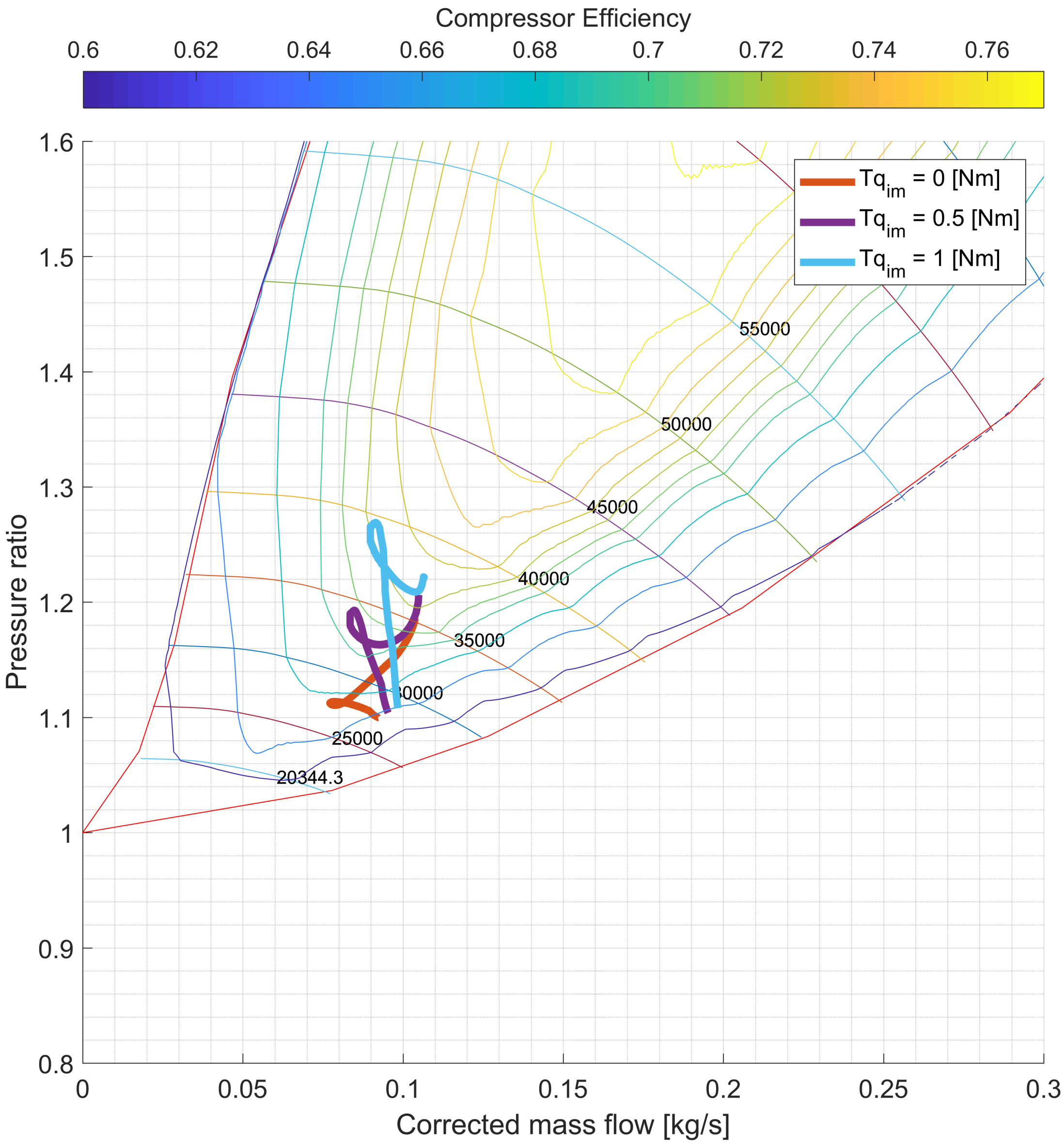

Figure 5.15: Operating points on compressor map plotted for three degrees of ideal motor assistance during a load increase event

5.3 Design Proposal

In an attempt to fulfill the suggestions given by the parametric study for the speed increase transient two assistance motors were proposed. A permanent magnet direct current (PMDC) motor and a series DC motor. Possible motor implementations were also considered.

5.3.1 DC Motors

Due to the difficulty in obtaining specific motor parameters with the suggested performance for the DC machines, these were freely specified. In practice, however, obtaining or constructing motors with the specified parameters may not be possible. High-speed operation with brushed motors are limited by commutation. PMDC and series DC motors require a commutator to periodically reverse the current. A commutator consists of stationary brushes that are in contact with rotating collectors. Commutation limits how fast a PMDC can run due to spark generation at high speeds between the collectors and brushes. Additionally, the time to reverse the current depends on how long a brush is in contact with a collector, while the time a brush is in contact with a given collector reduces with rotational speed.

With the limitations above in mind, a PMDC motor was simulated together with the turbocharger moment of inertia and resistance. It was assumed that the motor had a moment of inertia of J_m = 2 kgcm^2 which is 46 % of the turbochargers moment of inertiaJ_{tc} which might be well conservative. Furthermore, an added resistance connected with additional bearings was assumed to be 20 % of the turbocharger friction defined in Chapter 3.2.3. In the previous section, it was found that the minimum motor torque for a motor with a moment of inertia around 2 kgcm^2 is 0.3 Nm for the first few seconds of the transient. Together with the recommended torque from the parametric analysis a total torque of 1 Nm could be suggested for the given motor inertia. The recommended duration of the assistance was in the range of 1 to 1.5 seconds which for the given transient would end at a turbocharger speed of around 50 000 to 70 000 rpm. The torque-speed curve for a PMDC motor with parameters as specified in Table 5.2 can be seen in Figure 5.16 together with the recommended range. It can be noted that the recommended performance is only provided up to 20 000 rpm. Hence similar response improvements as for the ideal motor is not expected. The response of speed and torque development is also shown while the motor is given its maximum voltage U_{max} = 42 V.

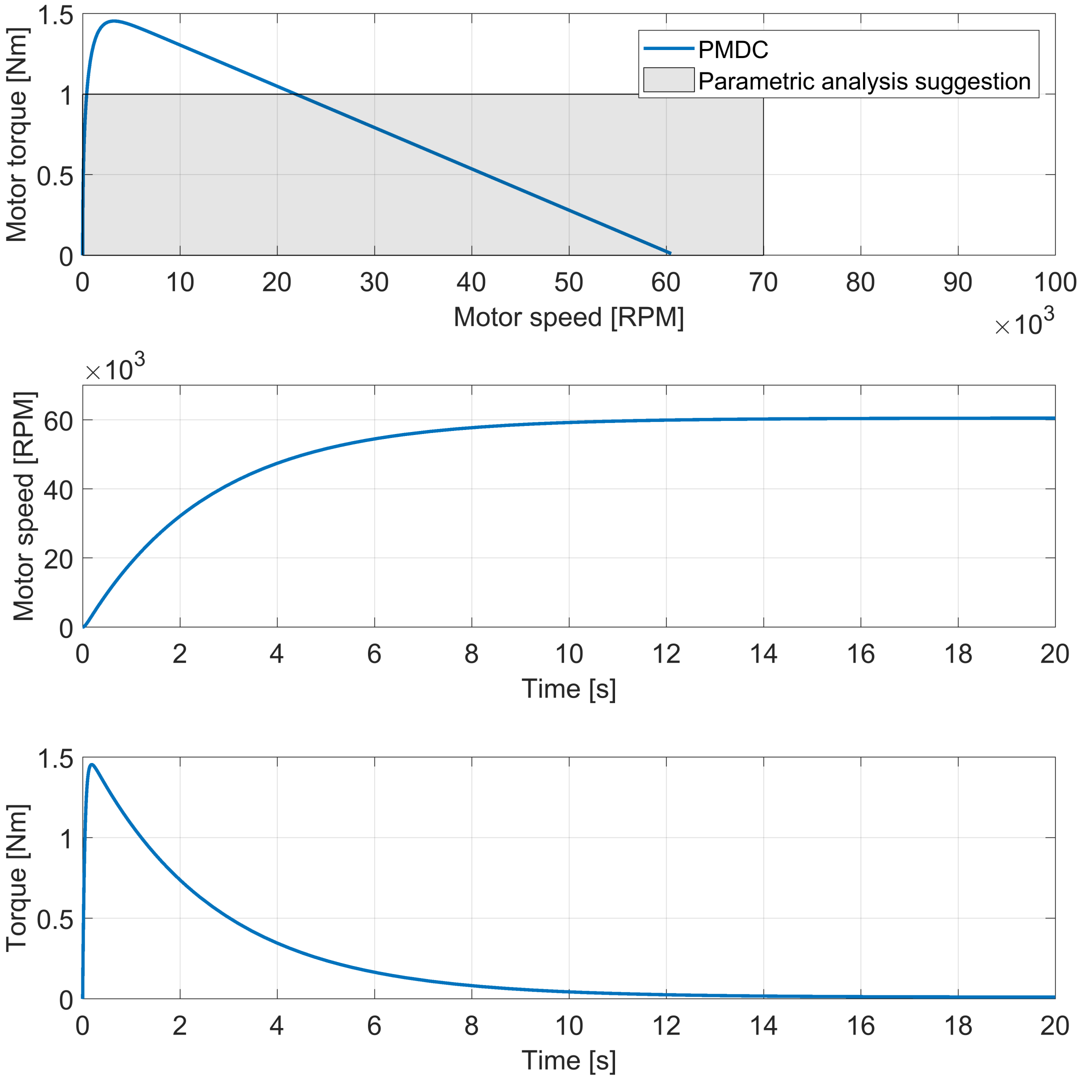

Figure 5.16: Torque speed curve of a PMDC motor, with suggested torque speed area and motor speed and torque development against time

The series DC motor was also simulated under the same conditions as the PMDC motor with the parameters specified in Table 5.2. In the parameter table, it can be noted that the series DC motor has the same values for inductance and resistance as the PMDC motor even though it is for both the armature and field, which might be unrealistic. The back EMF of the series DC motor is proportional to both the armature current and rotational speed consequently limiting the maximum speed. To overcome this a gear with a ratio of 1 to 20 was used. The torque speed plot against the suggested torque speed area together with the response of the torque and speed development for a voltage supply of 42 V can be seen in Figure 5.17. As a result of the gear, the torque produced on the motor side of the gearing peaks at around 90 Nm.

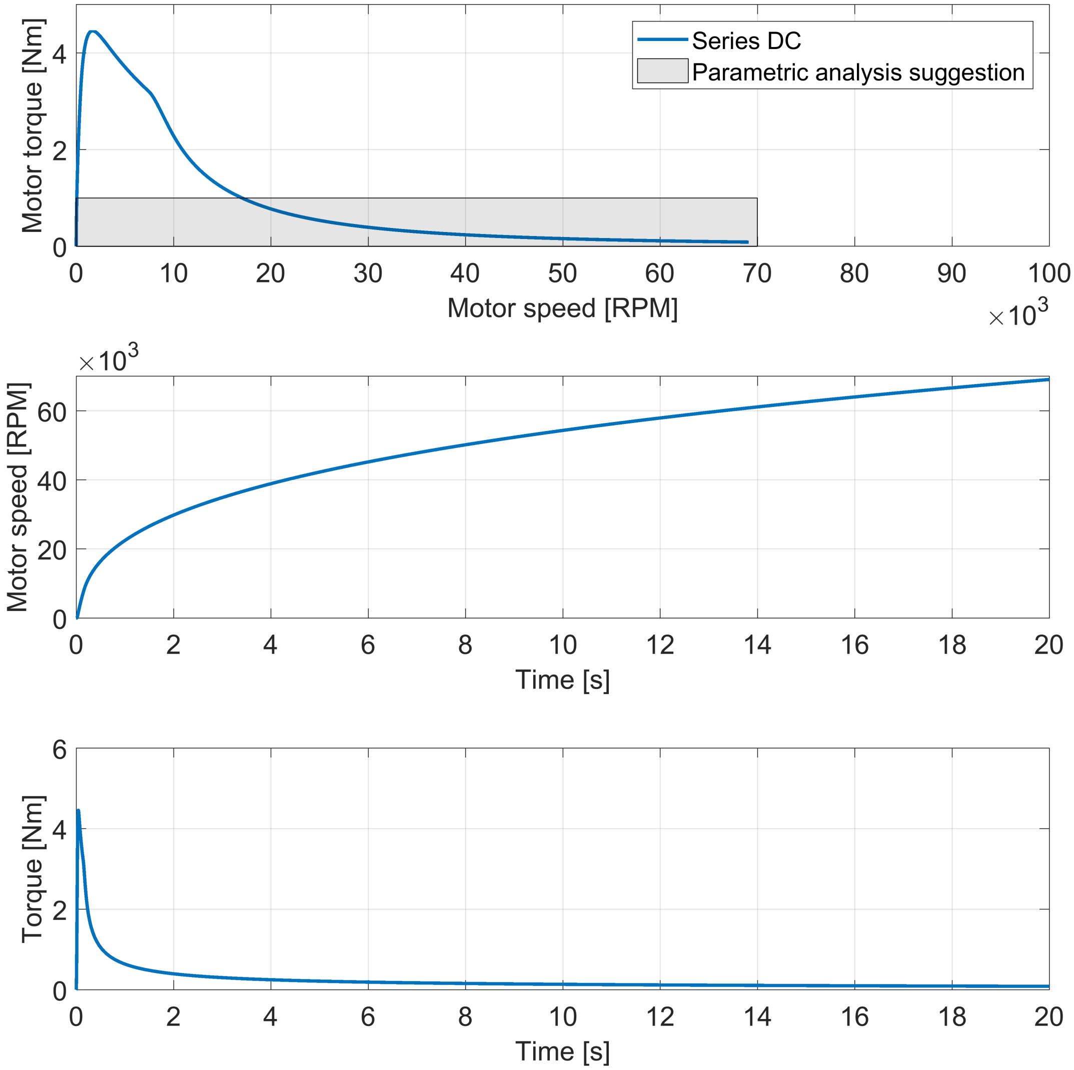

Figure 5.17: Torque speed curve of a series DC motor, with suggested torque speed area and motor speed and torque development against time

Comparing the results from the standstill acceleration simulations of the two DC motors, it can be seen that the larger start torque produced by series motor results in a faster initial acceleration. However, a more realistic test for the EATC application is the acceleration from a low turbocharger speed in the range of 20 000 to 50 000 rpm. Both motors were simulated for the more realistic case by first accelerating up to a speed of 30 000 rpm and then apply maximum voltage. A comparison of the simulations can be seen in Figure 5.18 where speed, torque, and power are shown for the case outlined above. In this case, the PMDC shows better performance, producing more torque and consequently accelerating faster from 30 000 rpm.

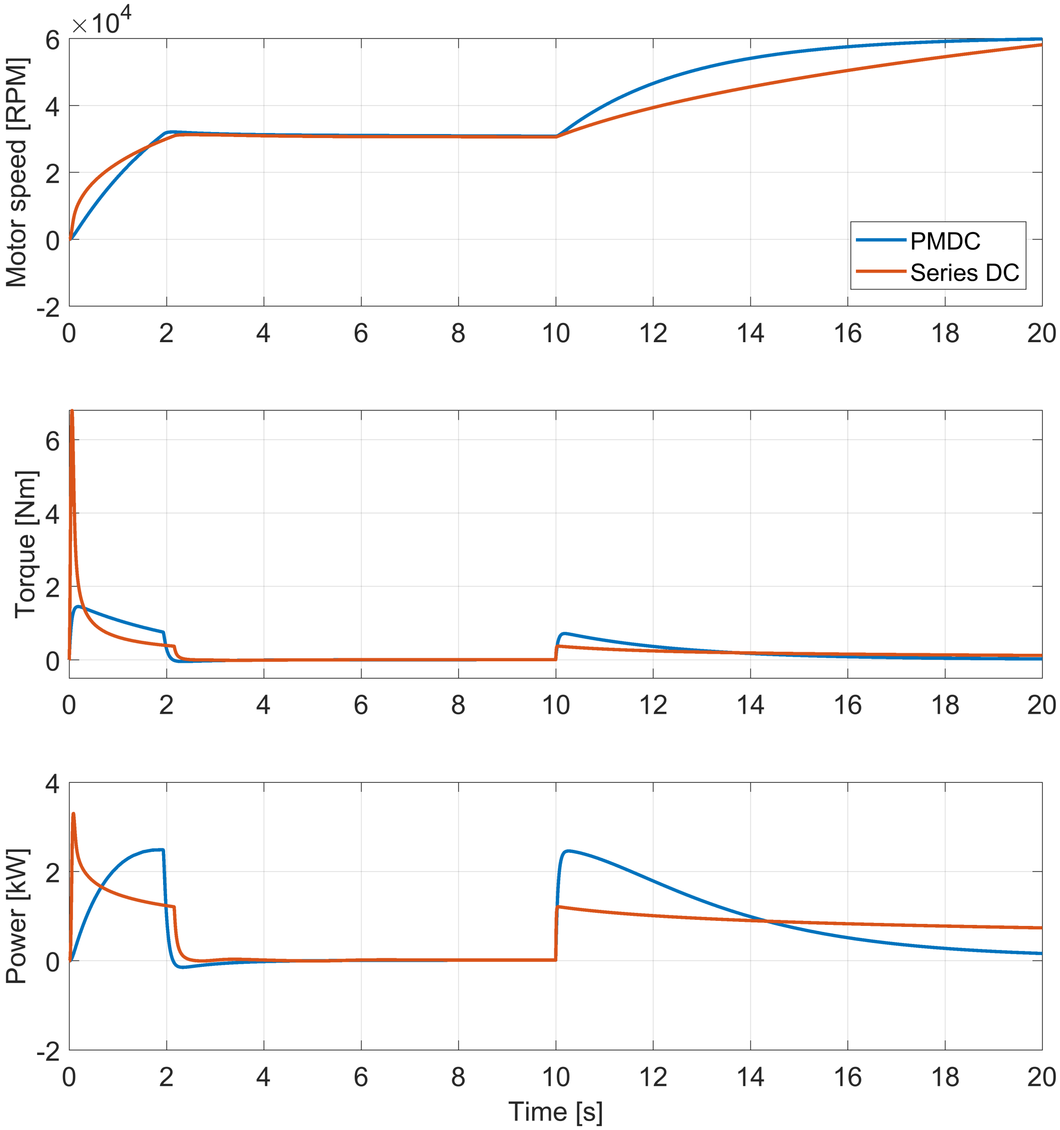

Figure 5.18: PMDC and series DC motor acceleration from standstill to 30 000 rpm, and from 30 000 rpm to maximum speed

With the motor parameters given in Table 5.2 the PMDC is the better choice for an EATC application. Additionally the large torque produced by the series DC motor would require a rigid construction to keep it in place, as well as gears adding to the mechanical complexity and total inertia. Hence, the PMDC was selected over the series DC for the purpose of assisting the turbocharger.

PMDC		**Series DC**	
Parameter	Value	Parameter	Value
l_a	0.008 [H]	$L_a + L_f$	0.008 [H]
r_a	0.18 [Ω]	$r_a + r_f$	0.18 [Ω]
k_t	0.00658 [Nm/A]	K	0.00658[Nm/A^2]
J_m	0.0002 [kgm^2]	J_m	0.0002 [kgm^2]
J_{tc}	0.000434 [kgm^2]	J_{tc}	0.000434 [kgm^2]
R_{gear}	1:1	R_{gear}	1:20
U_{max}	42 [V]	U_{max}	42 [V]

Table 5.2: Motor parameters for the PMDC motor and the series DC motor

5.3.2 Motor Implementation

Several configurations were considered for the EATC. In Figure 5.19 three different configurations are shown.

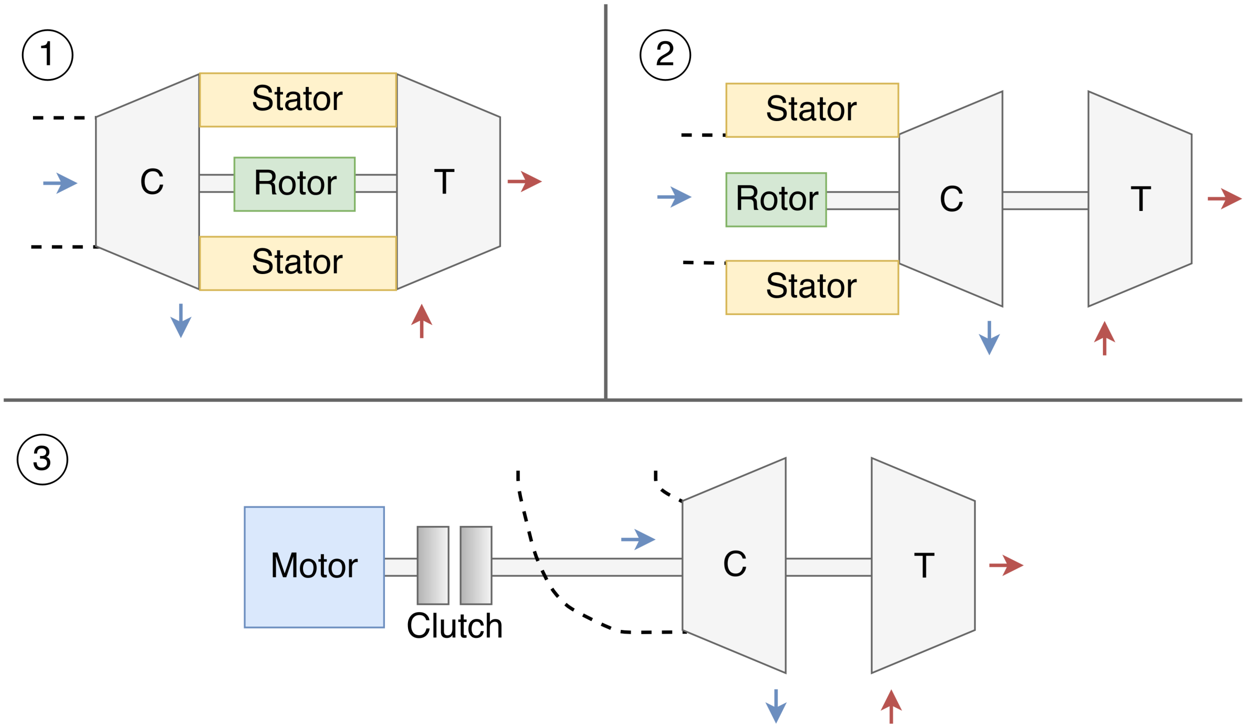

Figure 5.19: Possible configurations of the EATC

Configuration 1 and 2 are advantageous over configuration 3 regarding space requirements and mechanical simplicity. However, configuration 1 and 2 being connected directly to the shaft will have to follow the entire operating range of the turbocharger also when it is not in use. Hence, more stringent requirements are seen in the electromagnetic, thermal, mechanical and power electronic sides of the motor. The increased inertia associated with the rotor will have to follow the turbocharger regardless whether assistance is active or not. Additionally, a mechanism for breaking the armature circuit should be utilized. This ensures that the opposing torque from the back EMF generated current is avoided when assistance is not needed. Configuration 2 will be less affected by heat issues than configuration 1 since it is placed further away from the turbine. However, the air gap between rotor and stator in configuration 2 will be fixed by the dimension of the compressor to not restrict incoming flow, and may not be feasible electromagnetic-wise.

Configuration 3 has the motor placed outside the air intake manifold with a clutch mechanism allowing the motor to be disengaged from the turbocharger shaft. Such a design would require careful balancing of the extended shaft and the clutch mechanism. An analysis of the instabilities and vibrations associated with engaging and disengaging a clutch at high rotational speeds should also be performed. Furthermore, the clutch would add additional inertia to the system. One-half of the clutch would be rotating with the turbocharger even when assistance is not used, however, if half the clutch has less inertia than the motor the total inertia would be lower than a direct connection. Additional resistance will also be introduced from extra bearings to hold the mechanism in place.

The parameters assumed for the different configurations are given in Table 5.3, where J_m, and $J_{cl/2}$ denote motor inertia and half the clutch moment of inertia respectively. With the assumed values the clutch configuration will have a total moment of inertia of 3 kgcm^2 when in use, and 0.5 kgcm^2 when not in use. Whereas configuration 1 and 2 will have a total moment of inertia of 2 kgcm^2 regardless.

Clutch configuration		**Fixed rotor configuration**	
Parameter	Value	Parameter	Value
J_m	2 [kgcm^2]	J_m	2 [kgcm^2]
$J_{cl/2}$	0.5 [kgcm^2]		

Table 5.3: Moments of inertia used for the clutch and fixed rotor configurations

Assistance Logic

Depending on the configurations above, two simple assistance logics were proposed with the purpose of initiating and deactivating the EATC. One system was developed for the fixed rotor configuration and another for the clutch mechanism. From the parametric analysis, it was seen that much of the response improvements were obtained when the turbocharger was assisted while fuel limiting effects were present. This was selected as the control criteria for both assistance logics, i.e assist when fuel limiting effects are present. Using the notation from Chapter 3.2.4 the criteria can be stated as in equation (5.3). Assistance outside of the criteria stated in equation (5.3) will still provide response improvements which the proposed logics does not take advantage of. Hence, further improvements can be made by implementing better control strategies than those suggested here.

$$uGov_{sat} > uGov_{sl} \tag{5.3}$$

For configurations 1 and 2, a pseudo code diagram of the control strategy can be seen in Figure 5.20. For each time step, if the criteria in equation (5.3) holds, the armature circuit is closed, and the motor speed reference is set to its maximum value $\omega_{m,max}$. If the smoke limiter is not active, the circuit is opened, and the controller action is stopped. The process is then repeated for each time step.

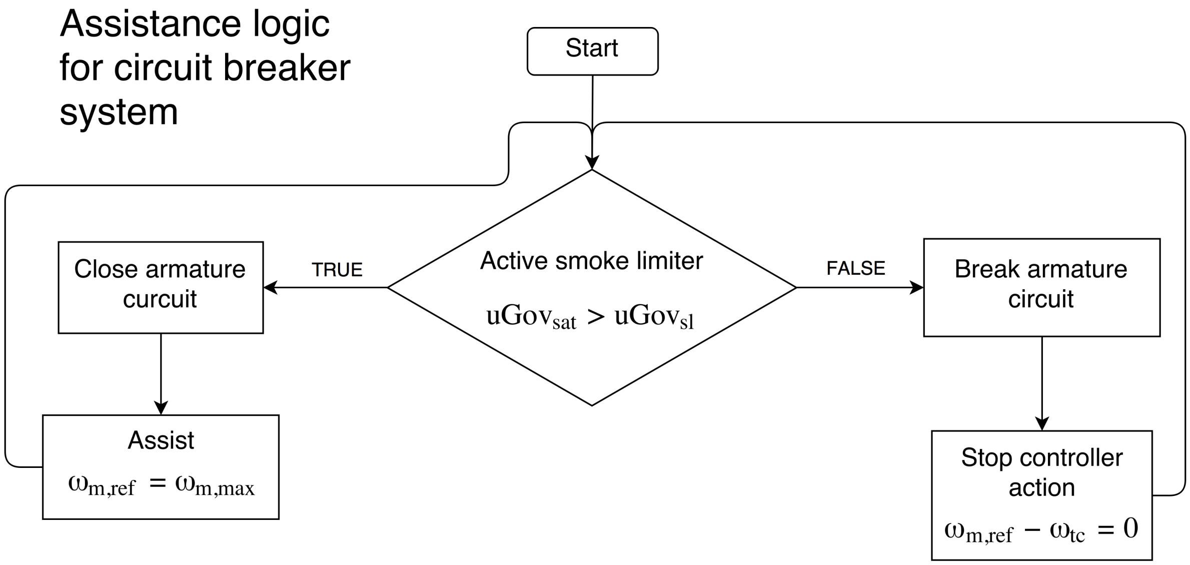
Assistance logic
for circuit breaker
system
Start
Active smoke limiter
$uGov_{sat} > uGov_{sl}$
TRUE
FALSE
Close armature curcuit
Assist
$\omega_{m,ref} = \omega_{m,max}$
Break armature circuit
Stop controller action
$\omega_{m,ref} - \omega_{tc} = 0$

Figure 5.20: Pseudo code diagram for the EATC logic for the fixed rotor configuration

An advantage of the clutch configuration was that fewer requirements were imposed on the motor. For this reason, a threshold turbocharger speed ω_{thr} was included in the logic seen in Figure 5.21. The threshold allows the specification of an upper limit the motor will assist for. It should be noted that if the smoke limiter activates below ω_{thr}, assistance is provided until the smoke limiter deactivates, restricted only by $\omega_{m,max}$. However by specifying $\omega_{m,max}$, and ω_{thr} a motor rated for lower speeds than turbocharger speeds could still be used. In the following simulations the threshold and maximum speed were set to $\omega_{thr} = 60\,000$ rpm and $\omega_{m,max} = 100$

000 rpm.

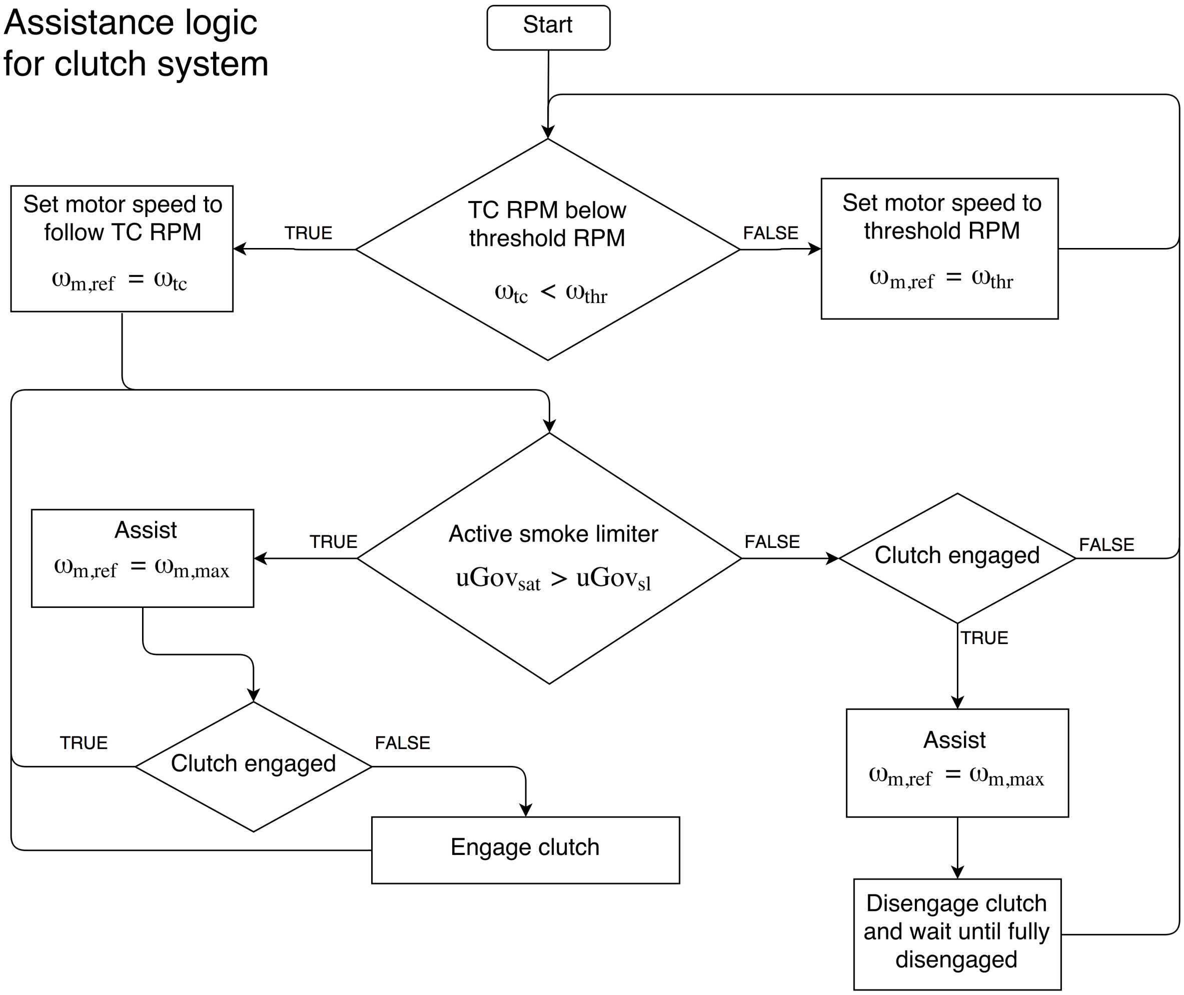
Assistance logic
for clutch system
Start
TC RPM below
threshold RPM
$\omega_{tc} < \omega_{thr}$
TRUE
FALSE
Set motor speed to
follow TC RPM
$\omega_{m,ref} = \omega_{tc}$
Set motor speed to
threshold RPM
$\omega_{m,ref} = \omega_{thr}$
Active smoke limiter
$uGov_{sat} > uGov_{sl}$
TRUE
FALSE
Assist
$\omega_{m,ref} = \omega_{m,max}$
Clutch engaged
FALSE
TRUE
TRUE
Clutch engaged
FALSE
Engage clutch
Assist
$\omega_{m,ref} = \omega_{m,max}$
Disengage clutch
and wait until fully
disengaged

Figure 5.21: Pseudo code diagram for the EATC logic for the clutch configuration

If the turbocharger speed is larger than ω_{thr} the motor will match the threshold speed and be ready should the speed drop below again. Otherwise, the motor follows the speed of the turbocharger and assists if the smoke limiter is active. Both clutch engagement and disengagement follow a predefined profile over 0.2 seconds. When disengaging the clutch the motor keeps assisting until the clutch is fully disengaged. Defining the clutch engagement start time as t_0 and disengagement start time as t_d the clutch engagement profile can be seen in Figure 5.22.

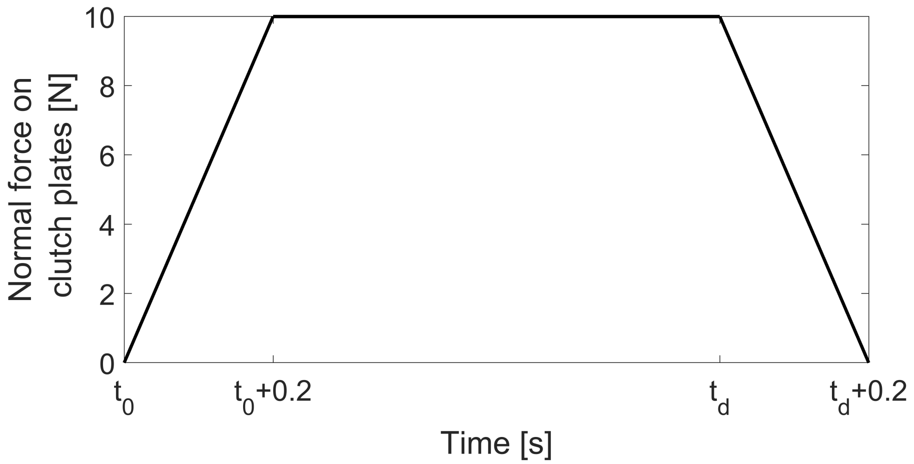

Figure 5.22: Predefined clutch engagement profile

Comparison of the suggested designs

With the assumed values for the PMDC motor and the moments of inertia for the configurations, the systems were simulated for the transient speed increase event from 900 to 1400 rpm with an initial load of 70 % to a final load of 80 % of maximum load. A comparison of how the configurations compare is seen in Figure 5.23. The additional inertia associated with the clutch worsens the response despite having a slightly longer assistance period due to the clutch disengagement compared to the fixed rotor configuration. A comparison of response times τ_{90} for the systems and the conventional turbocharger are given in Table 5.4.

Configuration	$\boldsymbol{\tau_{90}}$	**Improvement**
Rotor fixed to shaft	3.13 [s]	14 %
Clutch system	3.24 [s]	11 %
No assistance	3.64 [s]	

Table 5.4: Response times for the proposed configurations for a 900-1400 rpm, 70-80 % load, speed increase transient

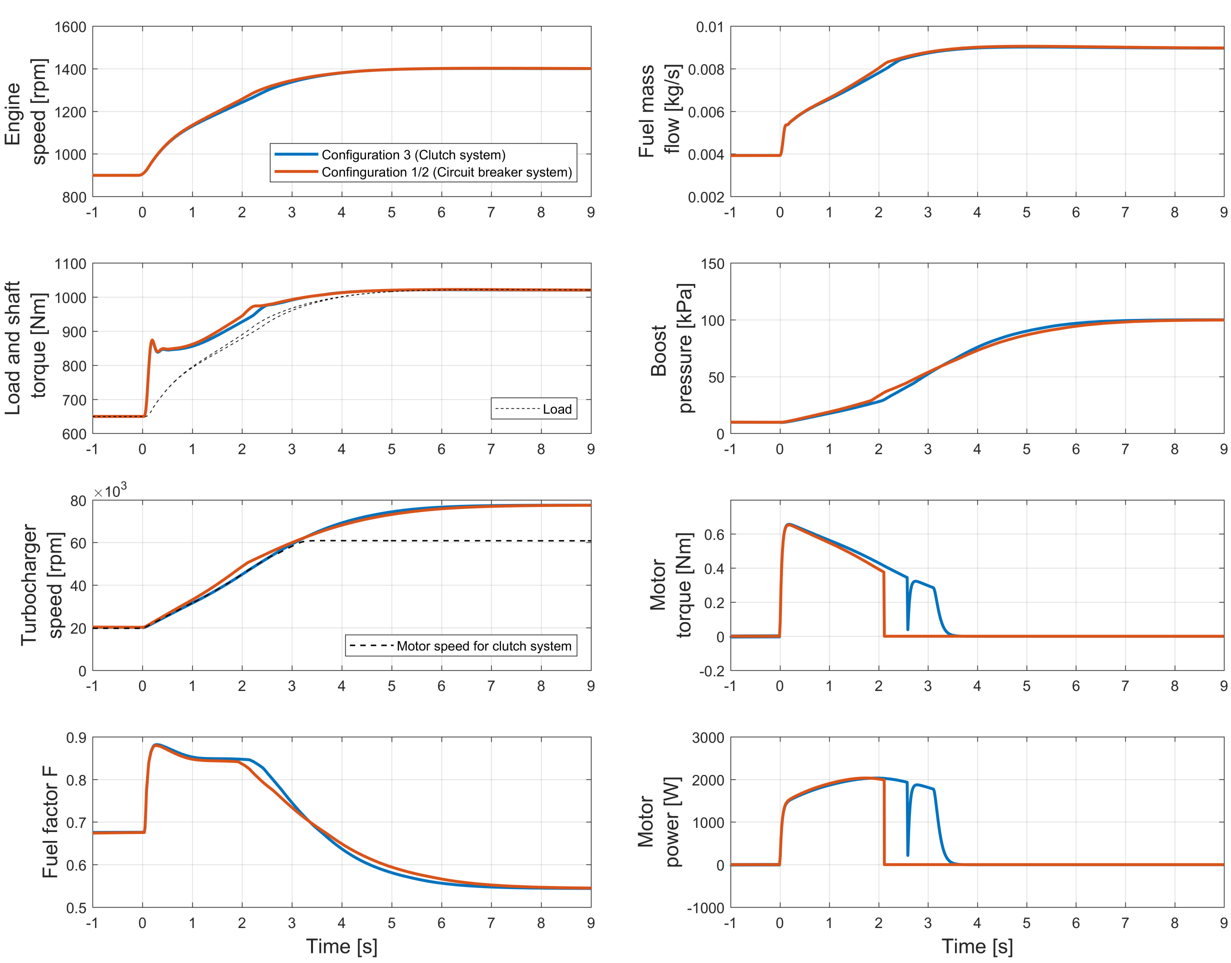

Figure 5.23: Engine speed, torque, turbocharger speed, fuel factor F, mass flow of fuel, boost pressure, motor torque, and motor power for the proposed configurations

Only marginal improvements in response are seen from the lighter clutch system when no assistance is needed. A comparison of the configurations for a speed increase from 1300 to 1600 rpm when no fuel limiting occurs can be seen in Figure 5.24 with response times τ_{90} given in the Table 5.3.2. Based on these findings the fixed rotor configuration is suggested, providing a 14 % response improvement for with the assumed values.

Configuration	τ_{90}
Rotor fixed to shaft	0.93 [s]
Clutch system	0.90 [s]

Table 5.5: Response times for configuration 1 or 2 and configuration 3 for a 1300 - 1600 rpm speed increase transient without assistance

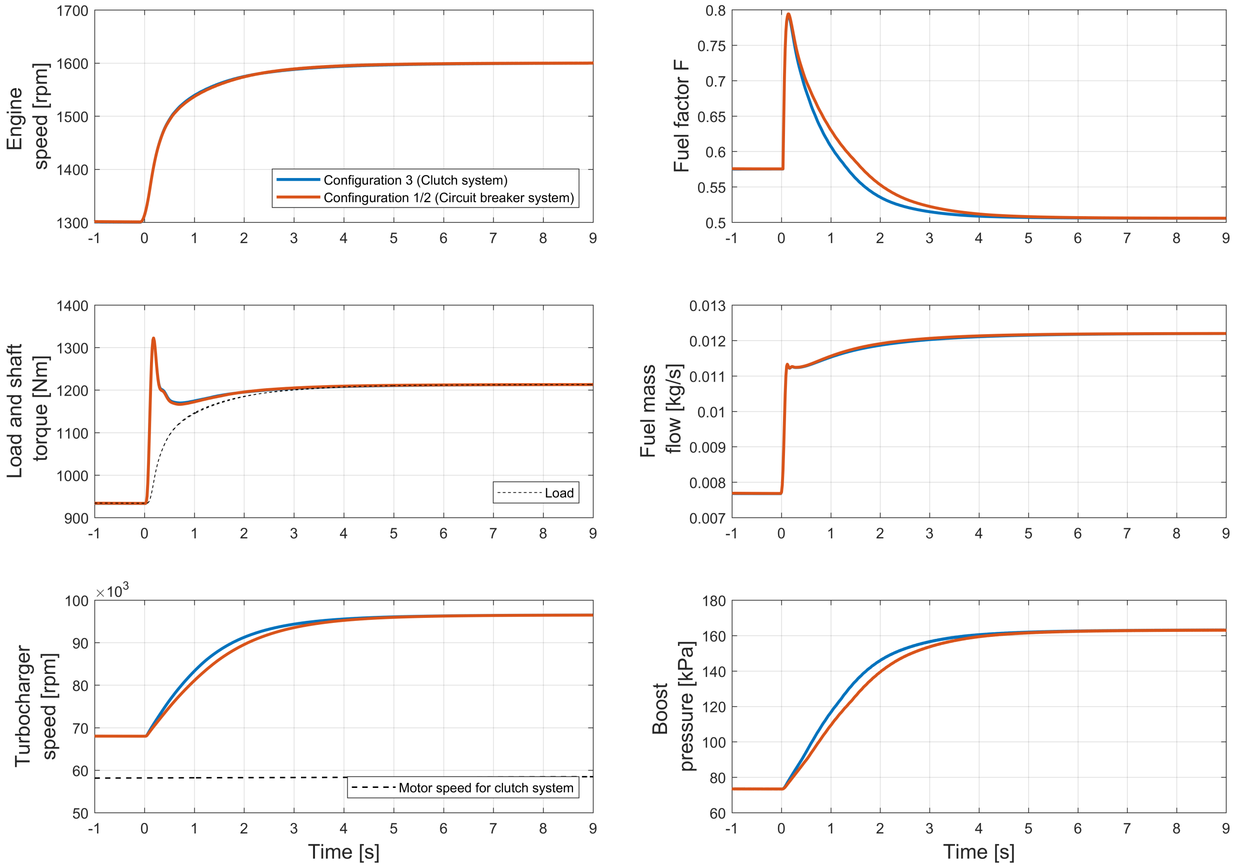

Figure 5.24: Engine speed, torque, turbocharger speed, fuel factor F, mass flow of fuel, an boost pressure for the proposed configurations when assistance is not active.

Based on the findings above a fixed rotor configuration is recommended for any implementation of an EATC in the lab given that the motor can handle the large temperatures and high speeds. Since PMSM and IM machines have proven to be capable of producing the required torque speed curve outlined in the parametric study while handling turbocharger speeds, Noguchi et al. [19], Noguchi et al. [20], Bumby et al. [18], these motor types could be candidates for any future implementation in the lab.

Chapter 6

Summary and Recommendations for Further Work

This chapter completes this thesis with a summary and discussion of the main results, ending with recommendations for further work.

6.1 Summary and Conclusions

Using a dynamic process engine model, potential response improvements by use of an electrically assisted turbocharger were presented. In Chapter 3 the engine model used to evaluate the EATC concept was presented with an explanation of most of the sub-models together with the calculations performed. Two DC motor models were also presented as well as the engine control system.

The model was validated against experimental data from a laboratory engine in Chapter 4. For speed increase transients with medium and high initial engine speeds the model was around 50 % faster than the actual engine. For speed increase transients starting at low engine speeds, the time constants of the model and actual engine were similar. The model also showed larger values than the experimental data in steady-state for turbocharger speeds and intake manifold pressures. A stricter smoke limiter was imposed and a slight improvement in response times between the experimental data and simulations was seen. Based on the scope of the model, two transients characterized by fuel limiting and turbo-lag was selected to be used in the parametric analysis.

A parametric study of response improvements was performed in Chapter 5, achieving the objective of showing improved response improvements with an EATC, and how the individual parameters affected the response. A performance metric τ_{90} was defined as the time from the start of the transient to 90 % of the step in engine speed was reached, and used to evaluate response improvements. Another performance metric τ_{tr} was used to evaluate improvements in a load increase case.

For the speed increase case, the minimum torque required by an assistance motor was identified for various motor inertias. For a given motor mass moment of inertia, the early phase of the transient required less torque from an EATC to accelerate faster than a conventional turbocharger. With a motor inertia of 2 kgcm^2, around 0.3 Nm of torque would be required for the start of transient whereas 0.45 Nm would be required as the exhaust gas energy peaks during the transient. It was also seen that increased mass moments of inertia on the turbocharger shaft linearly worsened response in terms of the defined performance metric τ_{90}.

An ideal motor producing a fixed torque regardless of engine speed was used to simulate the effects magnitude, duration, and delay of assistance had on response times. For the speed increase transient, response improvements in the range 20-30 % were seen with an additional torque on the shaft from 0.5-1 Nm over a 1-1.5 second duration corresponding to a maximum motor power from 3.5-8.8 kW. Further degrees of assistance quickly saw much larger power requirements from the motor, while response improvements diminished. Any delay in the onset of the assistance worsened response times. Furthermore, it was seen that much of the response improvements were made when the engine was assisted while fuel limiting occurs.

For the load increase case, larger response improvements were seen with less assistance. Specifically, the time constant τ_{tr} was reduced by 37-50 % with an ideal motor with a torque from 0.5-1 Nm over a duration from 0.5-1 seconds, requiring a maximum motor power from 1.3-3.9 kW.

A design proposal for the electric motor and implementation of the system was also presented for the speed increase event. A PMDC motor proved to be a better alternative than a series

DC motor for the application with the assumed motor parameters. The PMDC produced more torque at higher speeds, additionally it not need the extra complexity and inertia associated with gears. The PMDC motor was then simulated together with the engine model for two main types of configurations a fixed rotor configuration, and a clutch configuration. A simple logic to determine when the motor should assist was developed for both configurations. The rotor fixed configuration proved better than the clutch configuration due to lower moment of inertia and less mechanical complexity. The clutch system having less moment of inertia when assistance was not required, showed only marginal response improvements over the fixed rotor. The fixed rotor PMDC motor with the developed assistance logic showed a response improvement of 14 % with respect to the time constant τ_{90}.

6.2 Discussion

For initial evaluations of response improvements a zero-dimensional filling and emptying single zone engine model was assumed to provide required complexity to capture the general trends of the dynamics related to turbocharger lag. The zero-dimensional filling and emptying assumption, neglecting exhaust gas momentum, is possibly the most crude assumption for this purpose. The Scania engine in the lab is semi-pulse charged. This means that some effort has been put into designing an exhaust manifold geometry such that part of the momentum in the exhaust gas pulses are utilized and transferred into rotational power by the turbine, an effect not captured by the model.

The faster response of the model seen in the transient validation for the larger engine speeds could in part be attributed to the model lacking a form of boost control. In the real engine, boost control is likely achieved by regulating the amount of fueling at high turbocharger rotational speeds to keep the system within its limitations. This is possibly also a contributing factor, together with the differences in engine parameters, for the larger steady-state values seen for the model.

Ideally, the model should have been validated and tuned for steady-state conditions before comparing transient responses. Despite the difficulties with transient validation, a steady-state validation to start with would at least guarantee that the model behaved like the real engine in steady-state conditions. This could, in turn, provide a more accurate transient behavior. Nevertheless, similar time constants were seen for the model and engine at low engine speeds.

The transients for evaluating response improvements was selected to produce fuel limiting effects while still being within the scope of the model. Moreover, they were in the low engine speed range where the model and experimental responses were comparable. Hence, the general trends shown in the parametric study should be fairly similar to what could be expected on the real engine.

Even harder cases of turbo-lag than those simulated could occur on the real engine. By comparing the parametric study of assisted torque and duration for the load and speed increase events, it was seen that more improvements were gained from the assistance of transients with lower turbocharger speeds. Consequently, transients starting at even lower loads than what could be simulated here could see even larger response improvements from the suggested parameters. Also, transients in the higher load and speed ranges would see less improvements or require a more powerful motor.

The DC motor models used in the design proposal were modeled with assumed motor parameters which are likely unrealistic. Also, possible thermal effects associated with high speeds and the engine environment were not considered. Furthermore, the suggested logics based on assisting only when fuel limiting occurs has room for improvements. Ideally, the logic should predict the duration of the whole transient based on the engine parameters and assist accordingly if possible.

6.3 Recommendations for Further Work

With an ultimate goal of implementing an EATC in the lab a recommendation of further work follows:

- Adapt the model to the Scania engine in the lab by removing a cylinder and perform steady-state validation and tuning

- Implement a boost control resembling that of the engine in the model
- Study which motor types are most suited for the application, and develop detailed models of them including the thermal, mechanical and electromagnetic dynamics
- Analyze how the turbocharger shaft can be balanced after the rotor is attached
- Develop a better logic to determine the onset of assistance
- Explore the regenerative potential of using the motor as a generator together with an energy storage system
- Determine specific motor parameters by simulating the detailed motor models together with the steady-state validated engine model
- Build the EATC and implement it in the lab

Bibliography

[1] Tatsuo Takaishi, Akira Numata, Ryouji Nakano, and Katsuhiko Sakaguchi. Approach to high efficiency diesel and gas engines. *Mitsubishi Heavy Industries Review*, 45(1):21–24, 2008.

[2] S. M. Shahed and Karl-Heinz Bauer. Parametric studies of the impact of turbocharging on gasoline engine downsizing. *SAE International Journal of Engines*, 2(2009-01-1472):1347–1358, 2009.

[3] Federico Millo, Fabio Mallamo, E. Pautasso, and G. Ganio Mego. The potential of electric exhaust gas turbocharging for HD diesel engines. Technical report, SAE Technical Paper, 2006.

[4] Tomai Katrašnik, Samuel Rodman, Ferdinand Trenc, Aleš Hribernik, and Vladimir Medica. Improvement of the dynamic characteristic of an automotive engine by a turbocharger assisted by an electric motor. *Journal of engineering for gas turbines and power*, 125(2):590–595, 2003.

[5] Maria Thirouard, Sylvain Mendez, Pierre Pacaud, Vincent Chmielarczyk, Didier Ambrazas, Chrsitophe Garsi, Frédéric Lavoisier, and Bertrand Barbeau. Potential to improve specific power using very high injection pressure in HSDI diesel engines. Technical report, SAE Technical Paper, 2009.

[6] Constantine D. Rakopoulos and Evangelos G. Giakoumis. *Diesel engine transient operation: principles of operation and simulation analysis.* Springer Science & Business Media, 2009.

[7] Martinez-Botas Ricardo, Pesiridis Apostolos, and MingYang Yang. Overview of boosting options for future downsized engines. *Science China Technological Sciences*, 54(2):318–331, 2011.

[8] N. Watson and M. S. Janota. *Turbocharging the Internal Combustion Engine*. Wiley, 1982. ISBN 978-0-471-87072-2.

[9] John Heywood. *Internal Combustion Engine Fundamentals*. McGraw-Hill Education, April 1988. ISBN 978-0-07-028637-5.

[10] Hung Nguyen-Schäfer. *Rotordynamics of automotive turbochargers*. Springer, 2015.

[11] M. Tancrez, J. Galindo, C. Guardiola, P. Fajardo, and O. Varnier. Turbine adapted maps for turbocharger engine matching. *Experimental Thermal and Fluid Science*, 35(1):146–153, January 2011. ISSN 0894-1777. doi: 10.1016/j.expthermflusci.2010.07.018.

[12] Lino Guzzella and Christopher Onder. *Introduction to modeling and control of internal combustion engine systems*. Springer Science & Business Media, 2009.

[13] Garrett. *Product Catalog vol.6*, 2017. `https://www.turbobygarrett.com/turbobygarrett/sites/default/files/catalog/TBG-Catalog-Vol-6.pdf` [Accessed: 2017-31-05].

[14] Zoran Filipi, Yongsheng Wang, and Dennis N. Assanis. Effect of variable geometry turbine (VGT) on diesel engine and vehicle system transient response. Technical report, SAE Technical Paper, 2001.

[15] J. D. Ledger, Rowland S. Benson, and H. Furukawa. Improvement in transient performance of a turbocharged diesel engine by air injection into the compressor. Technical report, SAE Technical Paper, 1973.

[16] Thomas N. Schmitz, Klaus-D. Holloh, Rolf Juergens, and Guenter Fleckenstein. Potential of additional mechanical supercharging for commercial vehicle engines. Technical report, SAE Technical Paper, 1994.

[17] J. Galindo, J. M. Luján, H. Climent, and C. Guardiola. Turbocharging system design of a sequentially turbocharged diesel engine by means of a wave action model. Technical report, SAE Technical Paper, 2007.

[18] J. R. Bumby, E. S. Spooner, J. Carter, H. Tennant, G. Ganio Mego, G. Dellora, W. Gstrein, H. Sutter, and J. Wagner. Electrical machines for use in electrically assisted turbochargers. In *Power Electronics, Machines and Drives, 2004.(PEMD 2004). Second International Conference on (Conf. Publ. No. 498)*, volume 1, pages 344–349. IET, 2004.

[19] Toshihiko Noguchi, Yosuke Takata, Yukio Yamashita, and Seiichi Ibaraki. 160,000-r/min, 2.7-kW Electric Drive of Supercharger for Automobiles. In *Power Electronics and Drives Systems, 2005. PEDS 2005. International Conference on*, volume 2, pages 1380–1385. IEEE, 2005.

[20] Toshihiko Noguchi, Yosuke Takata, Yukio Yamashita, Yoshimi Komatsu, and Seiichi Ibaraki. 220,000-r/min, 2-kW permanent Magnet Motor Drive for Turbocharger. In *International Power Electronics Conference (IPEC-Niigata 2005)*, 2005.

[21] David Gerada, Abdeslam Mebarki, Neil L. Brown, Chris Gerada, Andrea Cavagnino, and Aldo Boglietti. High-speed electrical machines: Technologies, trends, and developments. *IEEE Transactions on Industrial Electronics*, 61(6):2946–2959, 2014.

[22] S. Münz, M. Schier, H. P. Schmalzl, and T. Bertolini. *eBooster design and performance of a innovative electrically driven charging system.* 2008.

[23] E. Pedersen and H. Engja. Mathematical modeling and simulation of physical systems. *Department of Marine Technology, Norwegian University of Science and Technology*, 2008.

[24] Dean C. Karnopp. State variables and pseudo bond graphs for compressible thermofluid systems. *Journal of Dynamic Systems, Measurement, and Control*, 101(3):201–204, 1979.

[25] Eilif Pedersen and Hallvard Engja. A bond graph model library for modelling diesel engine transient performance. *ISME Tokyo*, 2:447–455, 2000.

[26] Franziska Zacharias. Analytical representation of the thermodynamic properties of combustion gases. Technical report, SAE Technical Paper, 1967.

[27] Kevin Koosup Yum. Modeling and Simulation of Transient Performance and Emission of Diesel Engine: Pseudo Bond Graph Approach to Modelling the Thermodynamic Process. *107*, 2012.

[28] C. A. Finol and K. Robinson. Thermal modelling of modern engines: a review of empirical correlations to estimate the in-cylinder heat transfer coefficient. *Proceedings of the institution of mechanical engineers, part D: journal of automobile engineering*, 220(12):1765–1781, 2006.

[29] Kevin Koosup Yum, Bhushan Taskar, Eilif Pedersen, and Sverre Steen. Simulation of a two-stroke diesel engine for propulsion in waves. *International Journal of Naval Architecture and Ocean Engineering*, 2016.

[30] Robin Vanhaelst, Alaa Kheir, and Jakub Czajka. A systematic analysis of the friction losses on bearings of modern turbocharger. *Combustion Engines*, 55, 2016.

[31] Sergio Junco and Alejandro Donaire. Bond graph modeling and simulation of electrical machines. In *Bond Graph Modelling of Engineering Systems*, pages 269–321. Springer, 2011.

Appendix A

A.1 PID Control

The basic idea of a proportional, integral, derivative (PID) controller is to compute the control signal based on a linear combination of the error, the derivative of the error and the integral of the error. The error $e(t)$ is defined as the difference between the actual and desired value. The continuous-time controller output can be expressed as

$$u(t) = K_p e(t) + K_i \int_0^t e(\tau) d\tau + K_d \dot{e}(t) \tag{A.1}$$

where K_p, K_i, and K_d are constant scalar quantities that are tuned to achieve the desired performance. Figure A.1 shows a block diagram of a PID controller in a control loop, with the different terms computed in parallel. A PI controller is simply a PID without the derivative term.

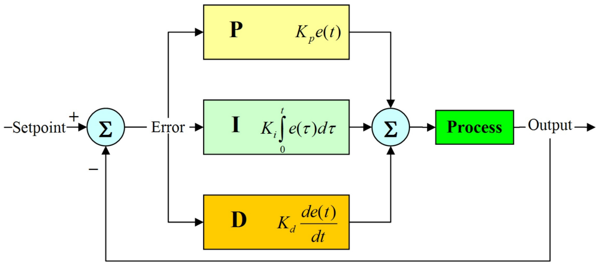

Figure A.1: Block diagram of a PID controller in the loop.

A.2 Load acceptance test

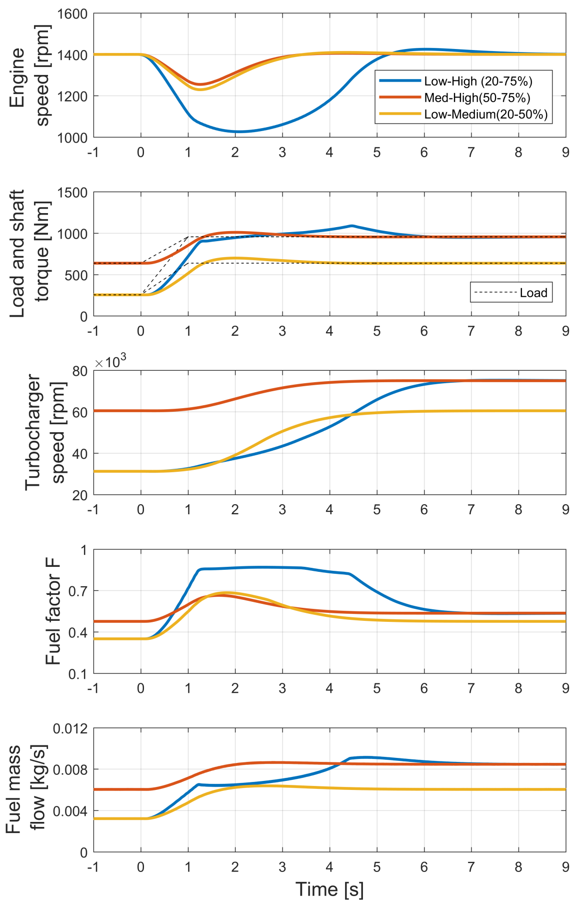

Figure A.2: Engine speed, torque, turbocharger speed, fuel factor F and mass flow of fuel responses for the 1400 rpm load acceptance test. Specific initial and final conditions are given in table 5.1